ELECTROMAGNETIC PULSE ENVIRONMENT STUDIES

Volume II

Late-Time, High-Altitude Electromagnetic Pulse Code Development

Science Applications, Inc.
Albuquerque, NM 87108
James A. Marks

Dikewood Corporation
Albuquerque, NM 87106
Vernon W. Pine

Final Report for Period 5 May 1972 through 31 December 1973

June 1974

This project has been partially supported by the Defense Nuclear Agency under DNA Subtask R99QAXEA094, Low Altitude EMP Phenomenology, DNA Work Unit 41, Low Altitude Predictions.

Prepared for
Defense Nuclear Agency
Washington, DC 20305

AIR FORCE WEAPONS LABORATORY
Air Force Systems Command
Kirtland Air Force Base, NM 87117

Table of Contents

List of Illustrations

Illustrations (Cont'd.)

SECTION I
INTRODUCTION

Two basic approaches are being pursued at the Air Force Weapons Laboratory to define late-time (after the initial peak) electromagnetic pulse (EMP) signals from a high-altitude nuclear detonation. The first, and more nearly complete approach is to model as completely as possible, all geometric variables (i.e., curved earth surface, atmospheric density, geomagnetic field, etc.). A compromise had to be made to perform such a calculation on existing computers. That is, instead of a complete three-dimensional calculation, a vertical geomagnetic field was imposed giving azimuthal symmetry and reducing the problem to two spatial dimensions. The result was the code HAPS (Ref. 1), High Altitude Prolate Spheroidal code. Results and comparisons of HAPS are described in Section II.

The other approach is one where considerable geometric assumptions are made to reduce the problem to a one-dimensional calculation as outlined by C. L. Longmire (Ref. 2). This method can give insight into two-dimensional effects in relatively short computer runs. The utility of it would be between the regions where one-dimensional line-of-sight methods are no longer valid to a point in time where geometrical considerations are important. Section III describes the development of a code, P, using this method and shows some preliminary comparisons to other results.

SECTION II
HAPS STUDIES AND COMPARISONS

1. DIRECT BEAM CALCULATIONS

The HAPS (High Altitude Prolate Spheroidal) code was developed at the Air Force Weapons Laboratory (AFWL) to provide means of determining the late-time electromagnetic pulse (EMP) signals from high-altitude nuclear detonations. By assuming a vertical geomagnetic field Maxwell's electromagnetic equations can be reduced to two spatial dimensions and time. A finite difference solution based on Knight's (Ref. 3) algorithm is the basis for the HAPS calculations. Late-time EMP effects, i.e., signals occurring after the initial gamma pulse, were observed for several source algorithms. Included as drivers were the direct beam of gammas, gammas outside the direct beam but scattered into the beam and neutrons arriving somewhat latter generating additional gamma rays. Electron currents arising from gamma induced Compton collisions were input to the HAPS code. Signals observed at several locations for local times up to 100 microseconds are presented.

The standard source package for the HAPS code has been a modified HEMP (Ref. 4) source algorithm known as the PROSOR* code. The basis for this direct-beam-only source approximation is from Erkkila (Ref. 5). PROSOR normally follows a spectrum of gamma rays exiting the weapon for a specified time distribution. Direct beam sources including Compton currents and ion densities are computed at selected locations in a non-self-consistent mode. PROSOR impacts the HAPS code by an interpolation to the HAPS field grid.

---

* Undocumented. PROSOR assumes a vertical geomagnetic field.

In order to compare late-time HAPS field results with direct beam results and other 1-D codes, the interpolation algorithm was completely changed. PROSOR direct-beam results for a typical weapon were curve fitted in the time range. Coefficients of the curve fits were interpolated in space, resulting in coefficients which could represent the source time history. By restricting the fitting function to a small number of constants, it was easier to vary the parameters representing the sources than it was to repeat the entire source calculation for as large an area as that covered by the 2-D codes. It was also possible to pass an arbitrary line of sight through the 2-D area covered by the source fits without the necessity of running special (or duplicate) runs for one-dimensional codes. In making 1-D and 2-D code comparisons, the PROSOR fitted data ensured also that both codes would be using identical sources rather than their own source routines.

A normal or standard PROSOR run consists of a matrix of sources which by specifying appropriate altitudes and horizontal range coordinates covers the area defined by a problem case. Physically, a record for each time step is written on tape containing four values, i.e., three currents and the secondary electron density for each of the matrix (grid) points. At each time step, the HAPS code reads a tape record and, depending on several options, interpolates from the source grid to the HAPS field grid.

In order to modify such parameters as rise or decay rate of the sources or to add an approximate first-scatter contribution, the PROSOR data were curve fit using each of the time histories for the currents and secondary densities. Once the rise and fall rates were determined, parametric changes could be readily made. A special code was written called PROFIT* which reads the PROSOR source tape and for each of the source

* Undocumented. PROSOR fitting code by J. A. Marks.

time history curves, 20 x 20 x 4 typically, determines appropriate constants to represent the time history according to the double exponential

$$J = A_o\left(e^{-\alpha(T-T_o)} - e^{-\beta(T-T_o)}\right) \qquad (1)$$

where T is the retarded (local) time, A_o, α and β were constants to be determined and T_o provided for adjusting the peak time. This function fits the direct beam currents quite well. Figures 1, 2, and 3 show example comparisons between the radial, theta and phi currents from PROSOR and PROFIT. Current densities are given in arbitrary units. These are typical of source region time histories. Higher altitude source pulses naturally last longer due to the reduced atmospheric absorption. In general, at the upper extremes of the source region, the double exponential function used was less satisfactory but this was acceptable since fields generated in the upper source region contribute proportionately less to fields observed near the earth's surface.

The double exponential function rises more rapidly near 3 shakes than the PROSOR results so that an exponential tail was used prior to 3 shakes. Only the values were matched at 3 shakes; consequently a Fourier analysis of resulting fields would present noise at the high frequency end. Since late time, i.e., low frequency, effects were sought, this assumption appears warranted and in addition saved the additional storage and time required to retain a more complex fit.

The secondary ion density used the following function:

$$A_o(1 - e^{-\alpha(T-T_o)}) \qquad (2)$$

More difficulty was encountered in matching the PROSOR secondary electron density using this simple function. An alternate model was provided by AFWL (see the Appendix) which integrated the radial current

analytically to obtain secondary electron density. The assumption made that the total current can be closely approximated by the radial current is made. This is acceptable since the effects of the transverse currents when added vectorially contribute typically 1-2% to the total current. Figure 4 shows the secondary electron density obtained by integrating the radial current in Figure 1. See Appendix A for integration model description.

Once the constants were determined, the standard interpolation routines in HAPS were used to obtain values representative of the source time histories. Several routines were written for inputting constants into the HAPS code and for reconstructing the sources at the field point of interest. For use in the 1-D codes the entire set of interpolation routines and associated data was gathered and integrated into the 1-D codes.

PROFIT output consists of the fitted constants for the entire source grid punched on cards. Approximately 1,000 cards are punched for a typical run. The time history curve generated by the fitted constants is overlayed on microfilm with the original PROSOR data. The generated time history is plotted as a dashed line and the original data is plotted as a solid line. For most comparison runs between 2-D and 1-D codes, a typical 100 km burst set of fitted constants was used. Punched cards from PROFIT were used to create a common file (ELEP226) on the AFWL computers. This file contains the PROSOR 22-6 set of data. A typical comparison between HAPS and HEMPB (see Ref. 6) is shown in Figures 5 and 6 for the direct beam PROSOR fits described. The observer location is at an altitude of 10 km and horizontal range of 360 km. A flat earth and vertical geomagnetic field were assumed.

2. FIRST SCATTER CONTRIBUTION APPROXIMATIONS

The normal PROSOR code and the HEMP code produce source representations of the Compton currents and secondary ion densities from a high

altitude nuclear burst. The approximations used in the codes have been well documented by Erkkila (see Ref. 5). Since these sources consider the currents resulting from the direct beam of gamma rays only, an estimate of the effects caused by currents resulting from scattered gamma rays could be estimated by enhancing the direct beam calculation. AFWL had a project underway to not only improve the direct beam calculations, but also to include the first scatter contribution by using a Monte Carlo algorithm. Since these results were not yet adaptable to the HAPS code, a simplified approximation was used based upon a first scatter calculation documented in the AFWL EMP Handbook (see Ref. 7). The handbook depicted for one particular altitude and range the first scatter contribution compared to the direct beam result. HAPS approximated this additional current by adding 5% of the peak current starting 2 shakes* after the current peak. This contribution decreased with a 2×10^{-7} sec^{-1} decay constant. Plots of the three currents for a typical source region observed are presented in Figures 7 through 9. Comparisons showing effects on the electric fields for a typical 100-km burst were made using the direct beam only source and the direct plus scatter source fits. In both cases the secondary electron density was based on the direct beam fits only. A typical source region conductivity is depicted in Figure 10.

Comparisons of typical electric fields for source region and near ground observers are presented. The source region observer located near the bottom of the source pancake is at an altitude of 20 km and at a horizontal range of 200 km. The lower observer was located at 10 km at a horizontal range of 360 km. A vertical downward geomagnetic field and flat earth approximation were used for the comparison. Source region electric fields are shown in Figures 11 to 13 and near ground fields in Figures 14 to 16. The radial electric fields are increased by less than a volt/meter. The

*A shake is 10^{-8} seconds.

radiated electric fields are enhanced by 2 to 6 volts/meter in the 1 to 20 microsecond region. Enhancement thereafter is approximately one volt/meter. An integration of the currents yields a 20 to 25%. The scattering effect, however, extends over a greater period of time (20 microseconds) than the direct beam portion of the current. There appears then a direct correspondence between the current injected and the late time fields. In the frequency range, the low frequencies and DC end can be expected to increase proportionately as well.

Additional results for many other observers can be found in the AFWL-EMP film library.

Source calculations as supplied by AFWL are not in a format suitable for inputing directly into a 2-D code such as HAPS. Source calculations generally stem from line-of-sight calculations directed outward from the burst. At each given range, sources are computed for the time history desired and then for the next range and so on. Additional lines-of-sight may be determined using the same format of a complete time history at each of the range steps.

A two-dimensional calculation requires several lines-of-sight or the equivalent in order to cover the large area described by the 2-D calculation. In addition, it is necessary to know the sources at all ranges (or all space points) for a specific time. An ancillary code, RORDER (see Ref. 8) was written that records the line-of-sight data as the total volume of data precludes storing it in central memory and/or ECS and merely addressing the data desired.

RORDER uses ECS to temporarily hold a limited number of time steps for all ranges and lines-of-sight. These are then read out of ECS and written on tape in a 2-D tape format. The next limited number of time of steps is stored in ECS and again read out for transferring to tape. Inputs to RORDER consist simply of the number of time steps, number of lines-of-sight and number of range steps.

AFWL was nearing completion of its first-scatterer-source calculations near the end of the contract under which this work was performed. Their initial results (see Ref. 6) were for a line-of-sight straight down from a plane-wave source with a magnetic field at 30^{o} sight. In order to estimate 2-D effects, this single line-of-sight source calculation was input both the 1-D HEMPB code and the 2-D HAPS code. Sources were scaled to a burst height of 150 km. HAPS used the same vertical lines-of-sight sources and scaled in range for all angles across a grid extending to 150 km. Air chemistry was based on the vertical downward air density so that fields obtained should be representative of a spherical wave at 30^{o} to the geomagnetic field. Currents used are given in Figures 17 to 19 for an altitude of 30 km. These are contrasted to the standard direct beam sources normally obtained without the recent scattered contribution. Corresponding electric fields at the same location (source region) are shown in Figures 20 to 22. Only the slightest difference in field strength is apparent between the HEMPB and HAPS codes. No significant fields appear after a few microseconds due to the sustained conductivity levels. An observer located at 15 km shows typical electric fields as well (see Figures 23 to 25). Radial fields differ slightly. Phi fields from HAPS remain in the 1-10 volt/meter range while the 1-D results die rapidly after a few microseconds. The theta field from HAPS displays the dipole or air asymmetry signal in the 10 volt/meter region. The 1-D theta field naturally proceeds to zero as the currents and after a few microseconds is below 1 volt/meter. A 10-km radial electric field, Figure 26, is presented to show the typical dipole effect below the source region. Theta and phi fields at 10 km are almost identical in shape to those at 15 km.

3. CAUSALITY

In order to determine causality (i.e., whether perturbations travel across the HAPS grid in the proper time), several runs were made with the

HAPS code with varying behaviors of the sources in order to observe the effects.

Signals observed at a point resulting from effects not on a line-of-sight should travel across the grid at the speed of light. All signals on an ellipse having as its foci the source point and the observer point require the same transit time in order to reach the observer point. The sum of the principal radii of the ellipse determines the transit time. As time increases, the ellipse enlarges, thus covering a larger area. Boundary effects, not troublesome at early times due to the very narrowness of the ellipse about the line-of-sight between the burst and observer, can become dominant at very late times comparable to the grid dimension divided by the speed of light.

Using the PROSOR fitted source data as the driver, a base case was run using a typical 100 km burst height with vertical geomagnetic field over a flat earth. An observer on the ground at a horizontal range of 400 km was selected. This represents a line-of-sight of approximately 76^{o} (as measured from the lower vertical axis). An ellipse equivalent to 10 microseconds, i.e., no effects should be observed for retarded times less than 10 microseconds, was also chosen. Three runs were made with different algorithms used for adjusting the sources at end beyond the 10-microsecond ellipse (see Figure 27). It was found, as was expected, that too abrupt a change in the sources could affect the code stability, and by trial and error a nominal perturbation at the ellipse was found. Sources were varied outside the 10-microsecond ellipse by the prescription

$$S = S_o e^{-\epsilon(\lambda-\lambda_z)/\Delta\lambda} \quad \text{for } \lambda > \lambda_z \tag{3}$$

where

λ = distance from burst to grid point to observer

λ_z = distance from burst to ellipse to observer

$\Delta\lambda$ = distance covered by light in 10 microseconds.

Cases with sources decreased were run with ϵ values of 1.0 and 2.0. A case with increasing sources outside the ellipse was run for ϵ of 1.0 with sources adjusted as

$$S = S_o 1 - e^{-\epsilon(\lambda-\lambda_z)/\Delta\lambda} \qquad \text{for } \lambda > \lambda_z \tag{4}$$

Figures 28 through 30 show the effects on the electric fields due to perturbing the sources along the 10 microsecond ellipse. Each figure shows values obtained from four separate runs labeled A, B, C, and D. The base case, labeled A, is compared to two cases, B and C, in which the sources decreased along the ellipse and one case, D, which has the sources increased along the ellipse. Although the method of adjusting the sources was quite arbitrary, the important result is that fields at the observer begin to be affected at very nearly the correct transit time, 10 microseconds. The fields begin to change a few microseconds before they should because of the manner which the sources were attenuated away from the ellipse. The conclusion one can draw is that HAPS, when suitably used, correctly predicts the manner in which signals can pass through the grid.

4. SCATTER GAMMA-RAY AND NEUTRON EFFECTS

An estimate of the effects produced by both scattered gammas and neutrons was made by combining AFWL scatter gamma and neutron sources with the direct-beam PROSOR (HEMP) type sources.

AFWL supplied analytic source fits for scattered gamma and neutron effects for a 20 km burst scaled from data for a ground burst case. Source

fits consisted of the three Compton currents and integrated number of secondary electrons as a function of altitude and range coordinates. The AFWL-supplied sources were based on 2-MeV gamma rays and 14-MeV neutrons processed by an AFWL Monte Carlo code for a ground burst. By adjusting mean free path lengths, the burst was scaled to 20 km. The results presented are meant to indicate the trends in field effects by the inclusion of these additional source terms. Including the neutron effects markedly enhances the late time fields.

Direct beam sources were supplied by the PROSOR code up to one microsecond after which an exponential tail was added to allow for the approximate decay following one microsecond. In general, the only direct beam source of any significance is in the very high altitudes above the burst and these do not contribute to fields observed at or near the ground.

After defining the appropriate grid covering the region around the burst to approximately 45 km ground range, the field calculation was made to 100 microseconds. Problems with the close-in field calculation required an approximate J/σ calculation for the region near the burst where very high conductivities can introduce oscillations in the field calculations.

Three separate runs were made and compared: (1) direct beam sources only, (2) direct beam and scattered gammas, and (3) direct beam, scattered gammas and neutrons. Time history plots for observers located at numerous locations in the field grid are in AFWL-EMP microfilm library.

Figure 31 shows the typical radial current enhancement by adding the scattered gamma and neutron contributions. The conductivity enhancement can be seen in Figure 32.

Figure 33 shows the total electric field contours at 50 microseconds and depicts the locations in the HAPS grid of three observer locations described here. The local radial electric field for observers at co-altitude (burst height), ground range 12 km and altitude 8 km, ground range 4 km,

as shown in Figures 34 and 35. Failure to include the ionic recombination terms in the air chemistry equations resulted in higher conductivities than should be observed at the lower altitudes.

Fields near the ground, radial and radiated, for an observer at 4 km altitude and 20 km ground are given in Figures 36 to 38. These exhibit the same general behavior as near earth fields obtained by Parkinson (Ref. 9). The radiated transverse electric phi fields, Figure 26, are dominated entirely by the neutrons at later times. Theta fields, Figure 37, which exhibit the signal as a result of the air density asymmetry retain the same three cross-overs in the first 100 microseconds. The first cross-over occurs as the dipole signal overrides the geomagnetic turning spike. Naturally, the lower altitude burst produces a dipole signal that dominates sooner than a higher altitude burst. Scattered gamma and neutron currents cause the first cross-over to occur up to two shakes later but are unable to drive the fields directly. Instead they generate a larger dipole signal. Second cross-overs occur later due to the stronger dipole effect. The third cross-over for the case in which all currents are combined occurs very late due again to the stronger dipole effects. Radial fields, Figure 38, build more slowly from the same mechanism as the dipole signal where the field may be thought of as a measure of the curvature (nonplane characteristics) of the theta field in the region around the observer.

5. MISCELLANEOUS

A damping algorithm that had been applied with some success in the HAPS code consisted of averaging successive time steps in order to remove small oscillations resulting from lack of convergence. This algorithm was applied infrequently, generally on the order of every 10 time steps as the calculation proceeded. Enough success had been realized with the averaging being used that the method was incorporated somewhat directly into the difference equations. The old damping algorithm required saving an additional

complete grid of all six fields, thus requiring additional disk and peripheral process or time. The present algorithm computes the fields for a time step twice that which is input and averages the new and the old field in time to the input time step. By suitably adjusting constants as the calculation proceeds and by saving an extra coordinate line's set of fields, the averaged fields can be set in and replace the old fields very much as is normally done in the code.

The problem of switching from one time step to a larger time can cause a hitch or bump in the fields if the sources are not specified at the proper time points through the switch. Since the differencing is centered about a point one-half ΔT back from the new time point, sources at the one-half ΔT point are used. For constant ΔT's throughout the time covered by the problem use of sources centered back one-half ΔT when they should be at the new time introduces a small error rather uniformly throughout. For source sets where the time step increases (or decreases), it is necessary to position sources at the new times or interpolate the old one-half ΔT back sources to the full ΔT times. Most of the recently devised analytic source packages allow sources to be obtained at any arbitrary time.

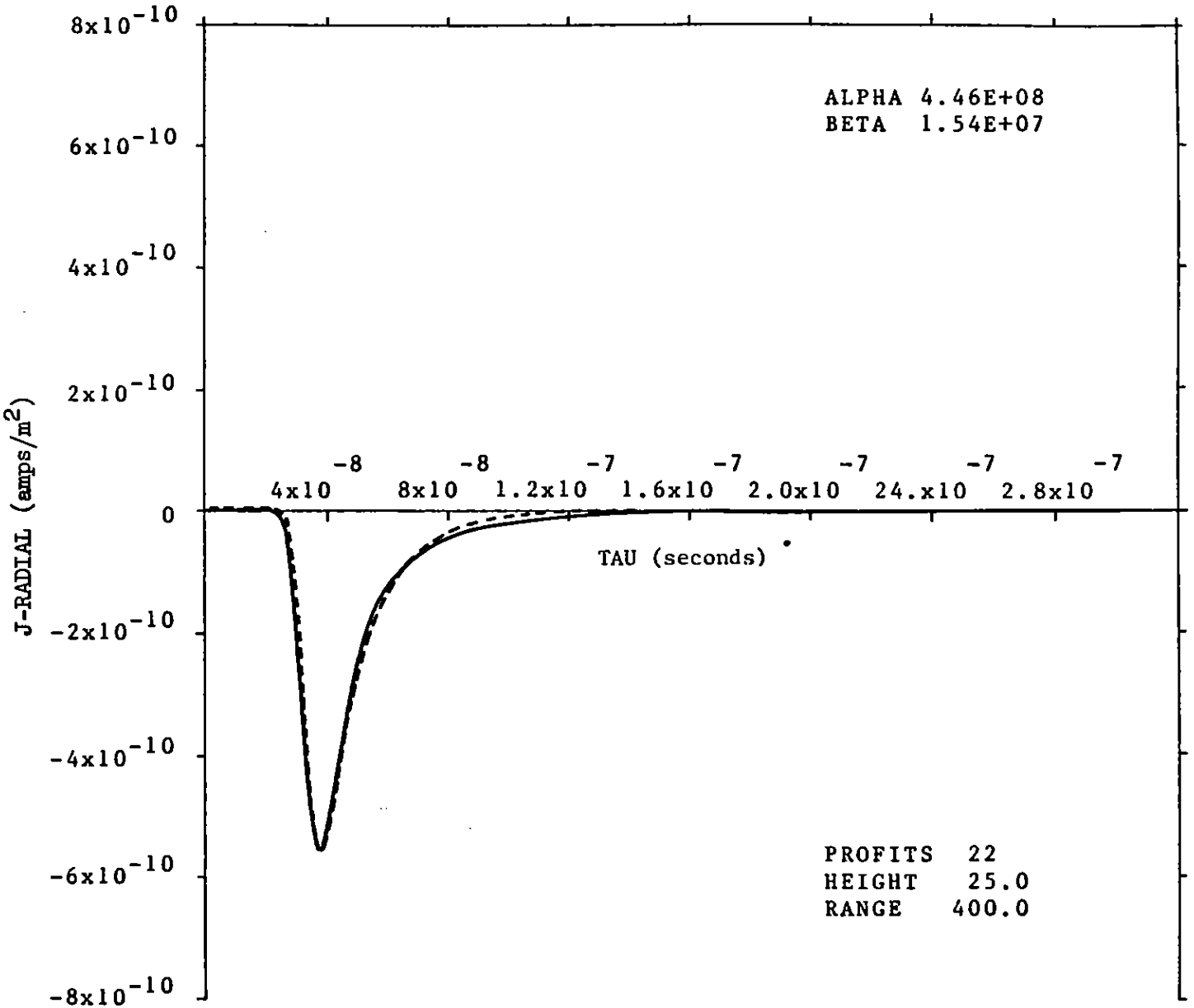

Figure 1. J Radial Comparison of PROSOR and Fitted Data.

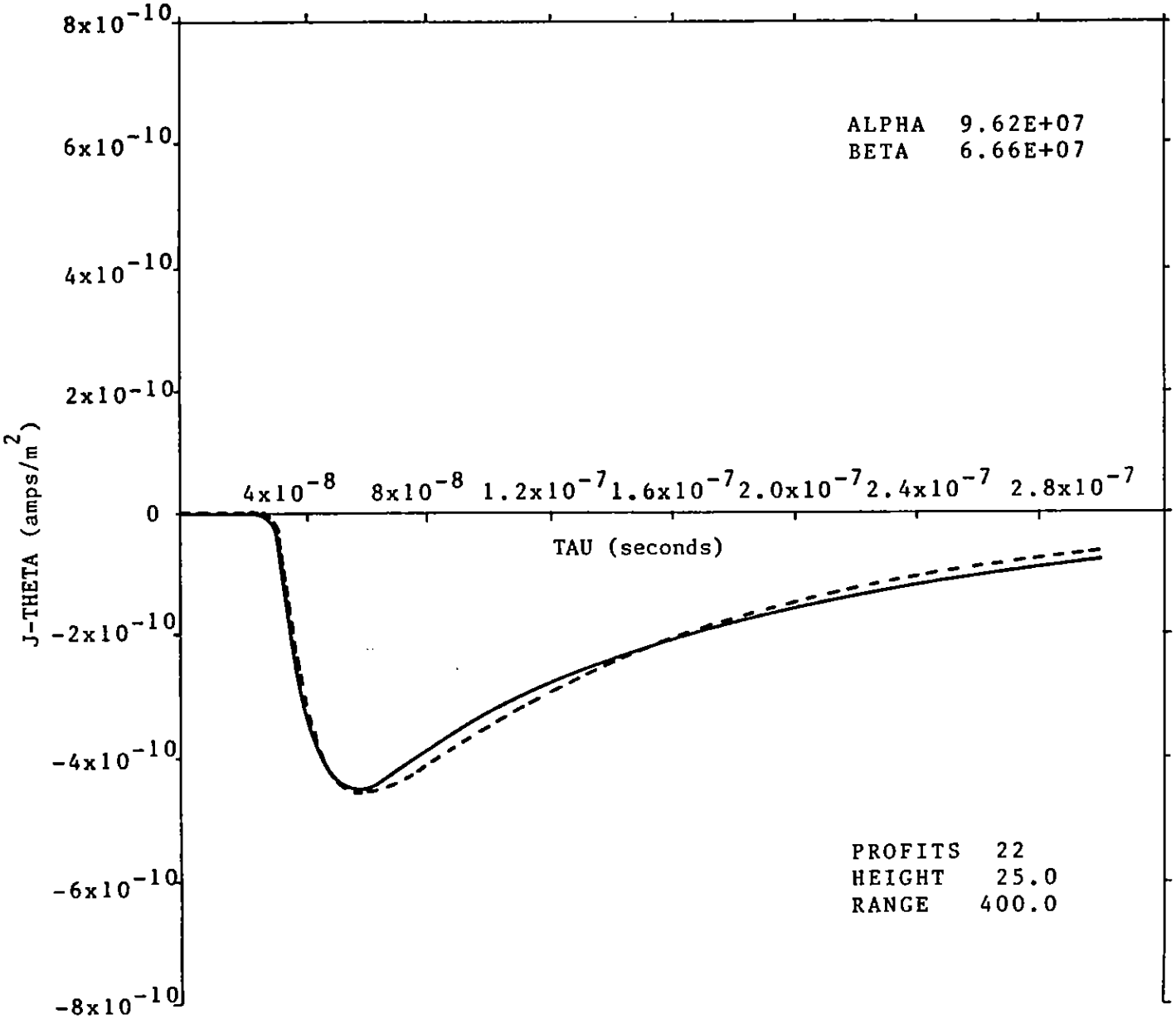

Figure 2. J Theta Comparison of PROSOR and Fitted Data.

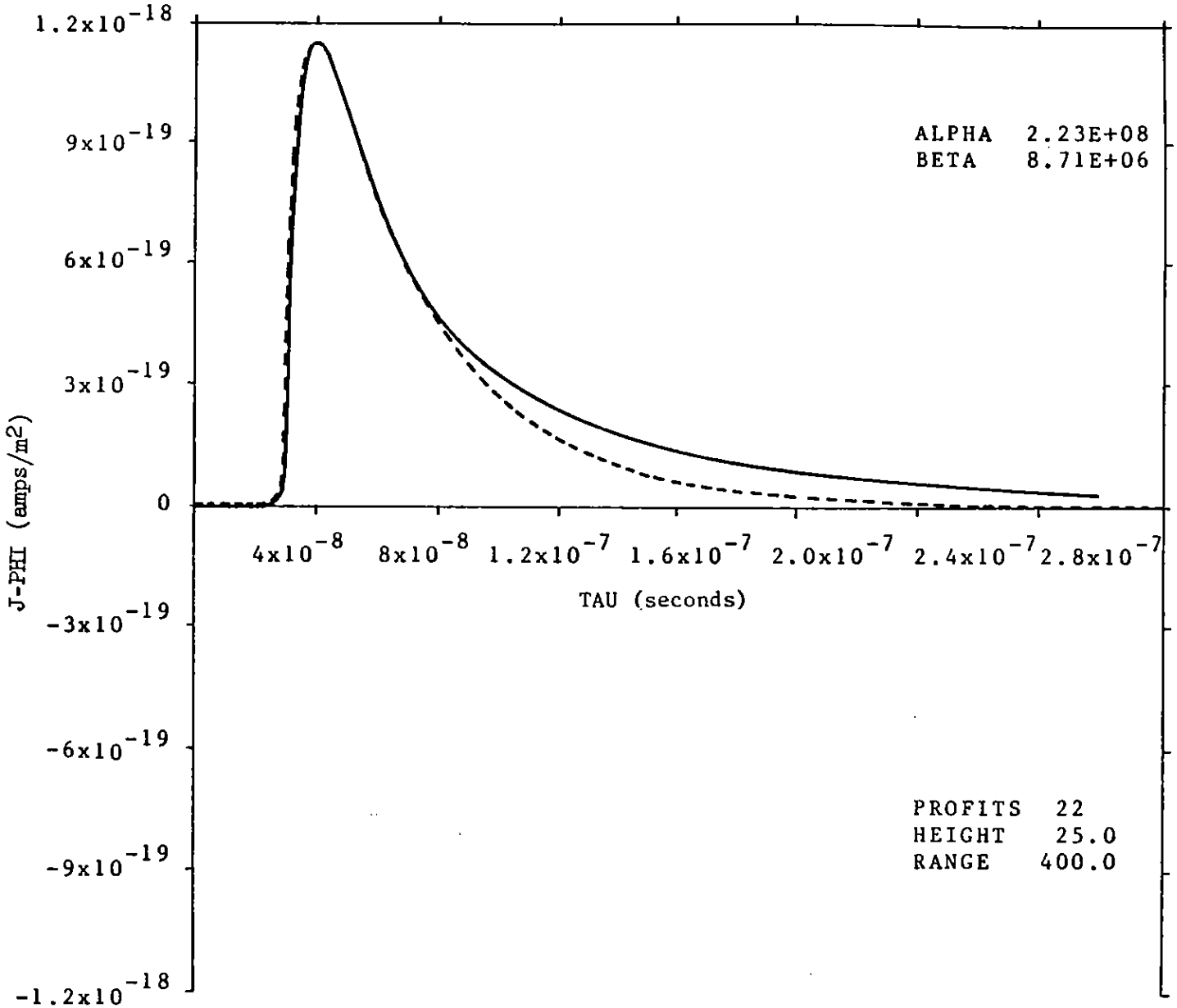

Figure 3. J-Phi Comparison of PROSOR and Fitted Data.

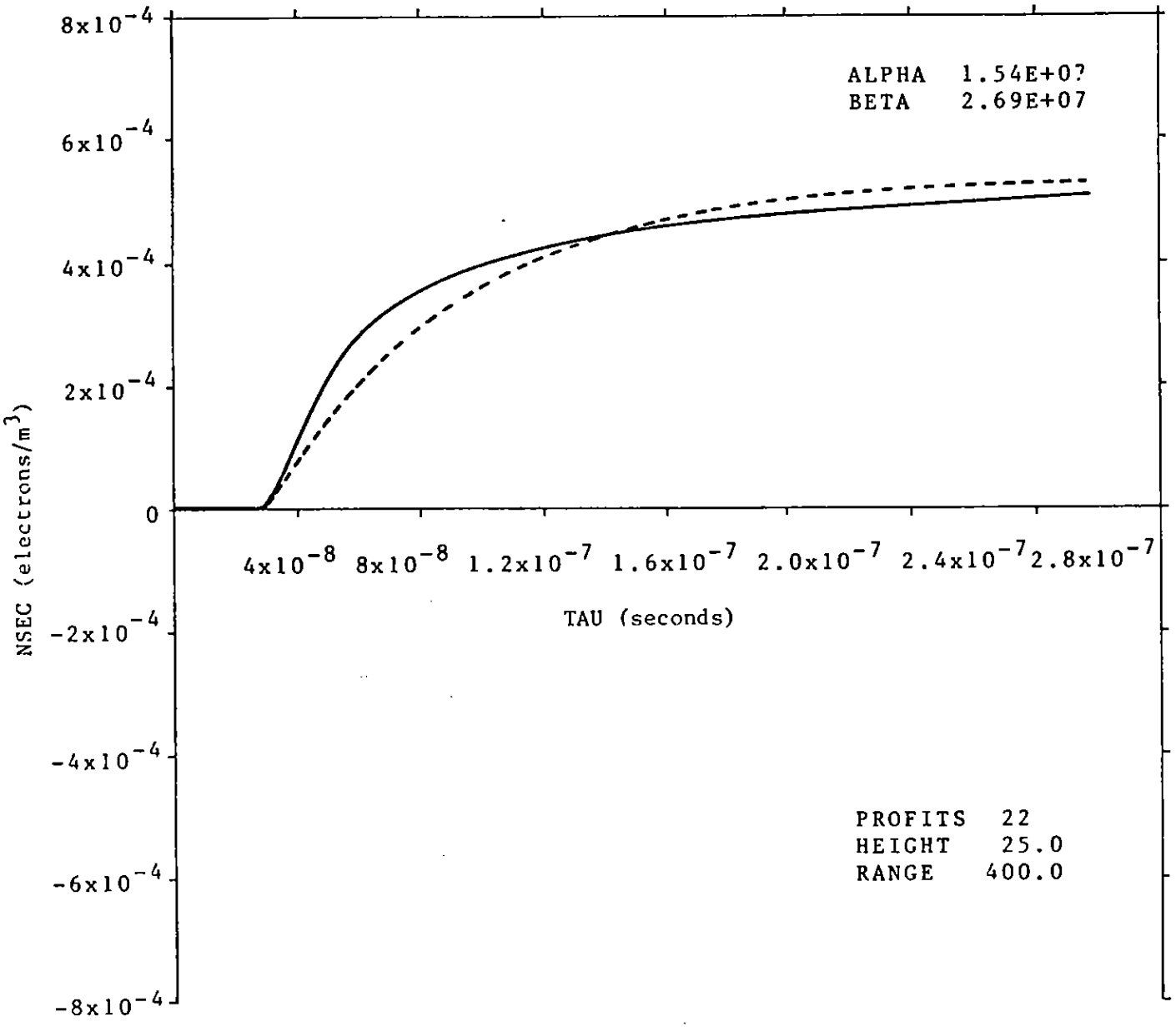

Figure 4. Secondary Electron Density Comparison of PROSOR and Fitted Data.

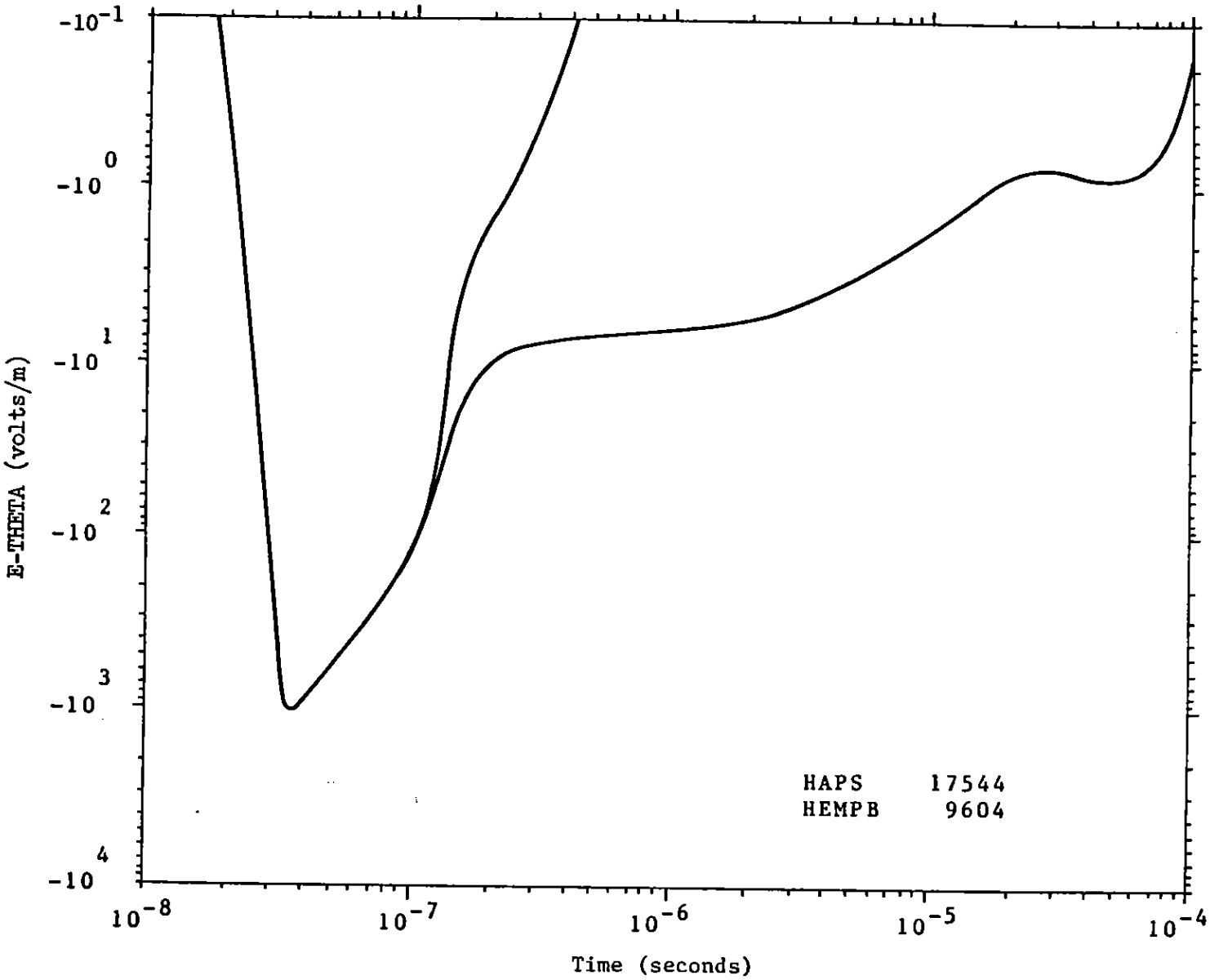

Figure 5. Typical E-Theta from HAPS Using the PROSOR Fits.

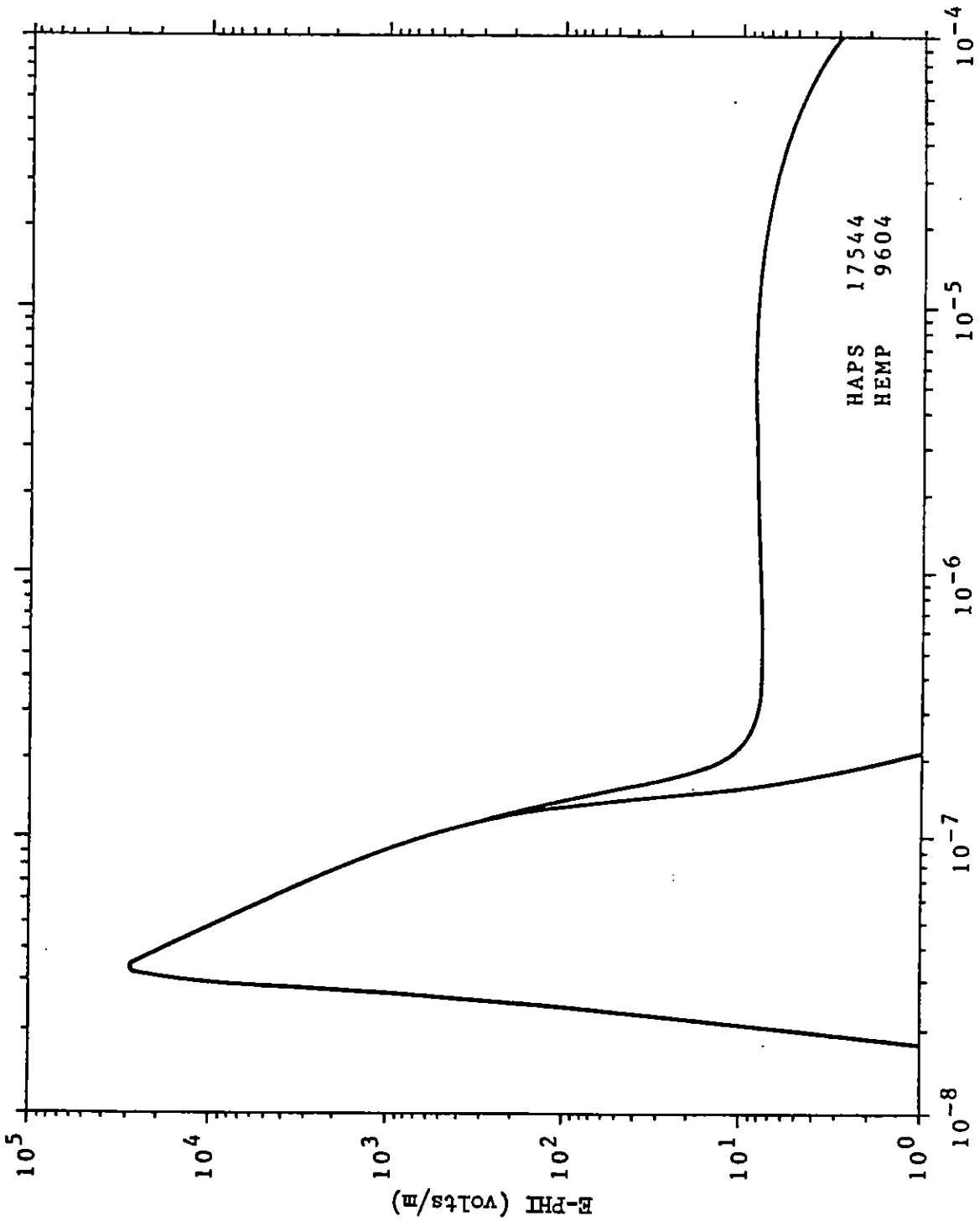

Figure 6. Typical E-Phi from HAPS Using the PROSOR Fits.

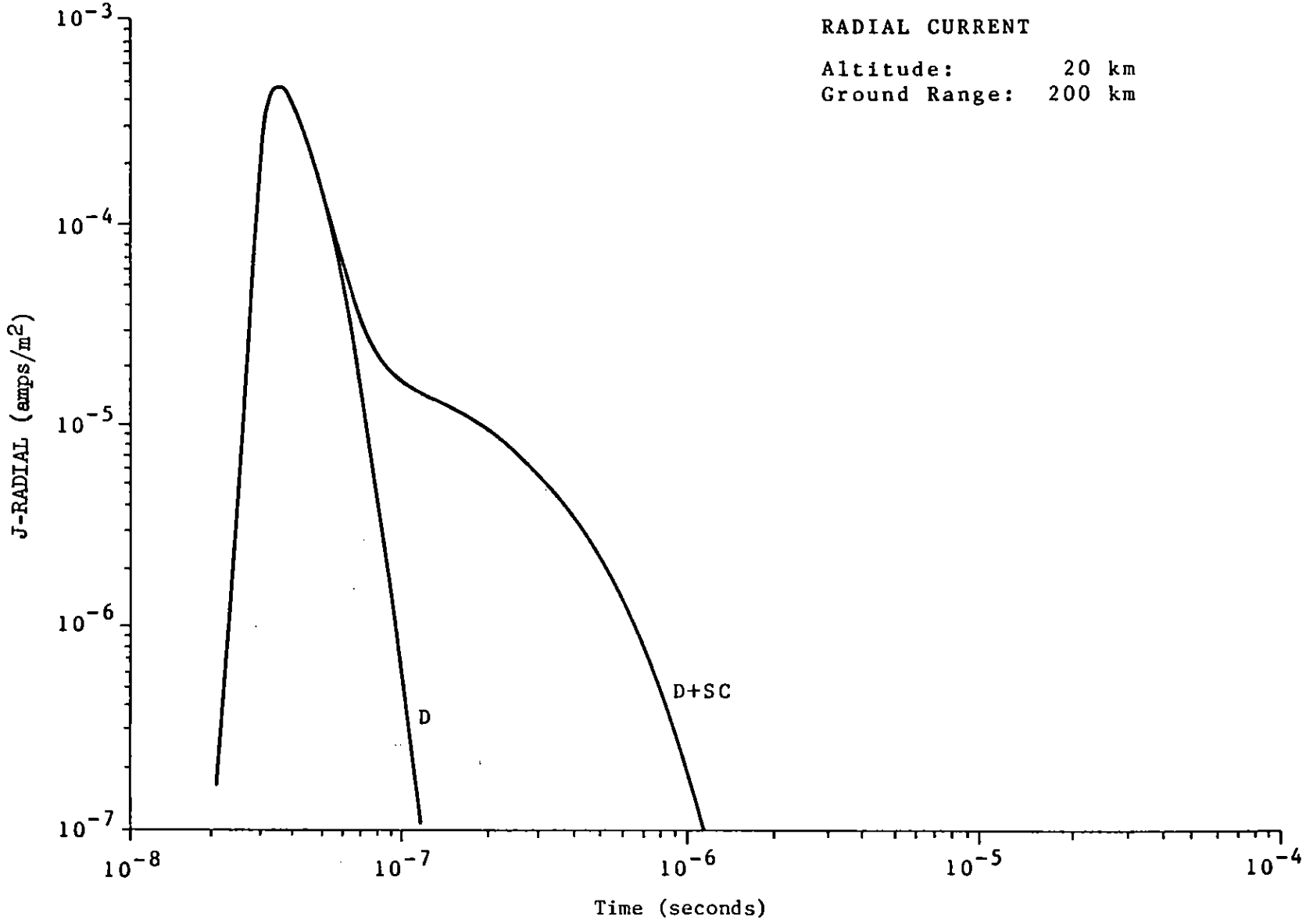

Figure 7. Radial Current for Direct Beam and Direct Plus Scattered.

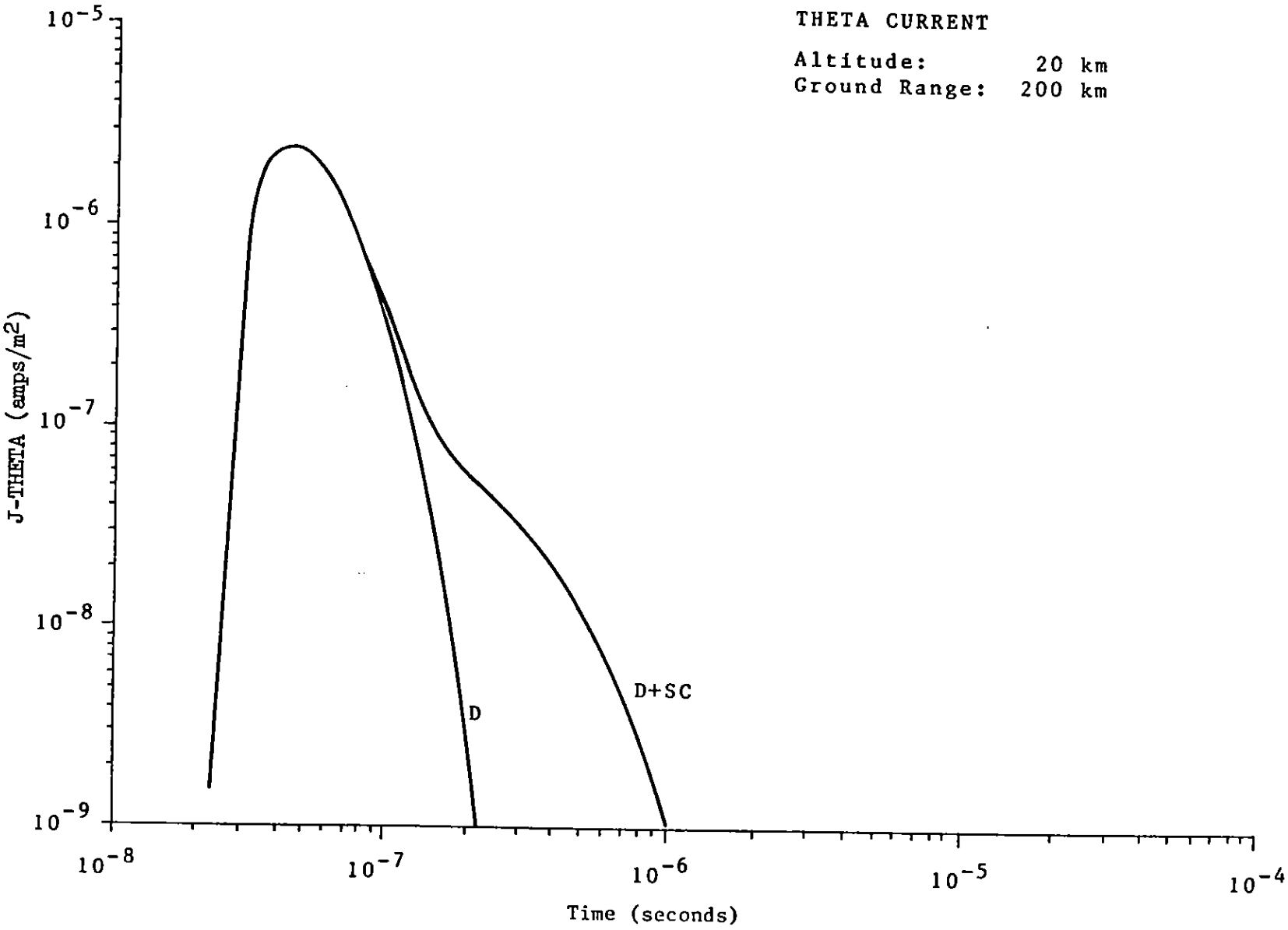

Figure 8. Theta Current for Direct Beam and Direct Plus Scattered.

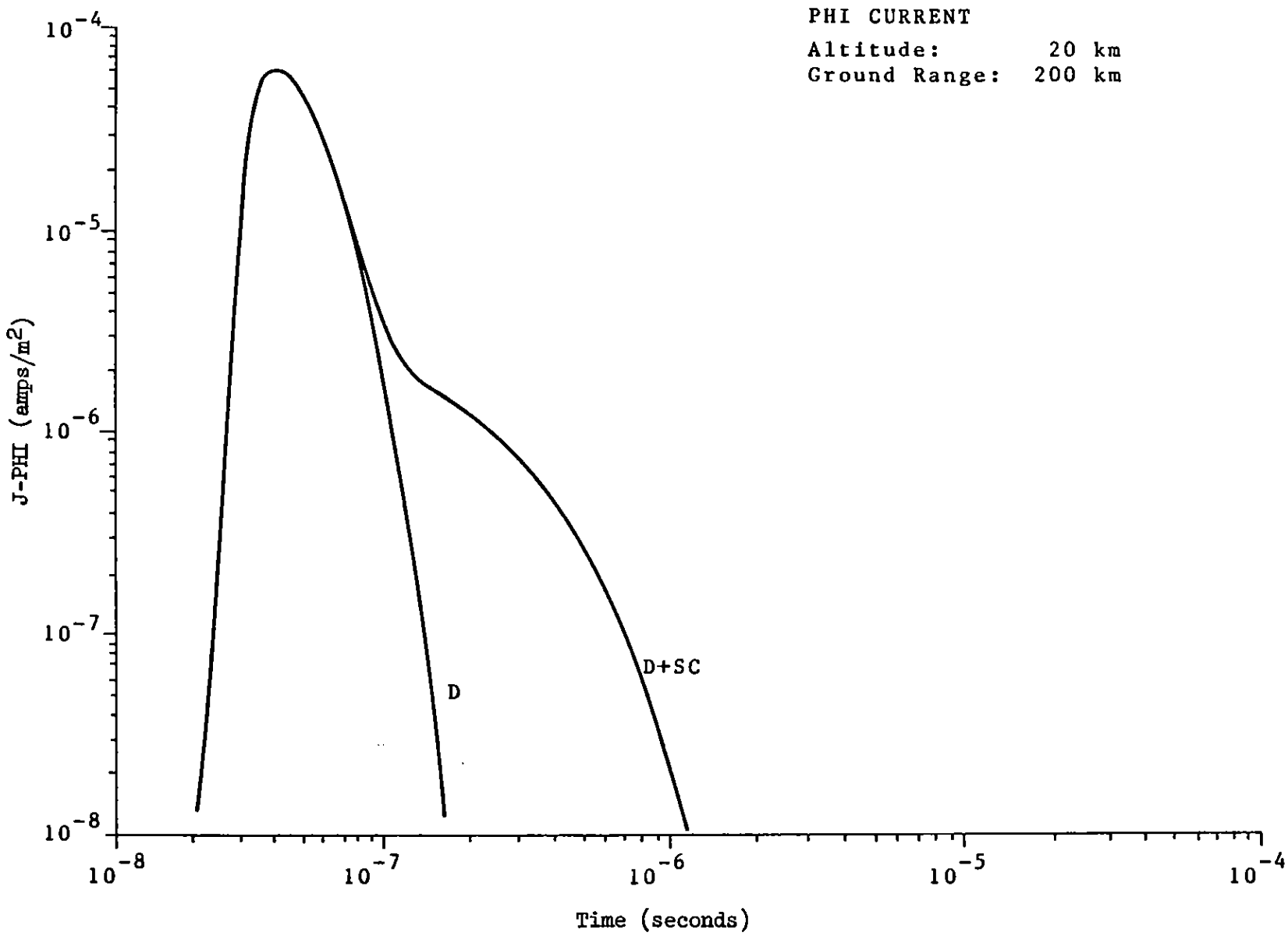

Figure 9. Phi Current for Direct Beam and Direct Plus Scattered.

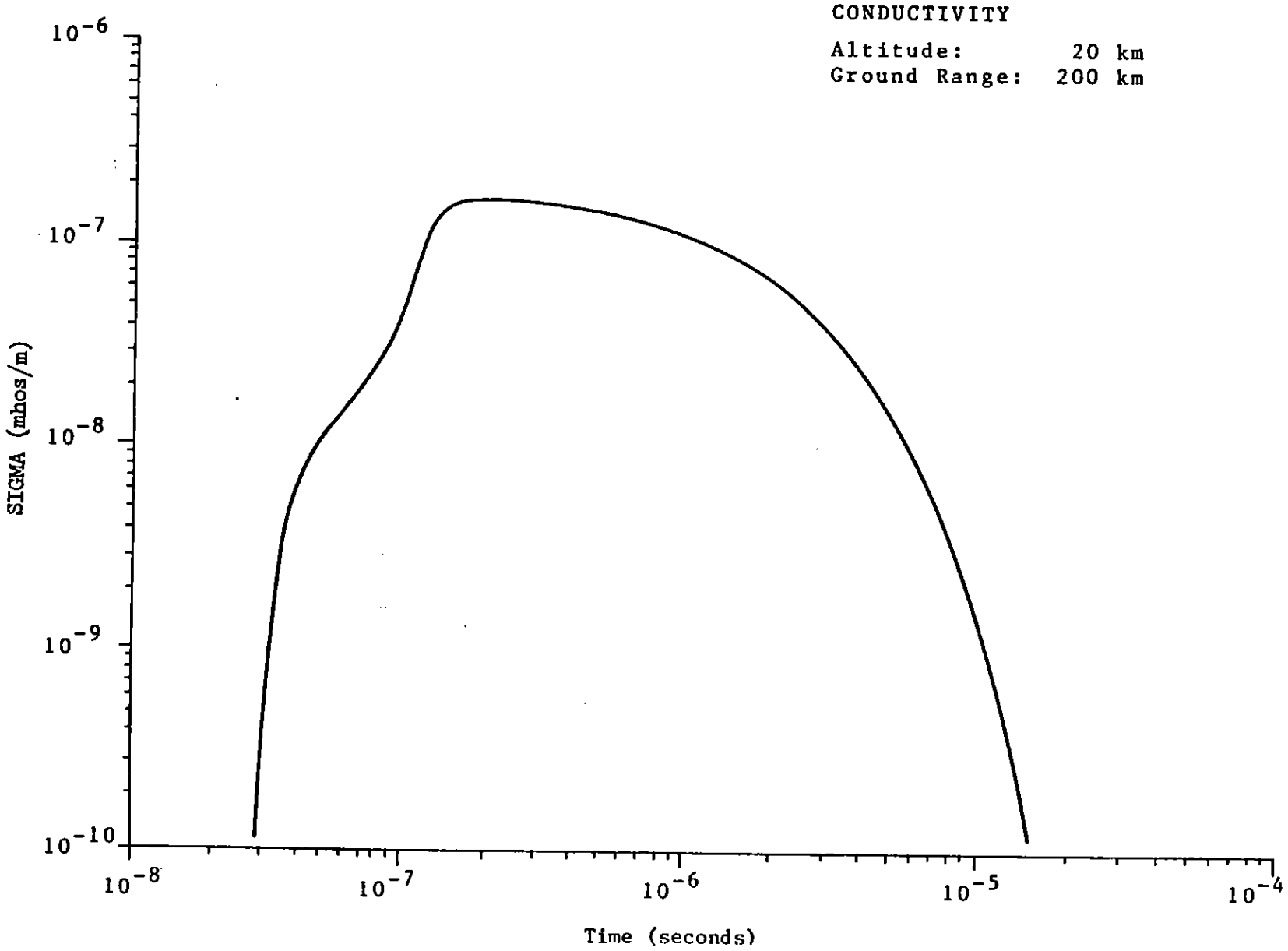

Figure 10. Conductivity Used in Both Direct and Scattered Problem.

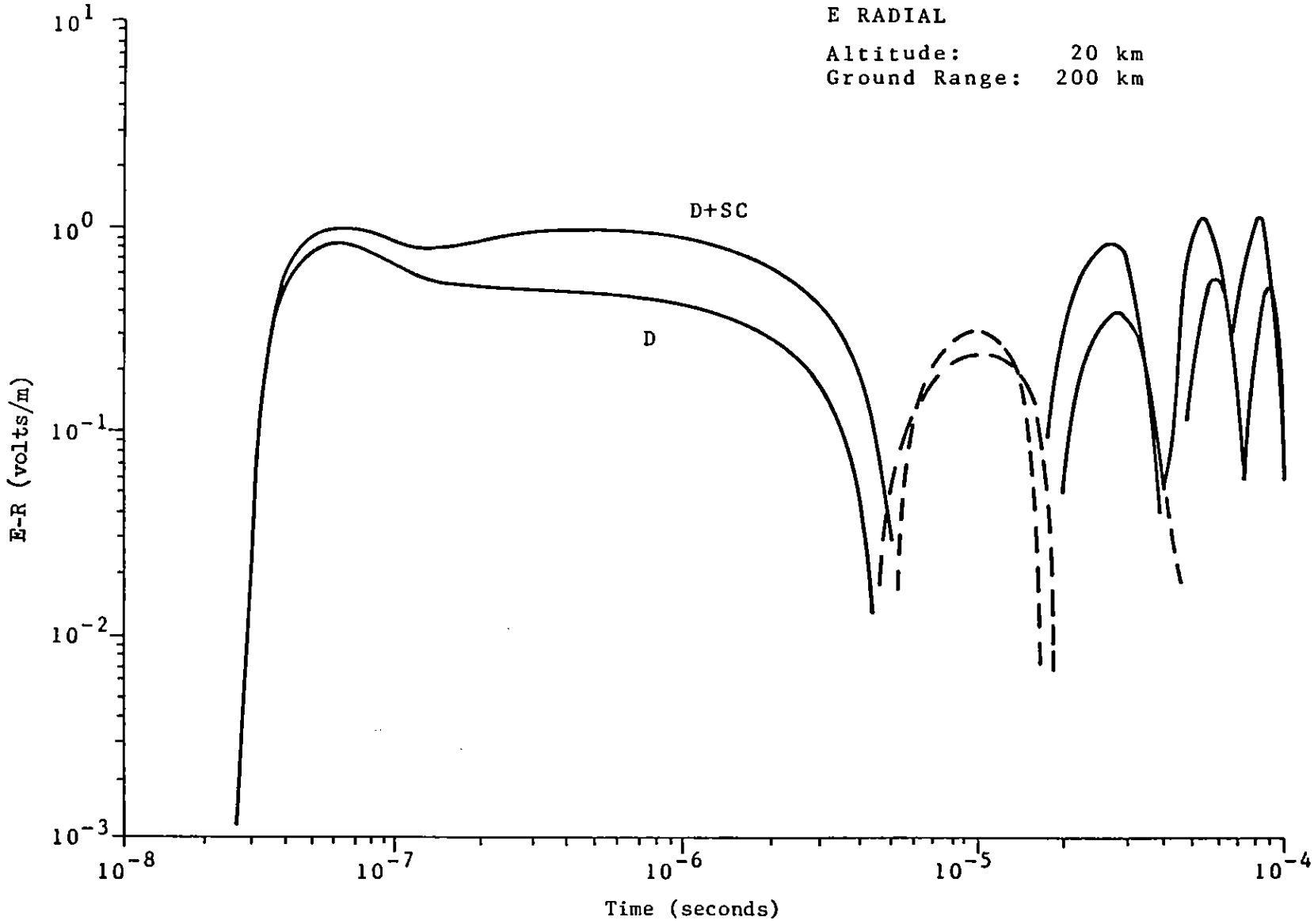

Figure 11. Radial E Field for Direct Beam and Direct Plus Scattered.

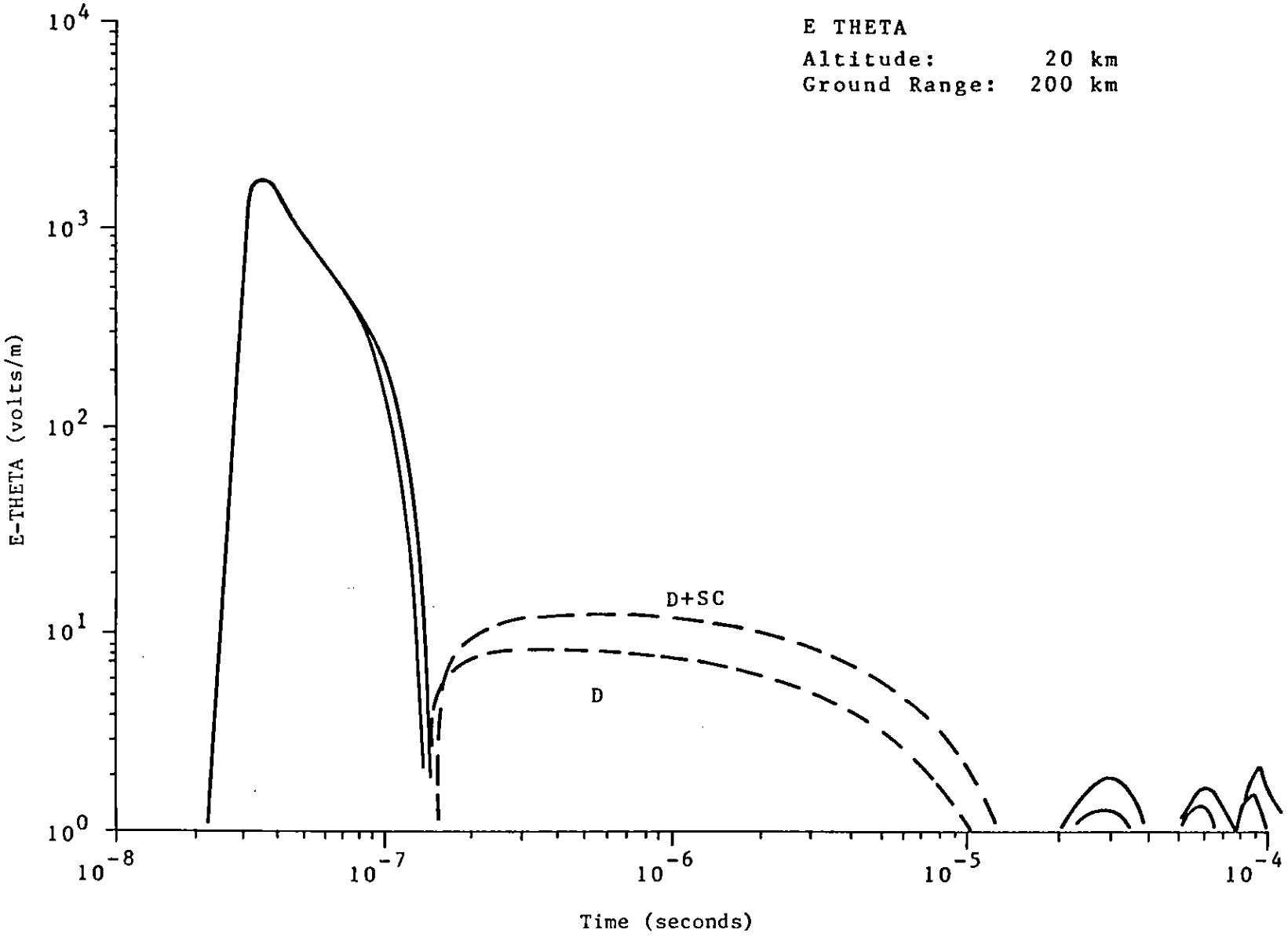

Figure 12. Theta E Field for Direct Beam and Direct Plus Scattered.

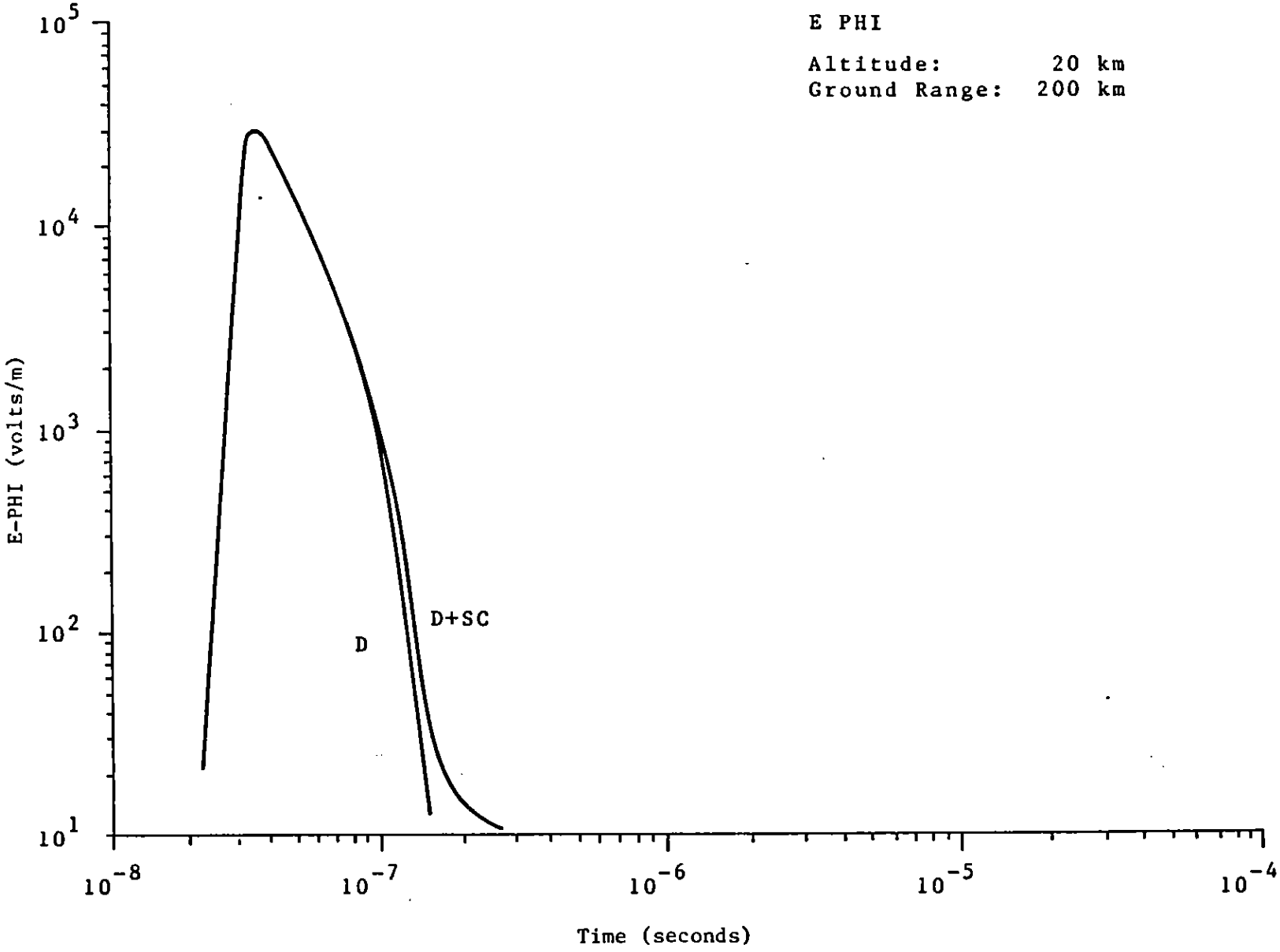

Figure 13. Phi E Field for Direct Beam and Direct Plus Scattered.

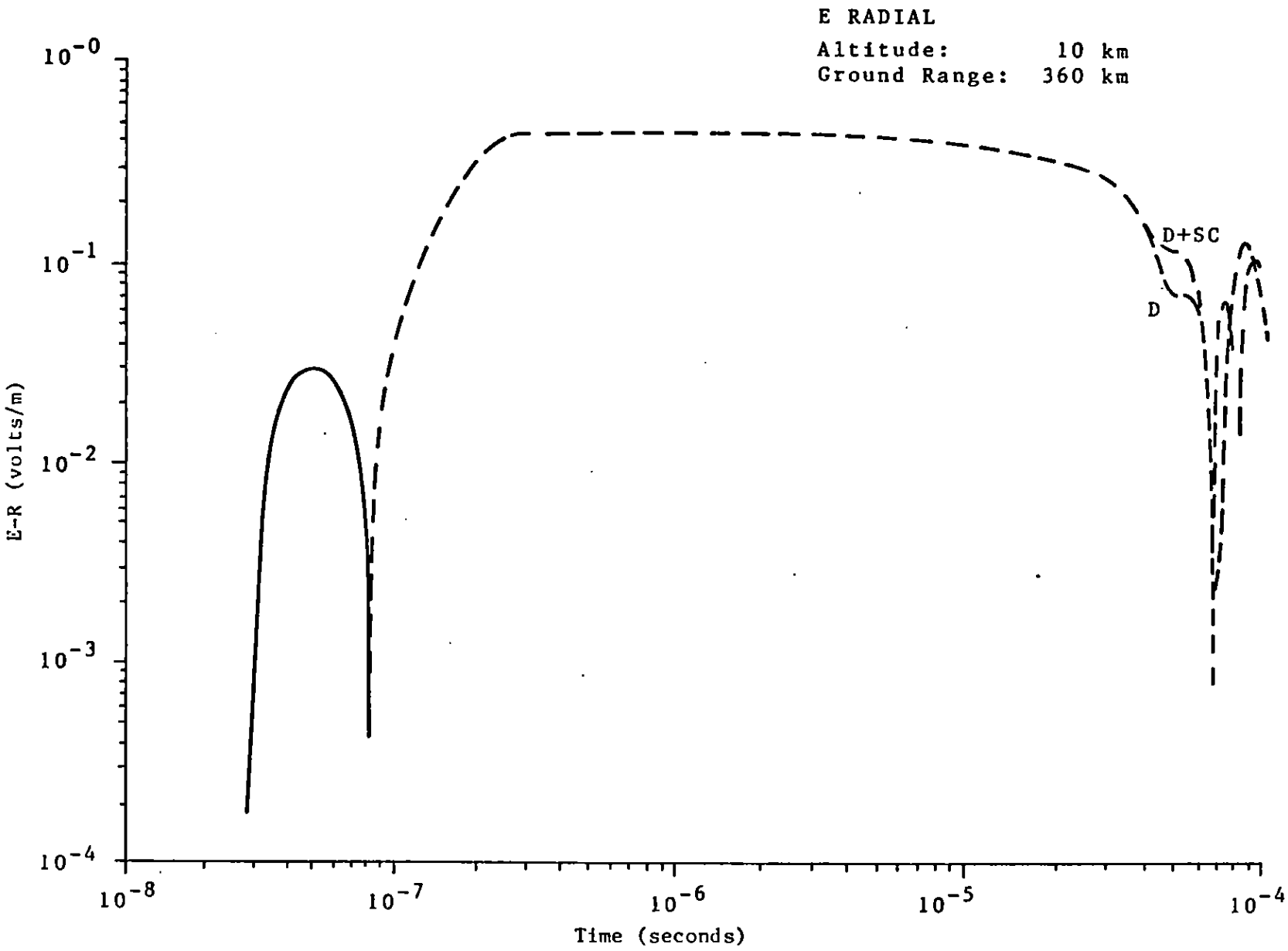

Figure 14. Radial E Field for Direct Beam and Direct Plus Scattered.

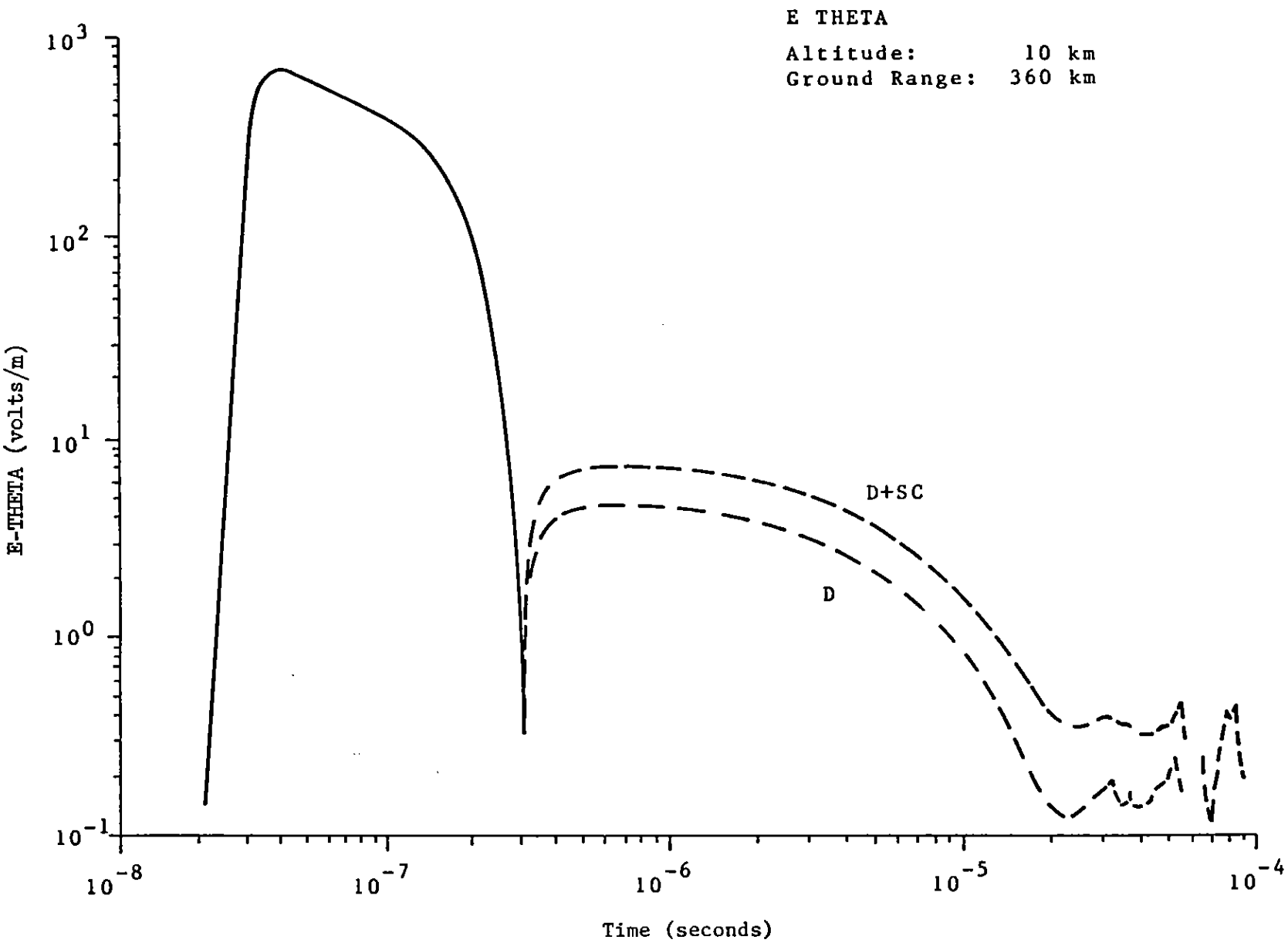

Figure 15. Theta E Field for Direct Beam and Direct Plus Scattered.

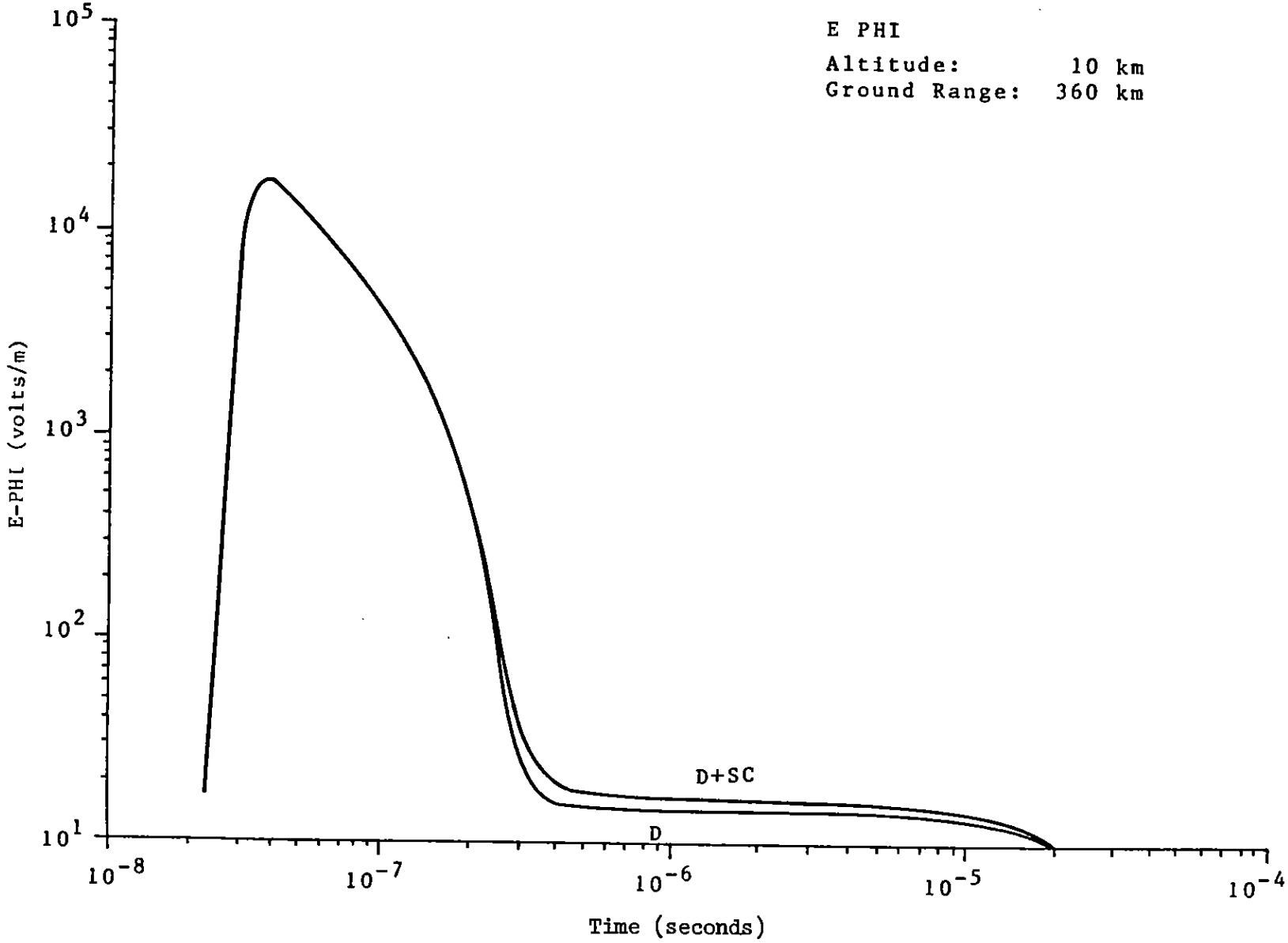

Figure 16. Phi E Field for Direct Beam and Direct Plus Scattered.

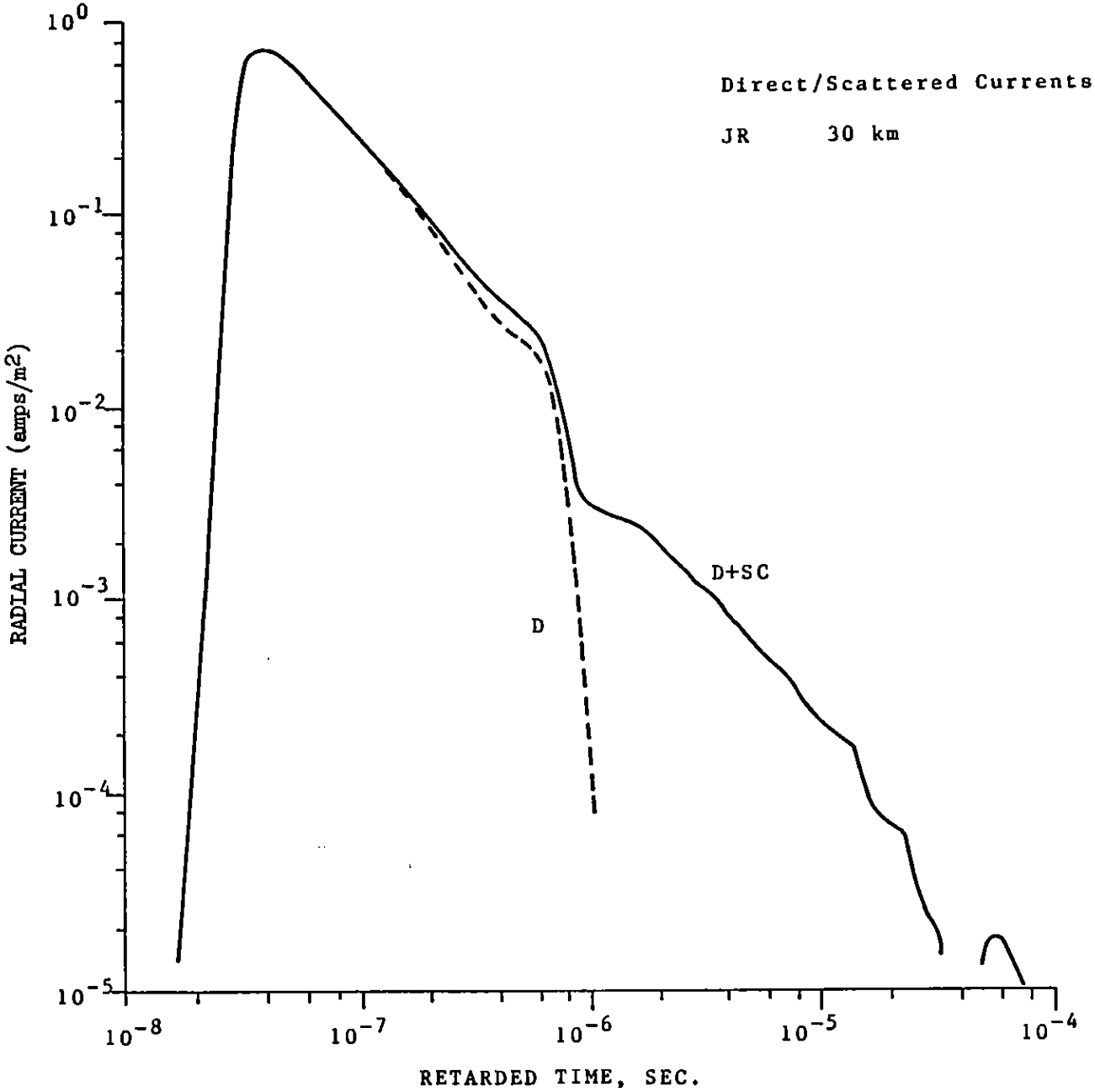

Figure 17. Direct/Scattered Currents, JR

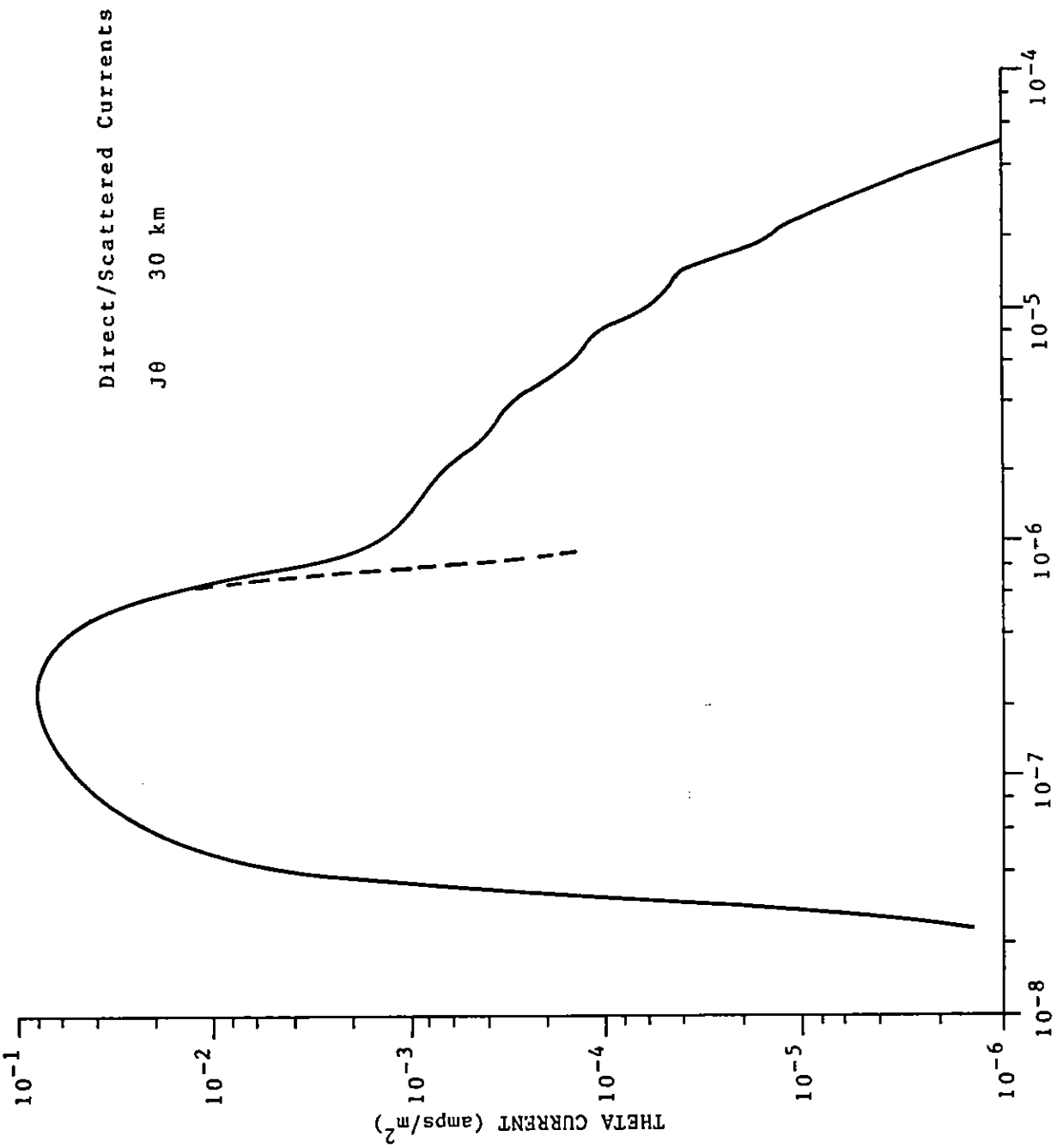

Figure 18. Direct/Scattered Currents, J-Theta.

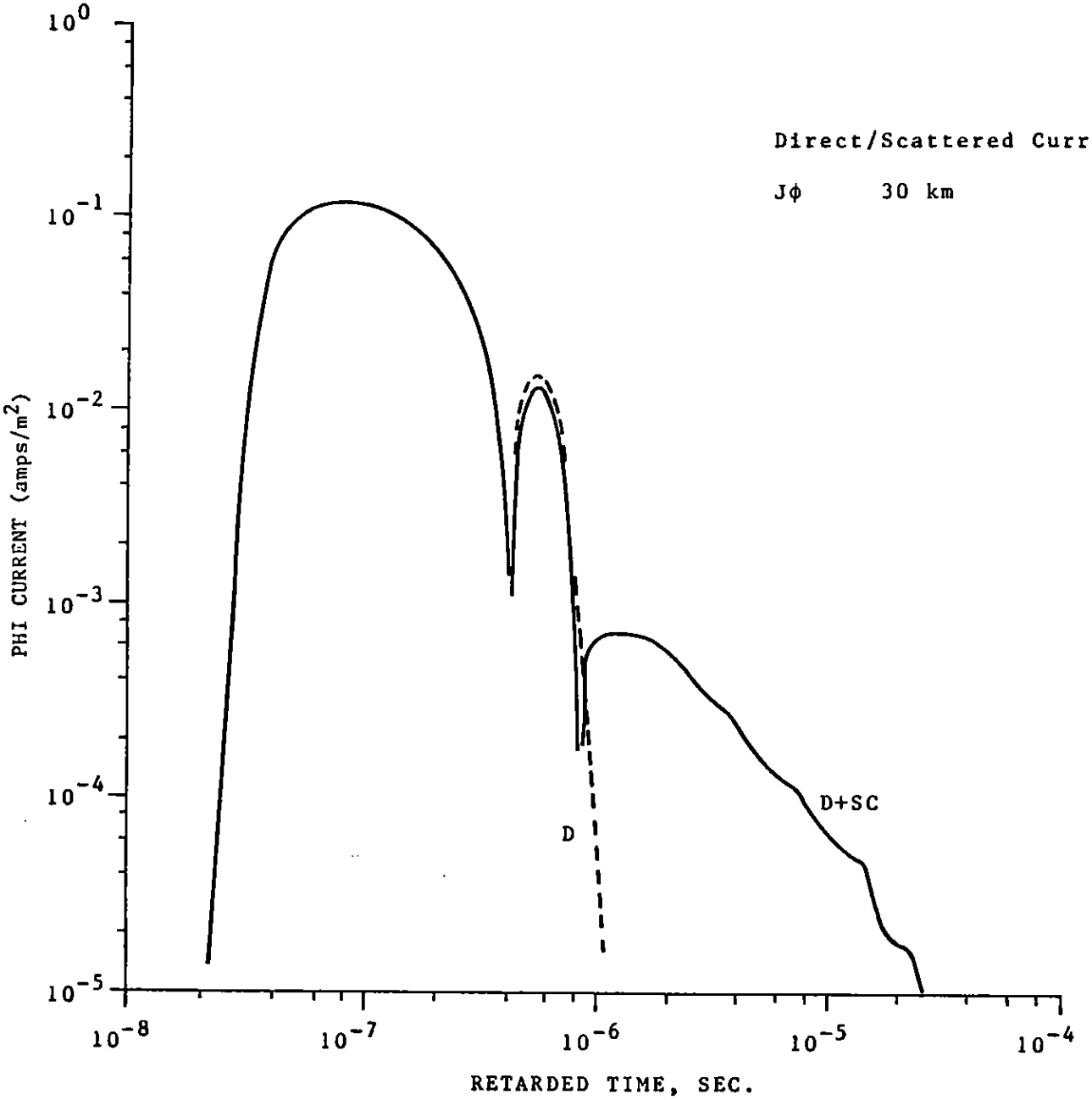

Figure 19. Direct/Scattered Currents, J-Phi.

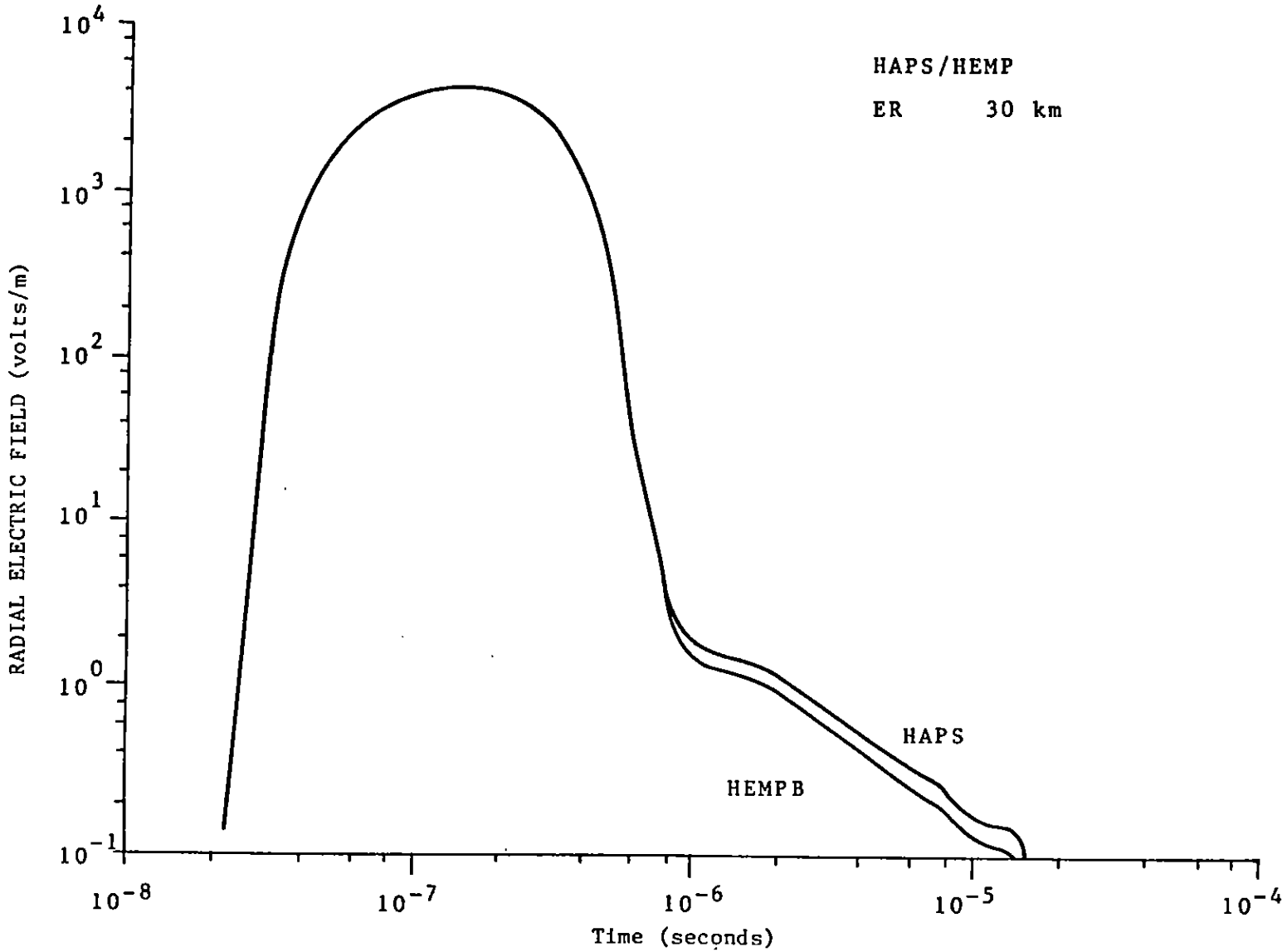

Figure 20. E Radial Comparison of HAPS and HEMPB.

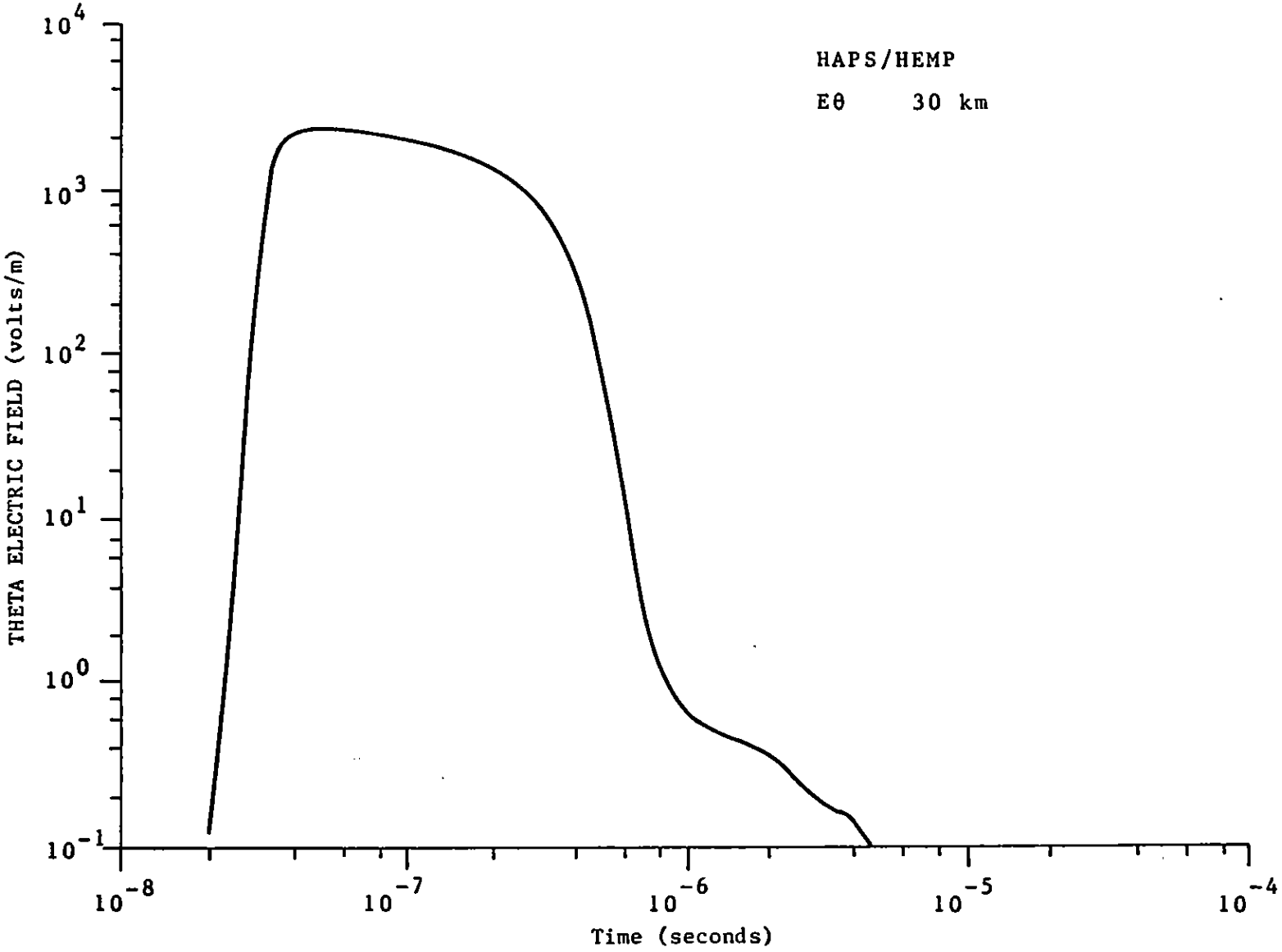

Figure 21. E Theta Comparison of HAPS and HEMPB.

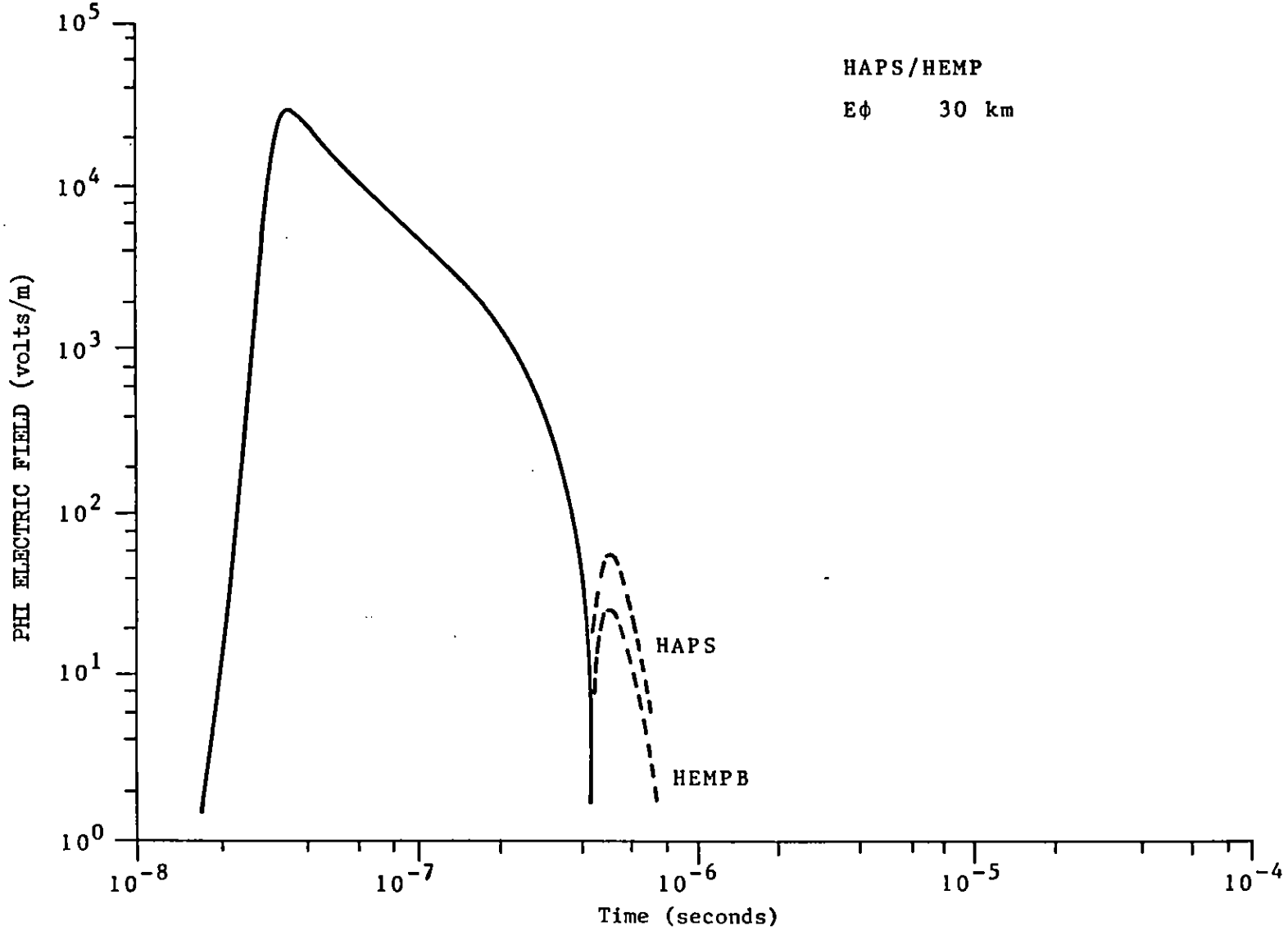

Figure 22. E Phi Comparison of HAPS and HEMPB.

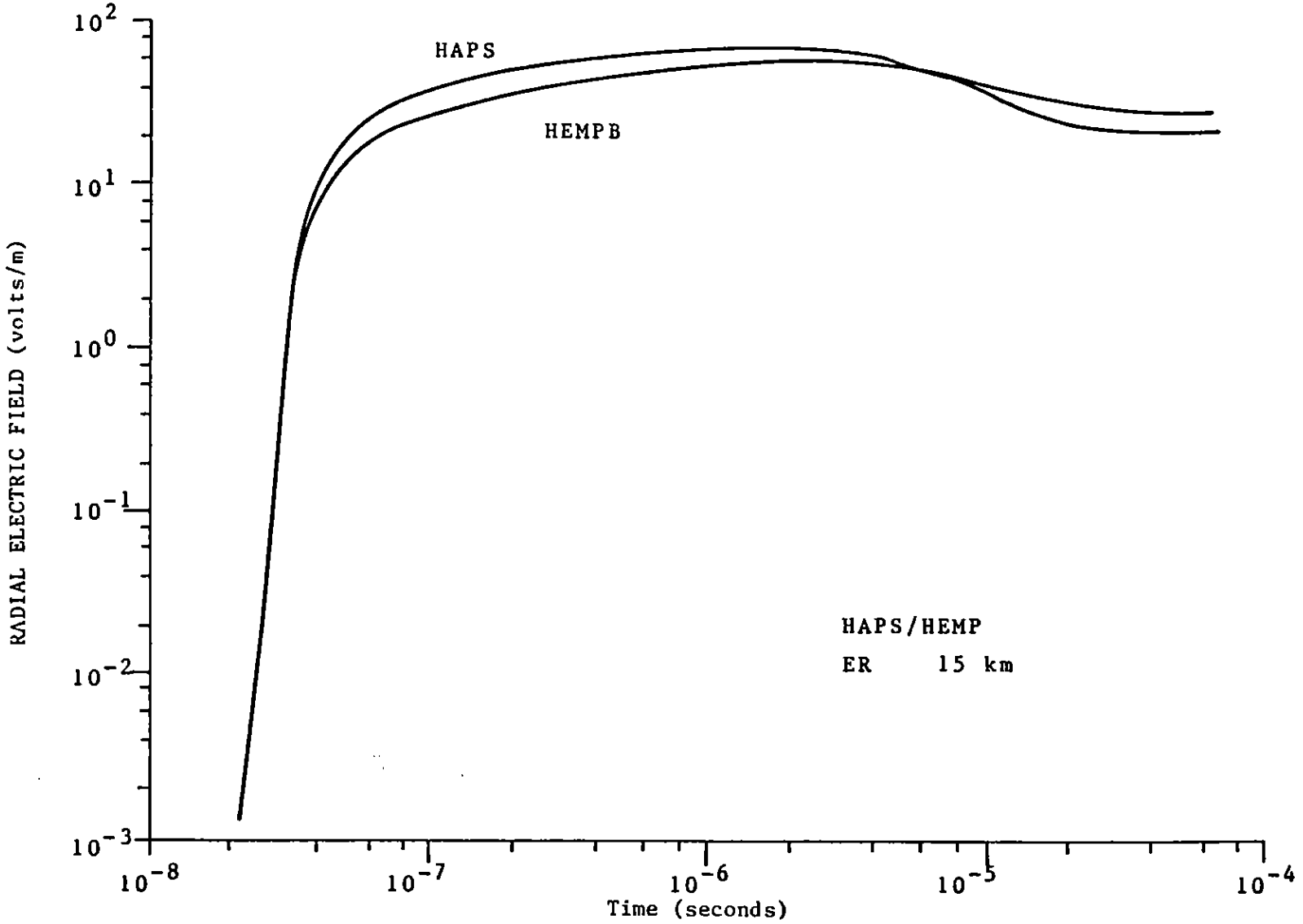

Figure 23. E Radial Comparison of HAPS and HEMPB.

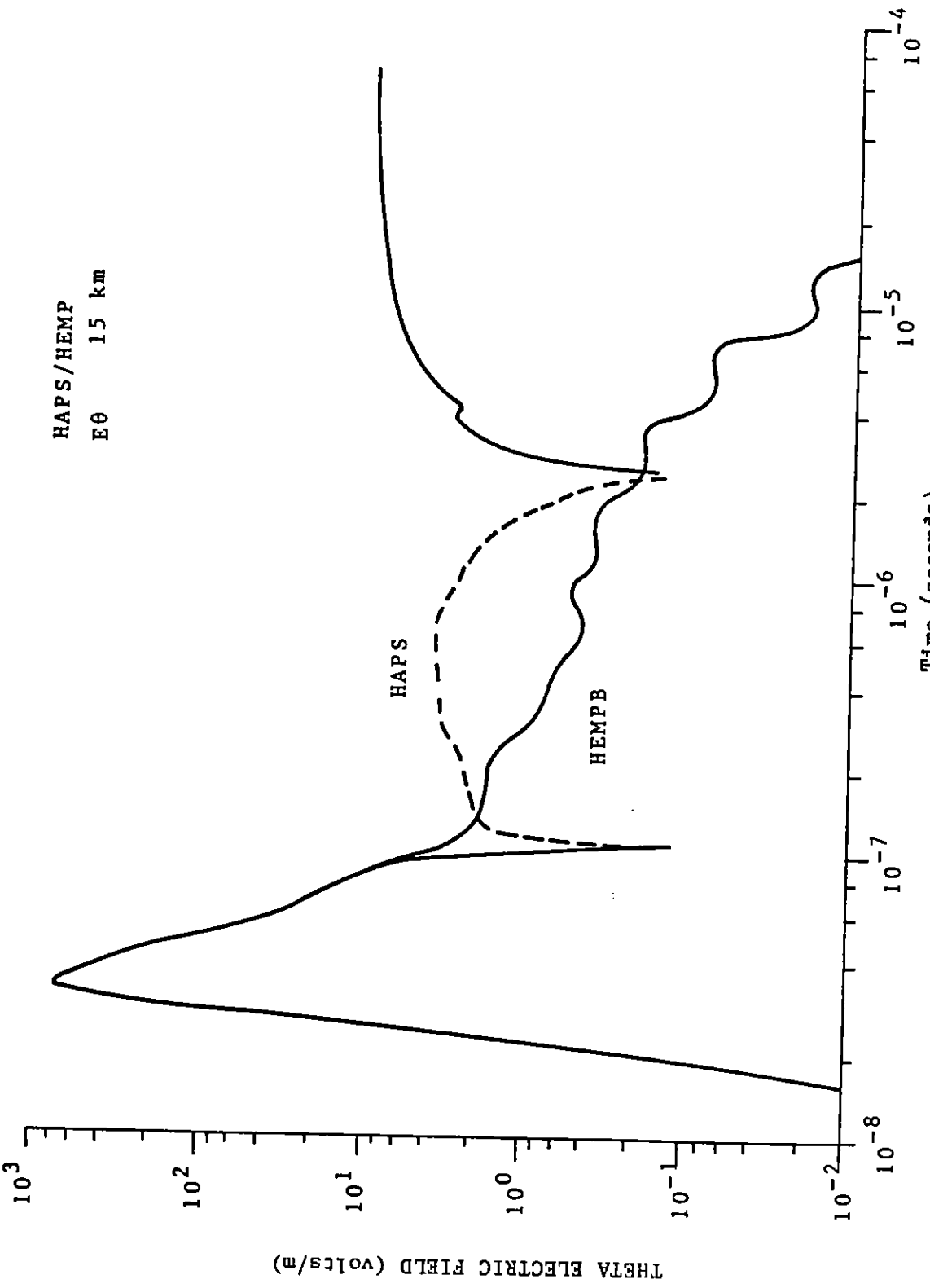

Figure 24. E Theta Comparison of HAPS and HEMPB.

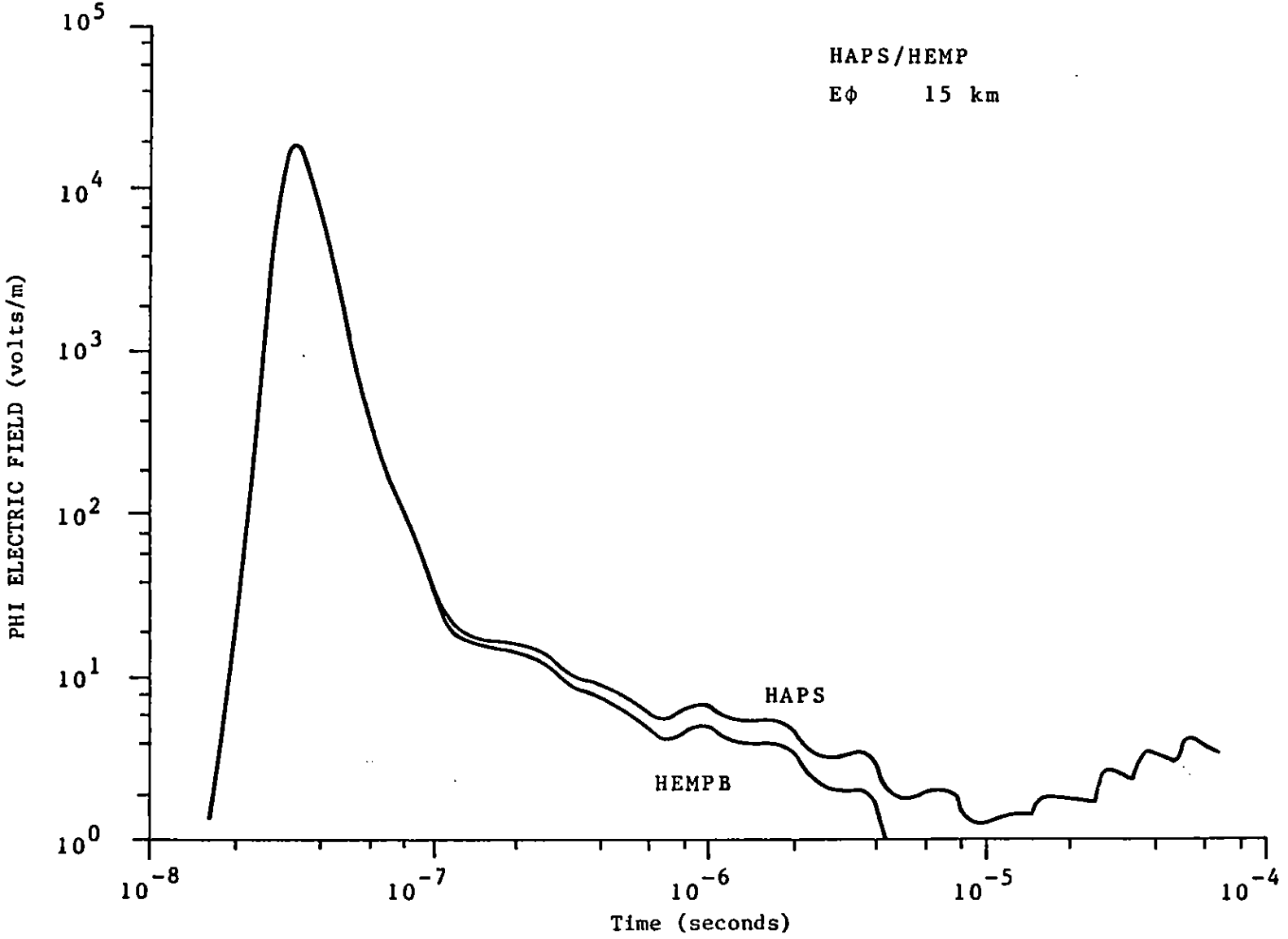

Figure 25. E Phi Comparison of HAPS and HEMPB.

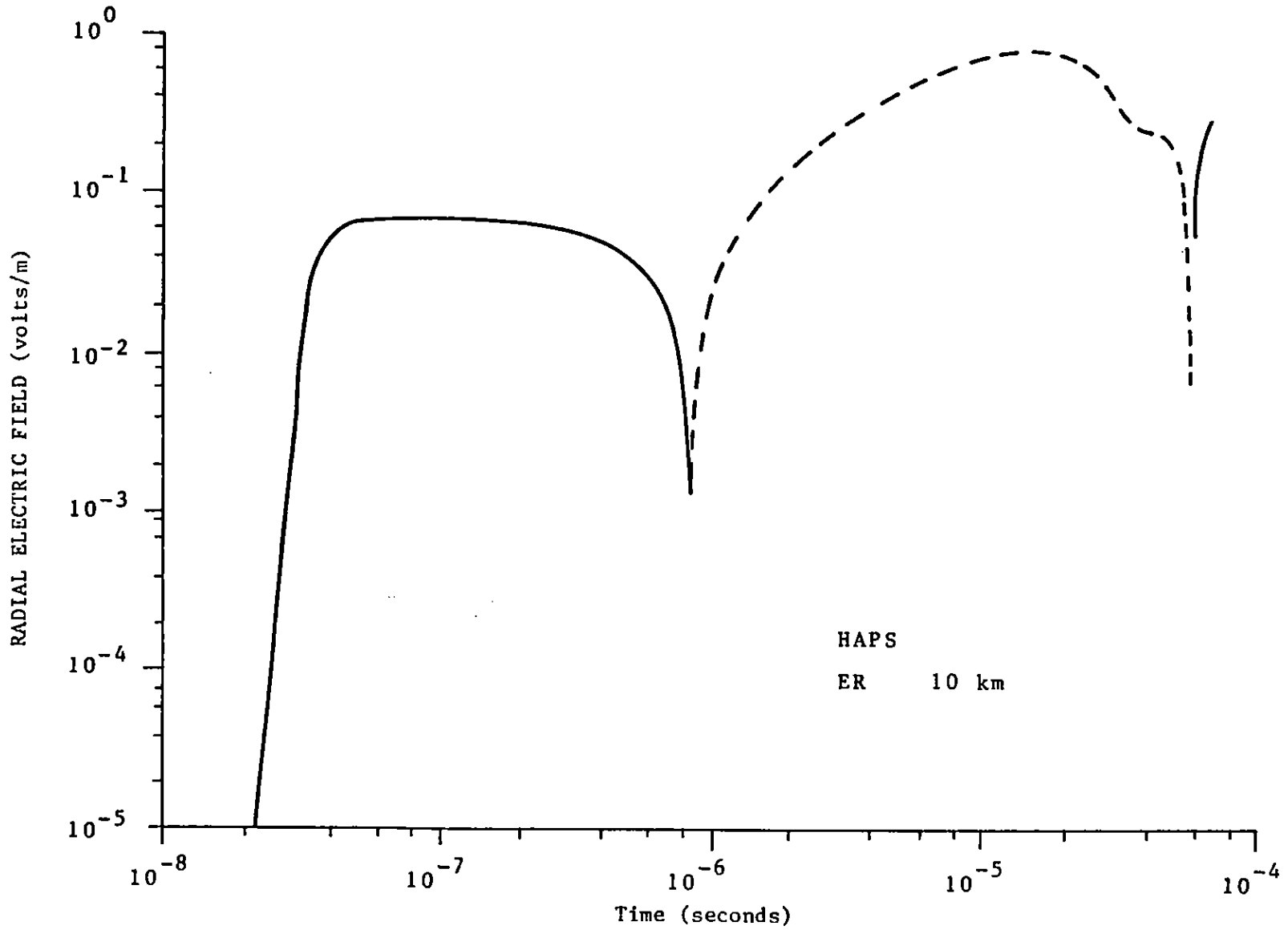

Figure 26. E Radial from HAPS at 10 km.

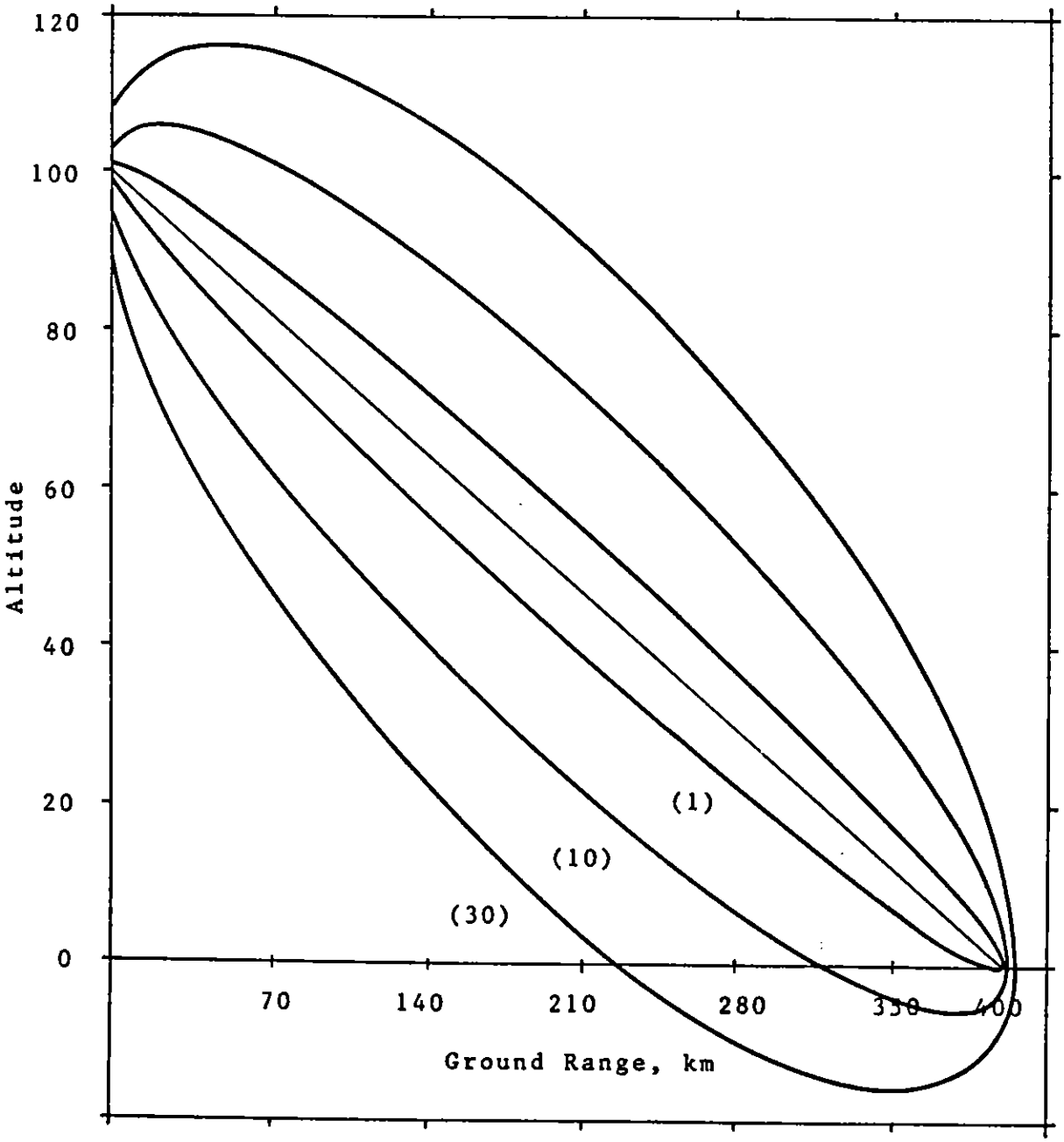

Figure 27. 1, 10, and 30 Microsecond Ellipses About 76° Line of Sight.

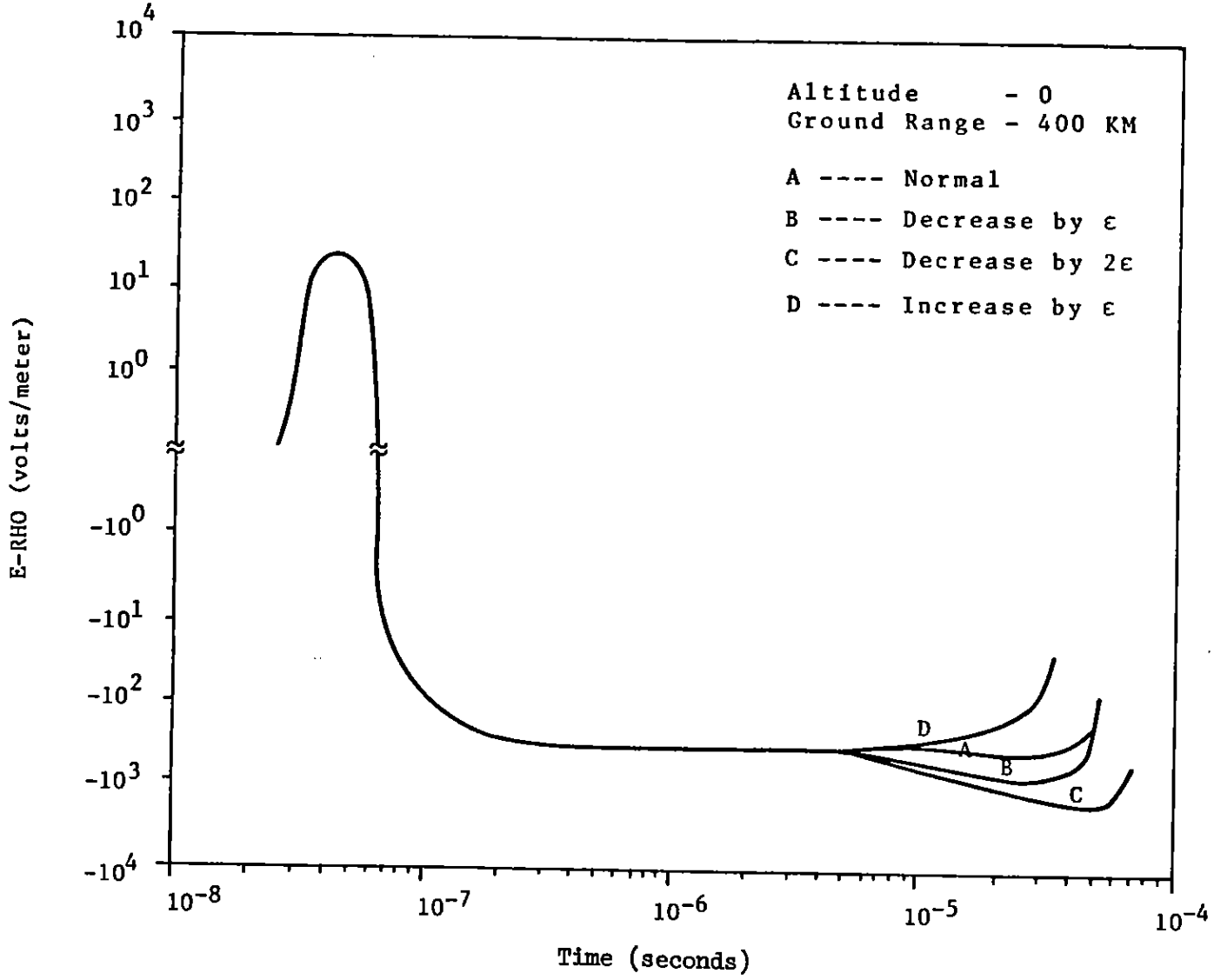

Figure 28. Radial E Fields for Grid Transit Time Study.

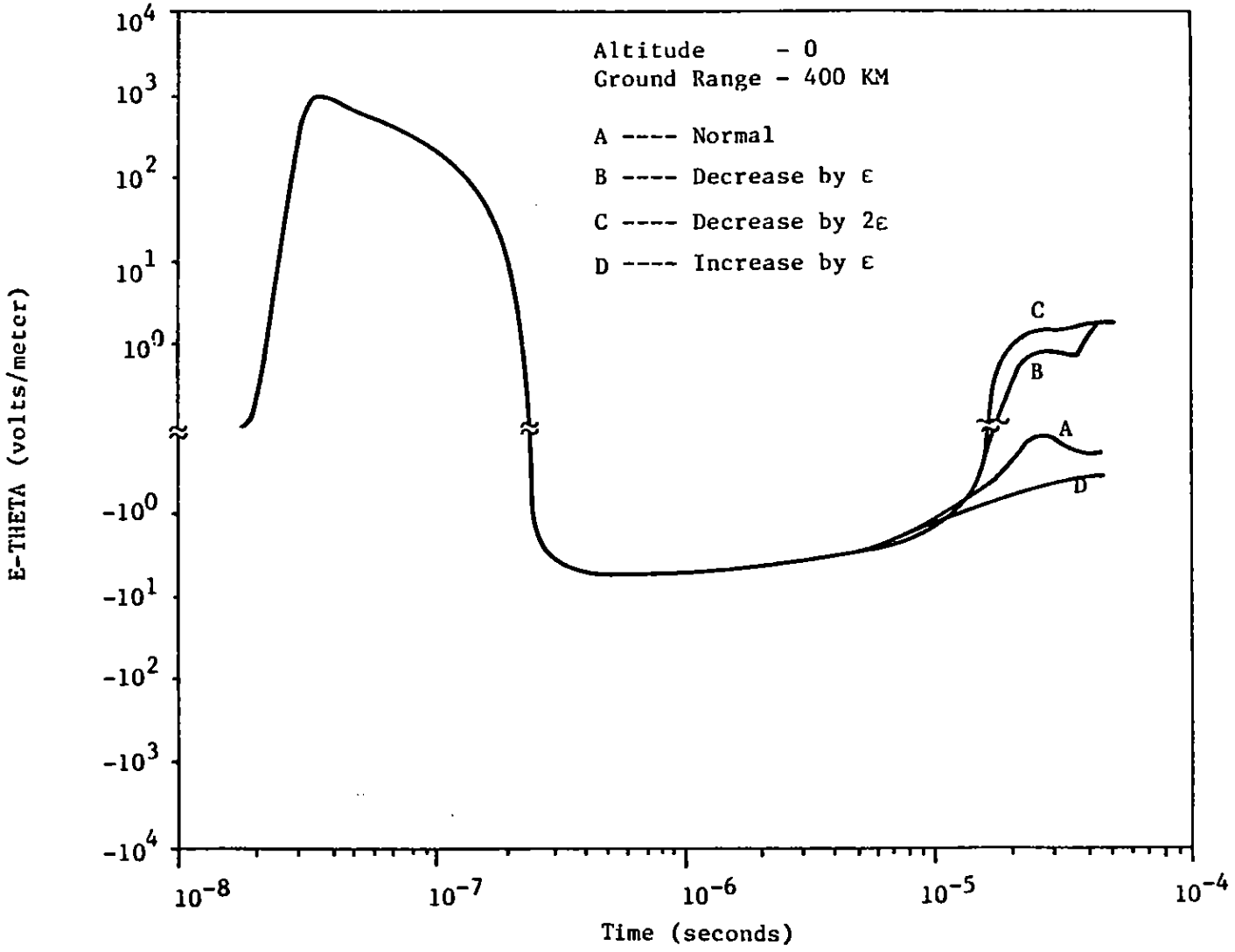

Figure 29. Theta E Fields for Grid Transit Time Study.

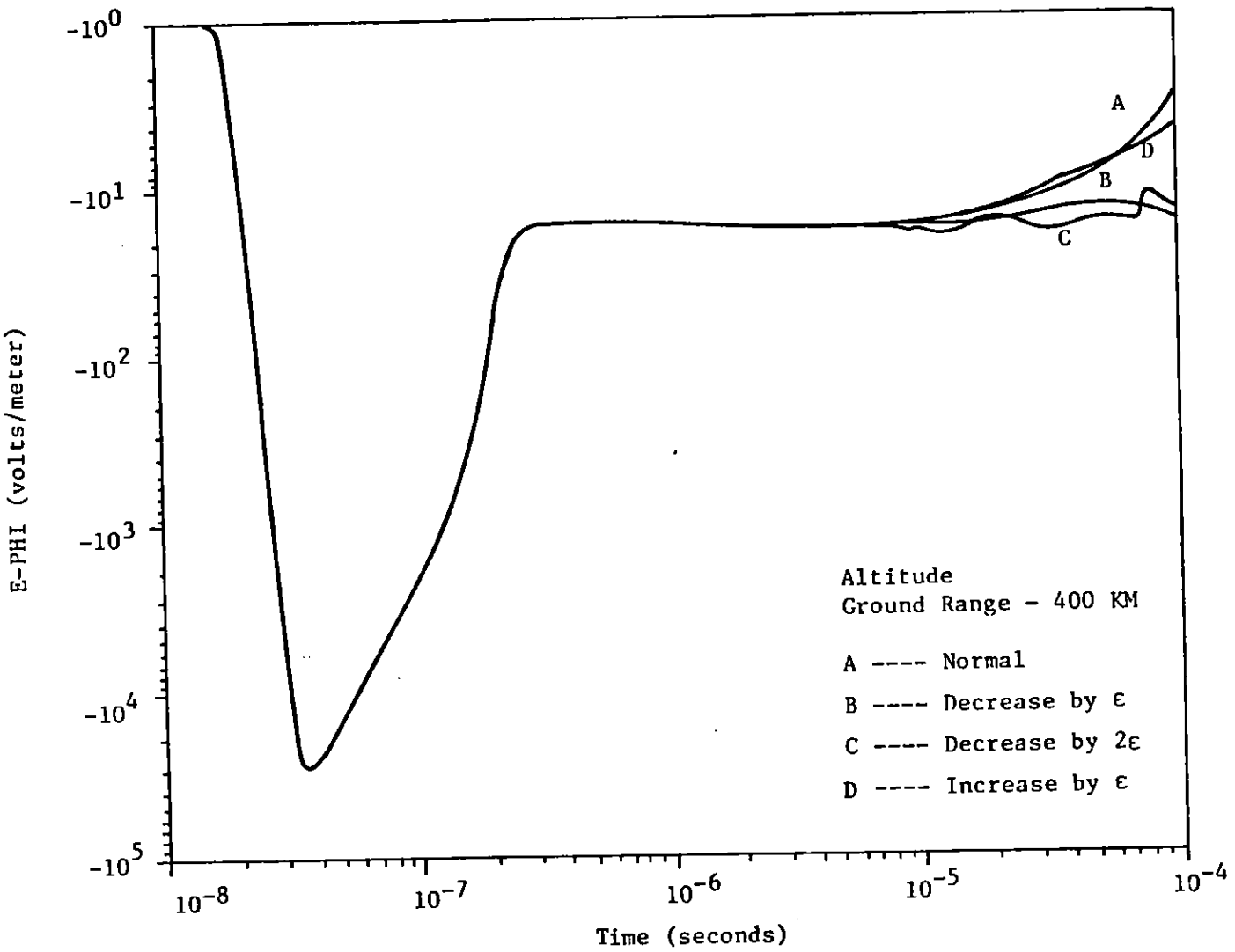

Figure 30. Phi E Field for Grid Transit Time Study.

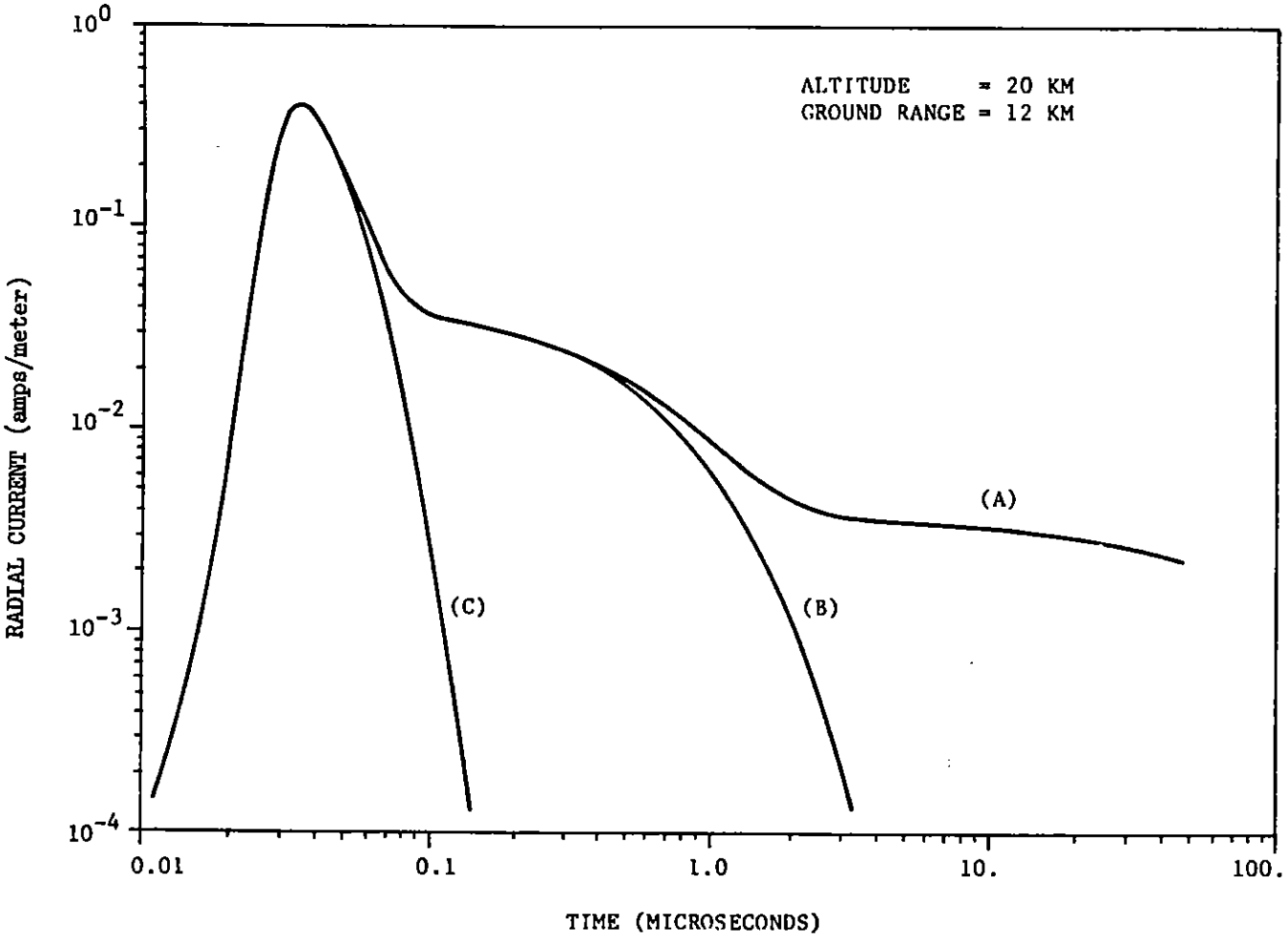

Figure 31. Radial Current for (A) Direct Beam Only, (B) Direct and Scattered and (C) Direct, Scattered and Neutrons.

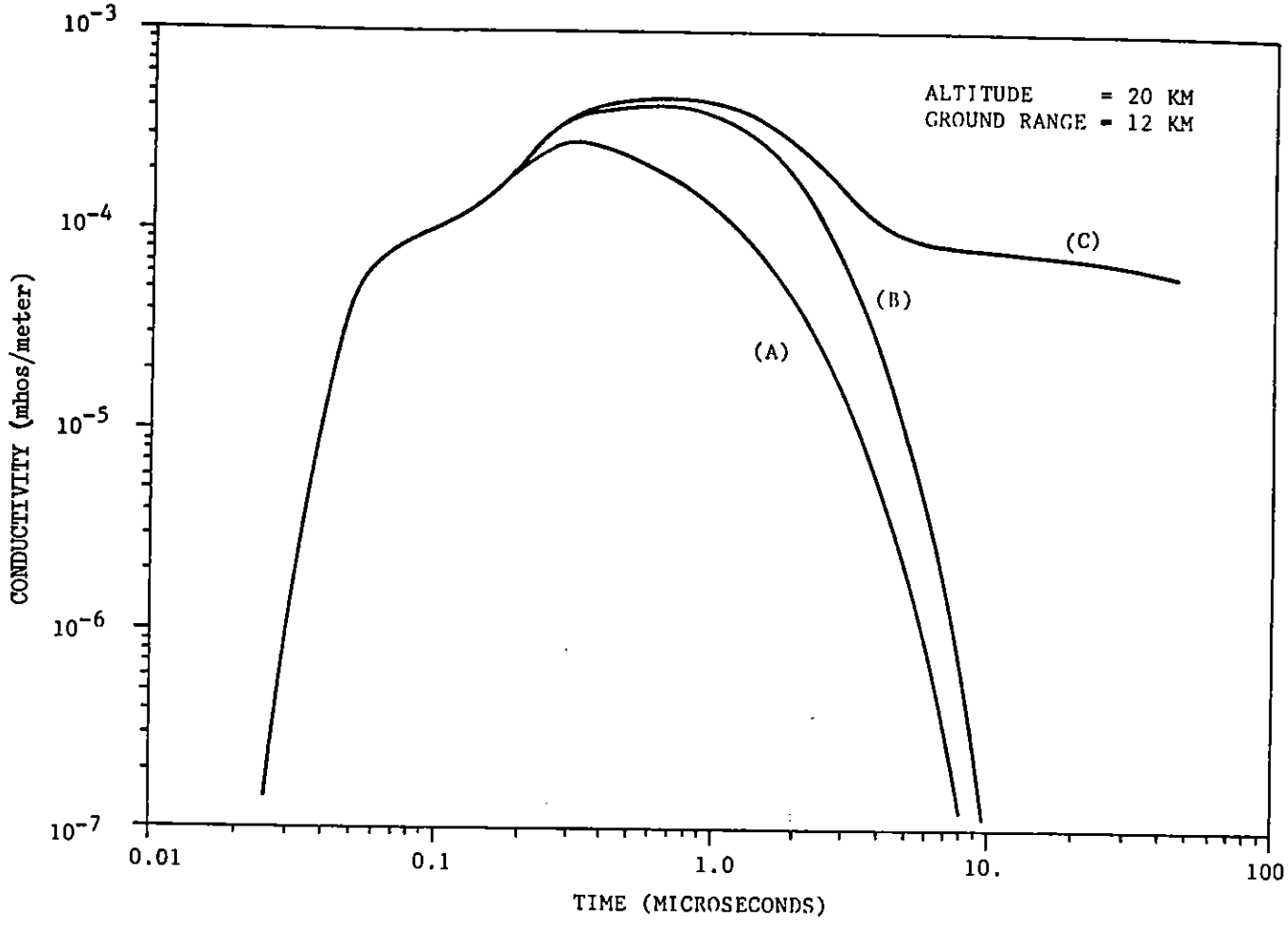

Figure 32. Conductivity for (A) Direct Beam Only, (B) Direct and Scattered and (C) Direct, Scattered and Neutrons.

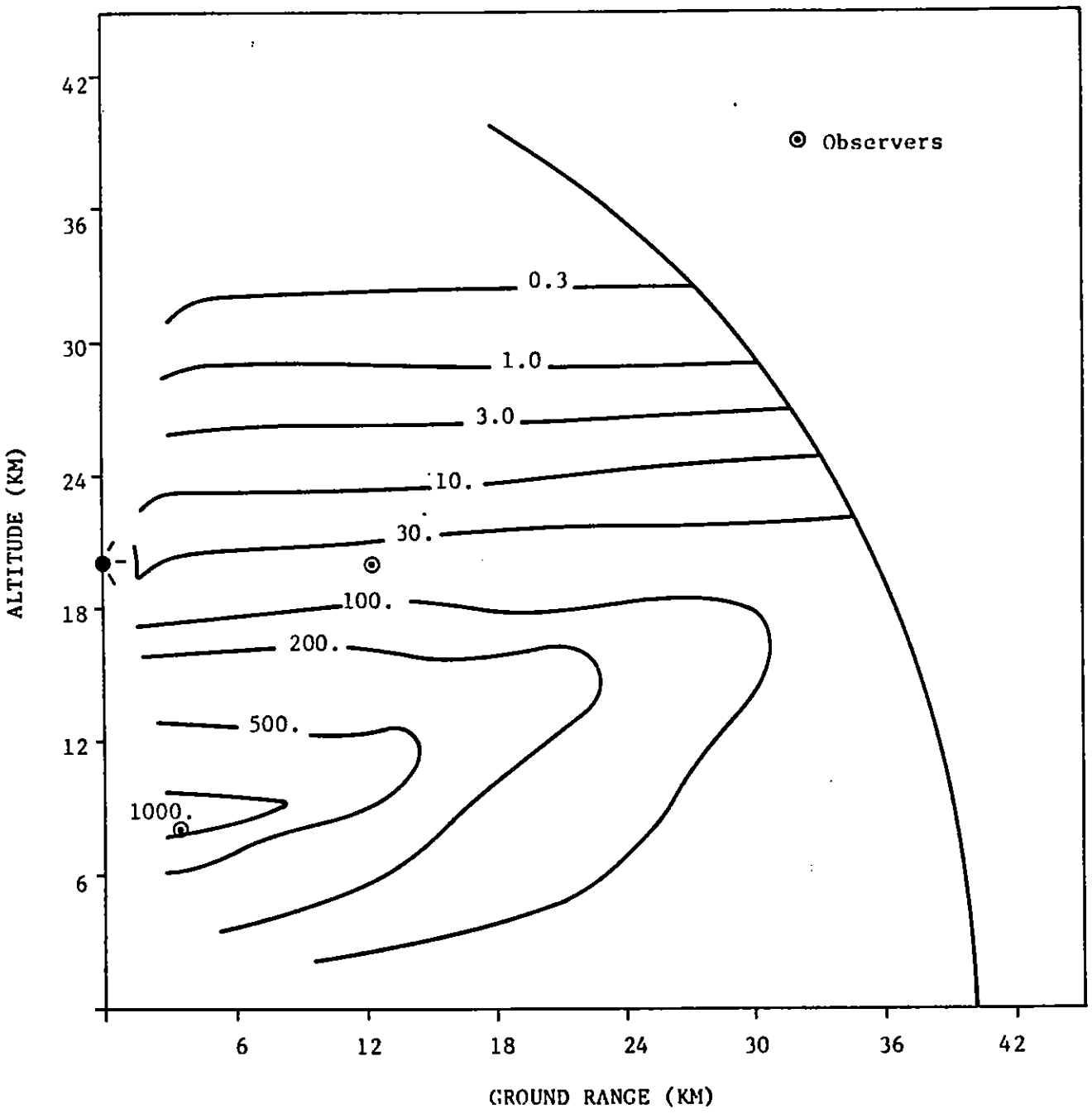

Figure 33. Total E Field (V/M) Contours at 50 Microseconds from Direct and Scattered Gammas and Neutrons.

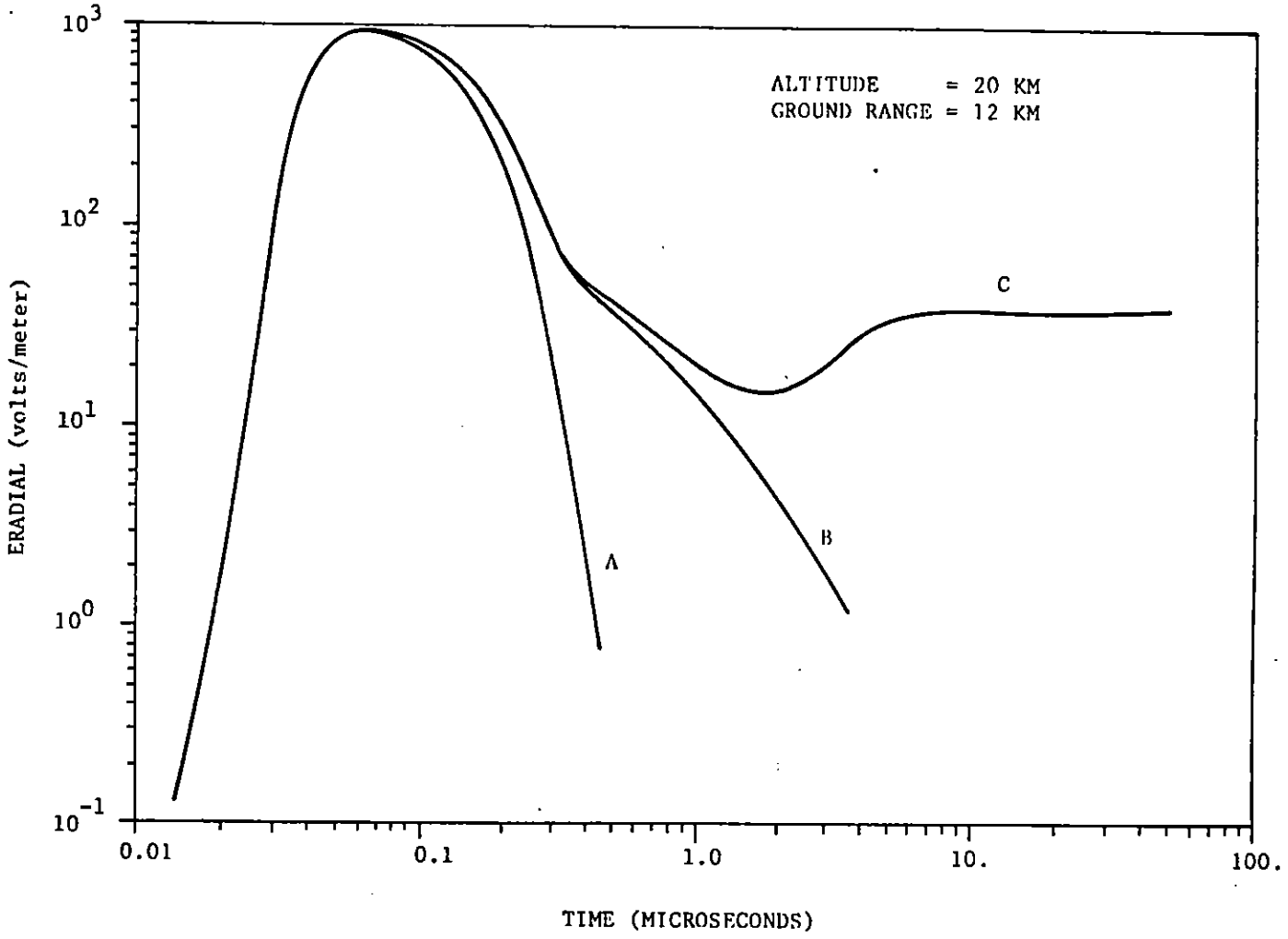

Figure 34. Radial E Field for (A) Direct Beam Only, (B) Direct and Scattered and (C) Direct, Scattered and Neutrons.

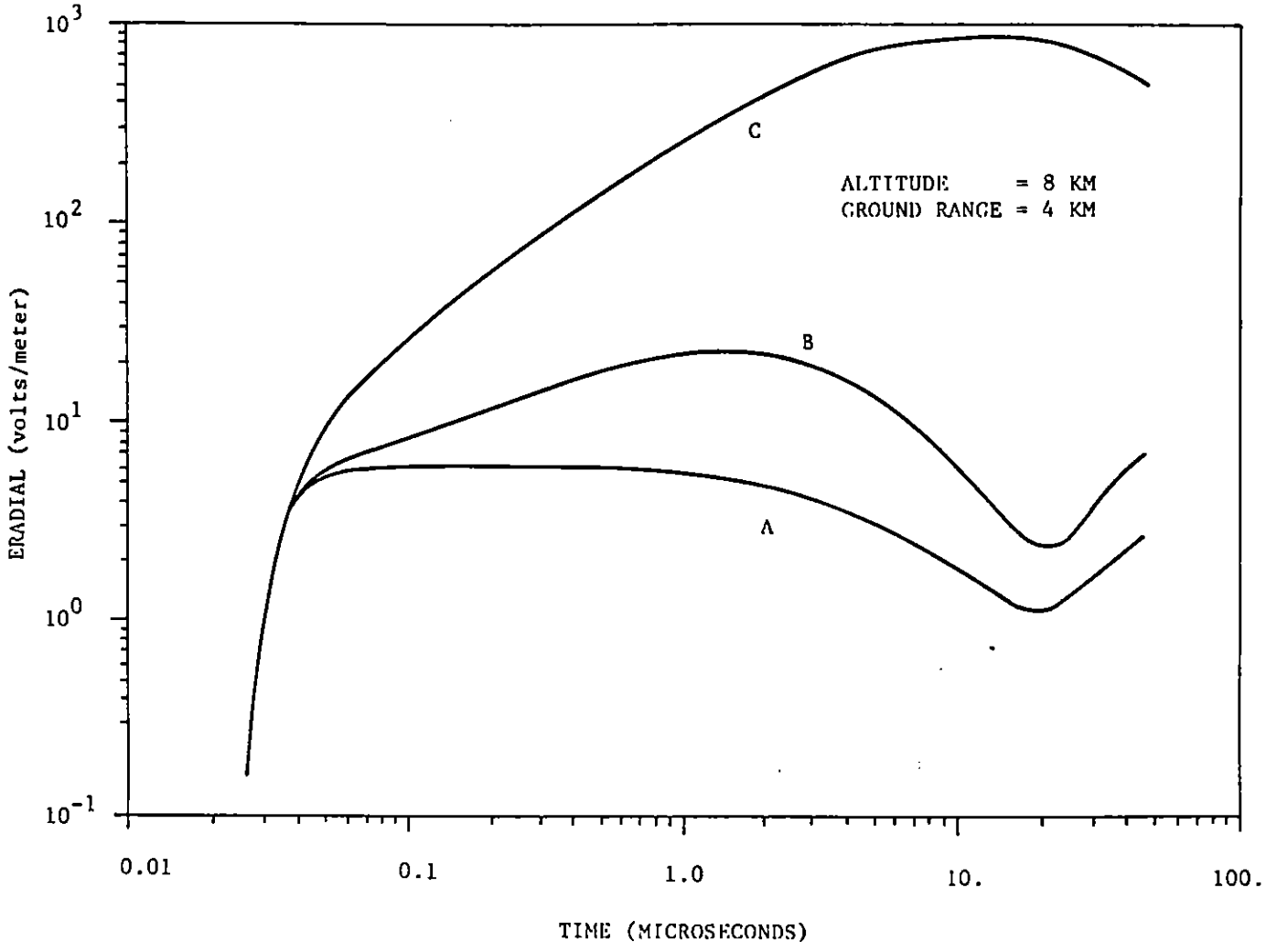

Figure 35. Radial E Field for (A) Direct Beam Only, (B) Direct and Scattered and (C) Direct, Scattered and Neutrons.

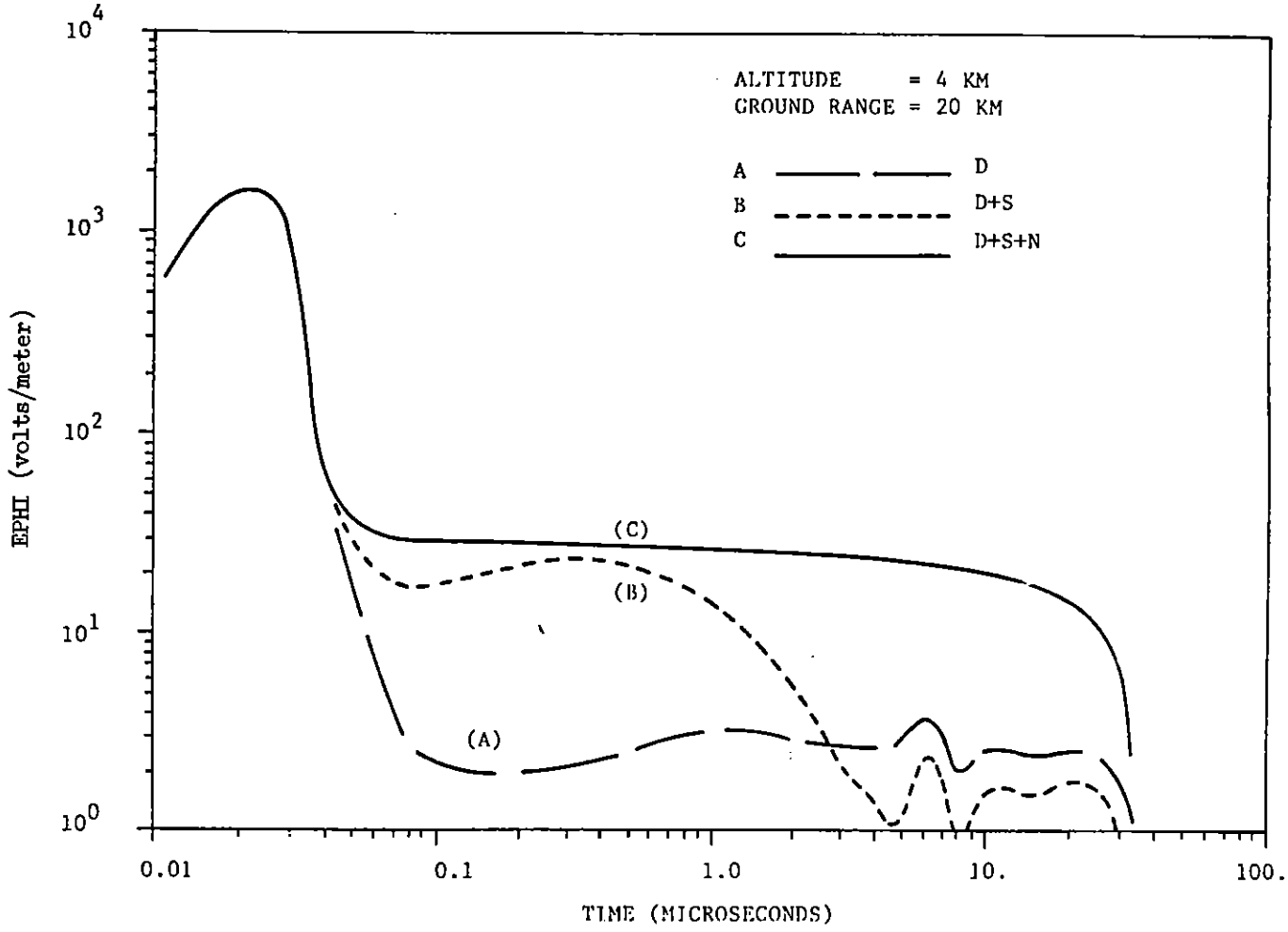

Figure 36. Phi E Field for Direct Beam Only, Direct and Scattered and Direct, Scattered and Neutrons.

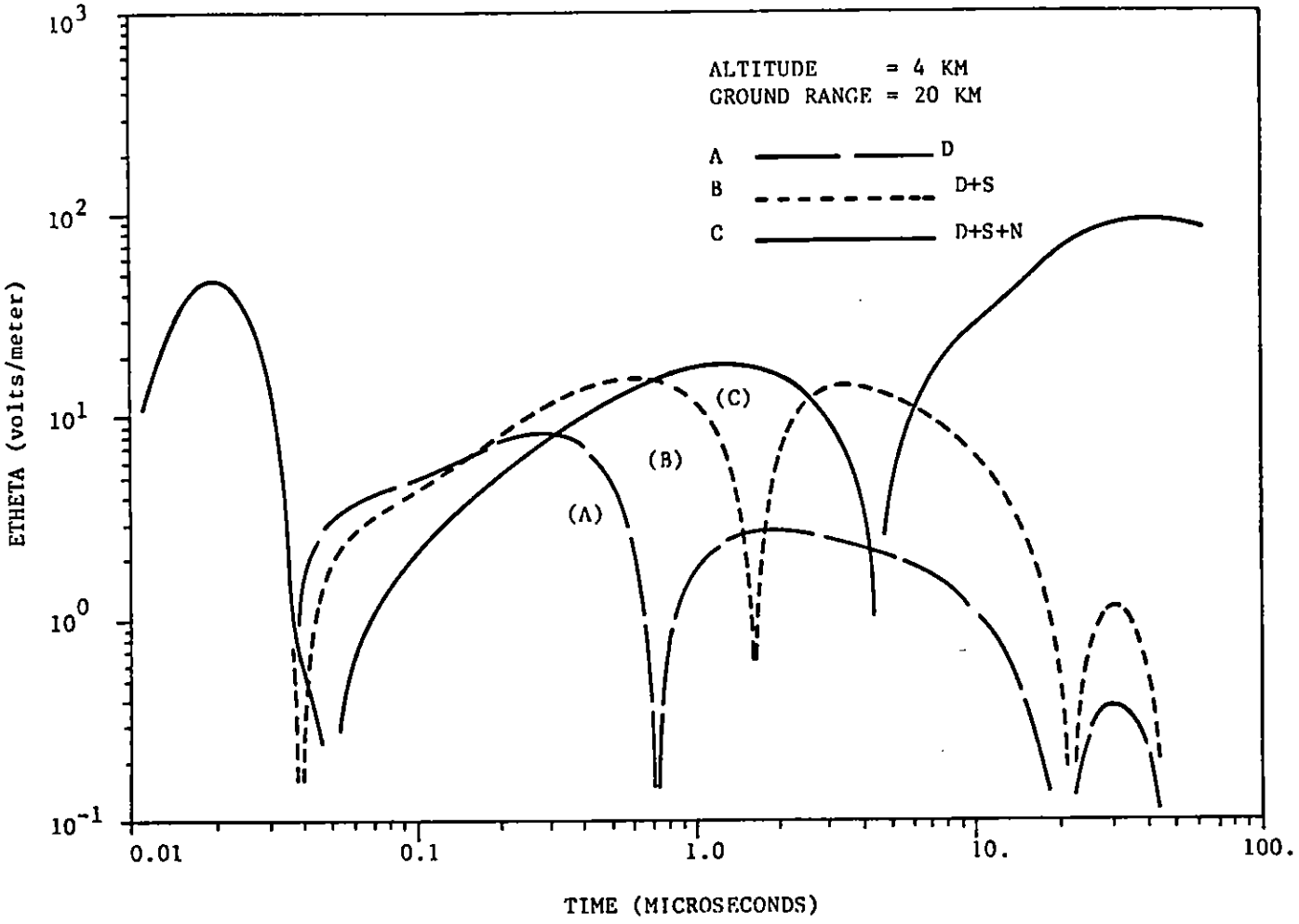

Figure 37. Theta E Field for (A) Direct Beam Only, (B) Direct and Scattered, and (C) Direct, Scattered and Neutrons.

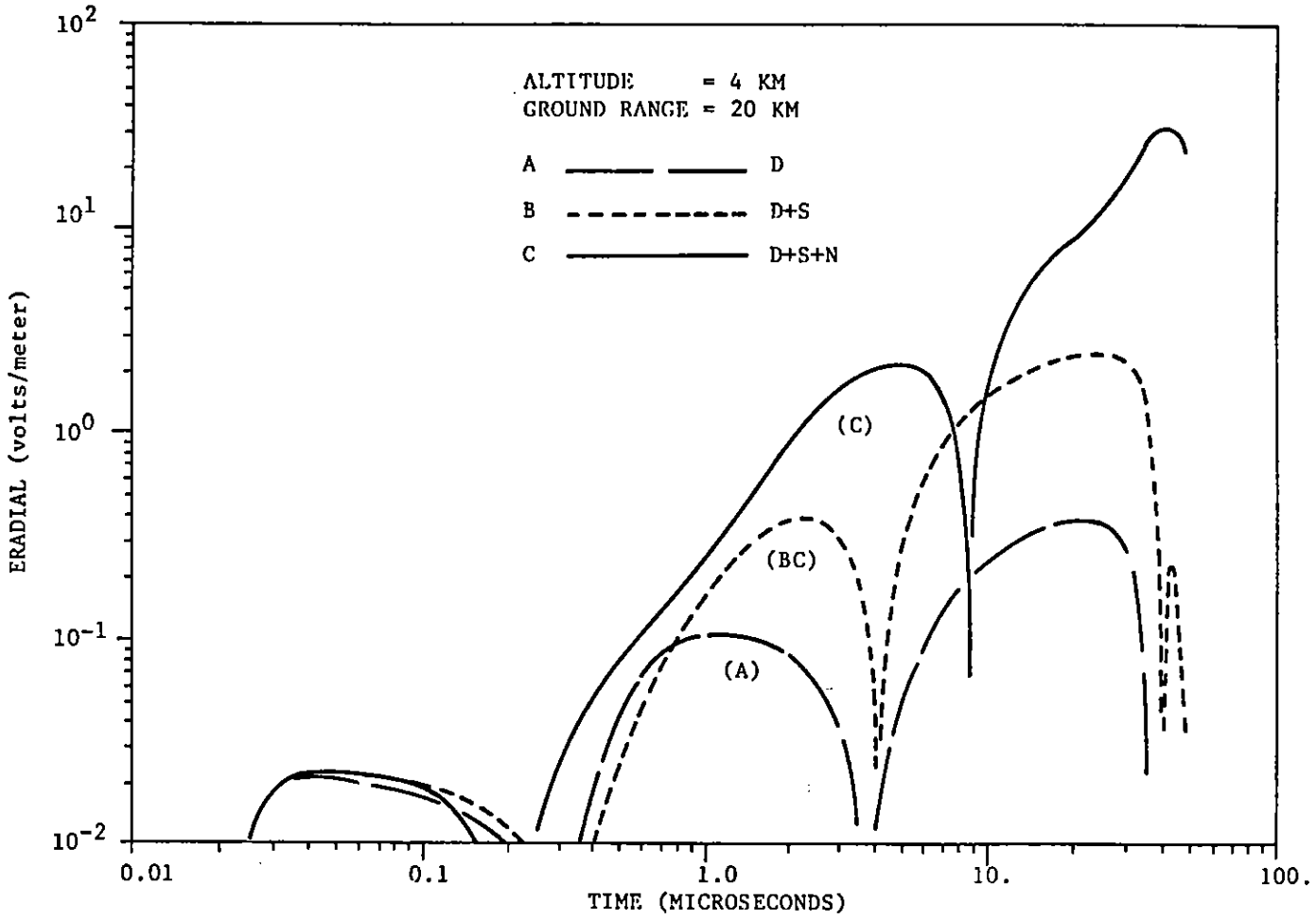

Figure 38. Radial E Field for Direct Beam Only, Direct and Scattered and Direct, Scattered and Neutrons.

SECTION III
PLANE CODE DEVELOPMENT

In recent years considerable effort has been expended at AFWL in the development of a two-dimensional high-altitude EMP computer code. As has been noted by C. L. Longmire (Ref. 2), under certain assumptions there is a class of high-altitude problems which are one-dimensional. A computer code, P, has been developed which implements the necessary assumptions.

1. FIELD EQUATIONS

There are two assumptions needed to cast the problem into a one-dimensional problem. First, the earth and the atmosphere are flat. That is, the only variation in the atmosphere is along a direction normal to surface of the flat earth. The other necessary assumption is that the gamma wavefront impinging upon the atmosphere is planar.

The geometry of the problem under consideration is shown in Fig. 39. The $\hat{y}$ vector is into the page.

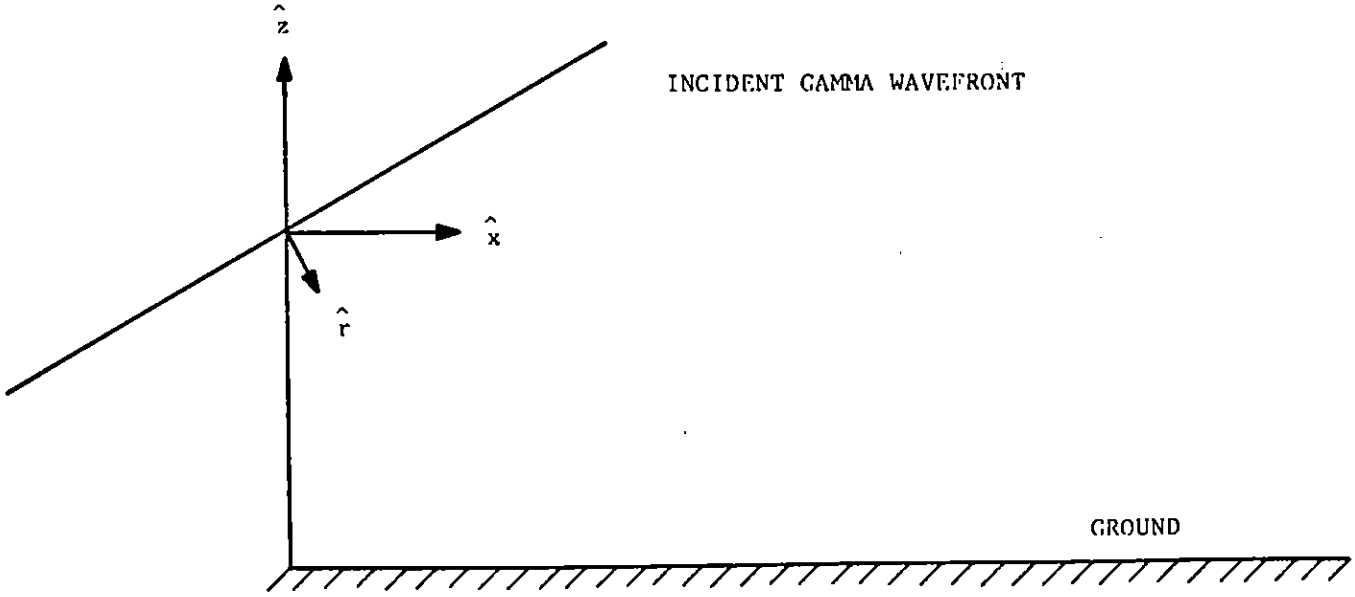

Figure 39. Problem Geometry.

The Maxwell curl equations are

$$\nabla \times \vec{E} = -\mu \frac{\partial \vec{H}}{\partial t} \tag{5}$$

$$\nabla \times \vec{H} = \vec{J} + \sigma \vec{E} + \epsilon \frac{\partial \vec{E}}{\partial t} \tag{6}$$

The transformation to retarded time is

$$\nabla \rightarrow \nabla' - \frac{\hat{r}}{c} \frac{\partial}{\partial \tau} \tag{7}$$

$$\frac{\partial}{\partial t} \rightarrow \frac{\partial}{\partial \tau} \tag{8}$$

Applying these to Eqs. (5) and (6), and dropping the prime, yields

$$\nabla \times \vec{E} - \frac{1}{c} \hat{r} \times \frac{\partial \vec{E}}{\partial \tau} = -\mu \frac{\partial \vec{H}}{\partial \tau} \tag{9}$$

$$\nabla \times \vec{H} - \frac{1}{c} \hat{r} \times \frac{\partial \vec{H}}{\partial \tau} = J + \sigma \vec{E} + \epsilon \frac{\partial \vec{E}}{\partial \tau} \tag{10}$$

From Fig. 39 it is obvious that the unit vector $\hat{r}$ is given by

$$\hat{r} = \cos\theta\hat{x} - \sin\theta\hat{z} \tag{11}$$

With the assumption that derivatives with respect to x and y are zero, the three component equations of (9) are

$$\frac{\partial E_y}{\partial z} + \frac{1}{c}\left[\sin\theta\,\frac{\partial E_y}{\partial \tau}\right] = \mu\,\frac{\partial H_x}{\partial \tau} \tag{12}$$

$$\frac{\partial E_x}{\partial z} + \frac{1}{c}\left[\sin\theta\,\frac{\partial E_x}{\partial \tau} + \cos\theta\,\frac{\partial E_z}{\partial \tau}\right] = -\mu\,\frac{\partial H_y}{\partial \tau} \tag{13}$$

$$\frac{1}{c}\left[\cos\theta\,\frac{\partial E_y}{\partial \tau}\right] = \mu\,\frac{\partial H_z}{\partial \tau} \tag{14}$$

The three component equations of (10) are

$$-\frac{\partial H_y}{\partial z} - \frac{1}{c}\left[\sin\theta\,\frac{\partial H_y}{\partial \tau}\right] = J_x + \sigma E_x + \epsilon\,\frac{\partial E_x}{\partial \tau} \tag{15}$$

$$\frac{\partial H_x}{\partial z} + \frac{1}{c}\left[\sin\theta\,\frac{\partial H_x}{\partial \tau} + \cos\theta\,\frac{\partial H_z}{\partial \tau}\right] = J_y + \sigma E_y + \epsilon\,\frac{\partial E_y}{\partial \tau} \tag{16}$$

$$-\frac{1}{c}\left[\cos\theta\,\frac{\partial H_y}{\partial \tau}\right] = J_z + \sigma E_z + \epsilon\,\frac{\partial E_z}{\partial \tau} \tag{17}$$

Note that Eqs. (12) through (17) are two sets of three coupled equations. The coupling of the set equations is through the field dependence of the conductivity. The first set, Eqs. (13), (15), and (17), will be referred to as the "TM" set. The remaining equations, (12), (14), and (16), will be referred to as the "TE" set. The two sets of equations will be solved by finite difference methods described in the next section.

2. FINITE DIFFERENCE SOLUTION OF FIELD EQUATIONS

A portion of the finite difference grid is shown in Fig. 40. The j subscript indexes over altitude. The superscript 1 refers to quantities at the previous time step; superscript 2 refers to quantities at the present time step. It is to be noted that all quantities are centered at the (X), which is denoted by subscript j, superscript 1/2.

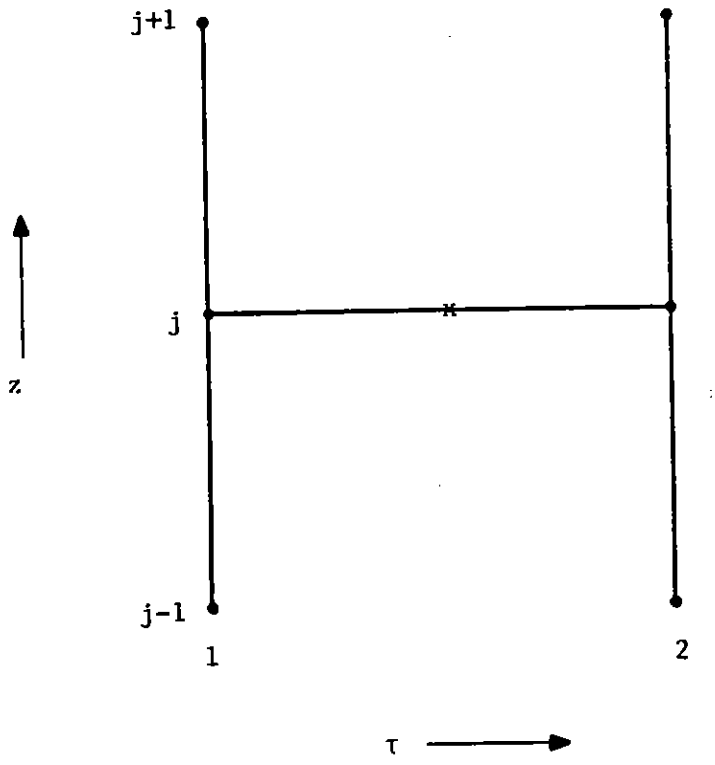

Fig. 40. Finite difference grid.

In this grid the time derivative of a quantity, such as E_x, is approximated by

$$\frac{\partial E_x}{\partial \tau} \approx \frac{E^2_{xj} - E^1_{xj}}{\Delta \tau} \tag{18}$$

The space derivative of E_x is given by

$$\frac{\partial E_x}{\partial z} \approx \frac{E^1_{xj+1} - E^1_{xj} + E^2_{xj} - E^2_{xj-1}}{2\Delta z} \tag{19}$$

The finite difference form of the TE equations will be given first. Eq. (12) in finite difference form is

$$\frac{1}{2\Delta z}\left[E^1_{yj+1} - E^1_{yj} + E^2_{yj} - E^2_{yj-1}\right] + \frac{\sin\theta}{c\Delta\tau}\left[E^2_{yj} - E^1_{yj}\right] = \frac{\mu}{\Delta\tau}\left[H^2_{xj} - H^1_{xj}\right] \tag{20}$$

Eq. (14) becomes

$$\frac{\cos\theta}{c\Delta\tau}\left[E^2_{yj} - E^1_{yj}\right] = \frac{\mu}{\Delta\tau}\left[H^2_{zj} - H^1_{zj}\right] \tag{21}$$

The finite difference form of (16) is

$$\frac{1}{2\Delta z}\left[H^1_{xj+1} - H^1_{xj} + H^2_{xj} - H^2_{xj-1}\right] + \frac{\sin\theta}{c\Delta\tau}\left[H^2_{xj} - H^1_{xj}\right] + \frac{\cos\theta}{c\Delta\tau}\left[H^2_{zj} - H^1_{zj}\right]$$

$$= J^{1/2}_y + \frac{\sigma^{1/2}_j}{2}\left[E^2_{yj} + E^1_{yj}\right] + \frac{\epsilon}{\Delta\tau}\left[E^2_{yj} - E^1_{yj}\right] \qquad (22)$$

Eq. (20) can be rewritten as

$$A_1 E^2_{yj} + A_2 H^2_{xj} = B_1 \qquad (23)$$

with

$$A_1 = \frac{1}{2\Delta z} + \frac{\sin\theta}{c\Delta\tau}$$

$$A_2 = -\frac{\mu}{\Delta\tau}$$

$$B_1 = \frac{E^2_{yj-1} - E^1_{yj+1}}{2\Delta z} + E^1_{yj} A_1 - \frac{\mu H^1_{xj}}{\Delta\tau}$$

Eq. (21) can be written in a similar form

$$A_3 E^2_{yj} + A_4 H^2_{zj} = B_2 \tag{24}$$

with

$$A_3 = \frac{\cos\theta}{c\Delta\tau}$$

$$A_4 = -\frac{\mu}{\Delta\tau} = A_2$$

$$B_2 = \frac{\cos\theta}{c\Delta\tau} E^1_{yj} - \frac{\mu}{\Delta\tau} H^1_{zj}$$

Likewise for Eq. (22),

$$A_5 E^2_{yj} + A_6 H^2_{xj} + A_7 H^2_{zj} = B_3 \tag{25}$$

where

$$A_5 = -\frac{\epsilon}{\Delta\tau} - \frac{\sigma^{1/2}}{2}$$

$$A_6 = \frac{1}{2\Delta z} + \frac{\sin\theta}{c\Delta\tau} = A_1$$

$$A_7 = \frac{\cos\theta}{c\Delta\tau} = A_3$$

$$B_3 = J_{yj}^{1/2} + E_{yj}^{1}\left[\frac{\sigma_j^{1/2}}{2} - \frac{\epsilon}{\Delta\tau}\right] + H_{zj}^{1}\left[\frac{\cos\theta}{c\Delta\tau}\right] + H_{xj}^{1}\left[\frac{\sin\theta}{c\Delta\tau} + \frac{1}{2\Delta z}\right]$$

$$+ \frac{H_{xj-1}^{2} - H_{xj+1}^{1}}{2\Delta z}$$

At each grid point we have the following system of linear equations to solve for TE set of equations:

$$\begin{bmatrix} A_1 & A_2 & O \\ A_3 & O & A_2 \\ A_5 & A_1 & A_3 \end{bmatrix} \begin{bmatrix} E_{yj}^{2} \\ H_{xj}^{2} \\ H_{zj}^{2} \end{bmatrix} = \begin{bmatrix} B_1 \\ B_2 \\ B_3 \end{bmatrix} \qquad (26)$$

After a little algebra the TE field components are given by

$$E_{yj}^{2} = \frac{\frac{A_3}{A_1}\left(\frac{B_3}{A_3} - \frac{B_2}{A_2}\right) - \frac{B_1}{A_2}}{\frac{A_3}{A_1}\left(\frac{A_5}{A_3} - \frac{A_3}{A_2}\right) - \frac{A_1}{A_2}} \qquad (27)$$

$$H^2_{xj} = \frac{B_1}{A_2} - \frac{A_1}{A_2} E^2_{yj} \tag{28}$$

$$H^2_{zj} = \frac{B_2}{A_2} - \frac{A_3}{A_2} E^2_{yj} \tag{29}$$

9

Returning to the TM set of equations, the finite difference form of (13) is

$$\frac{1}{2\Delta z}\left[E^1_{xj+1} - E^1_{xj} + E^2_{xj} - E^2_{xj-1}\right] + \frac{\sin\theta}{c\Delta\tau}\left[E^2_{xj} - E^1_{xj}\right] + \frac{\cos\theta}{c\Delta\tau}\left[E^2_{zj} - E^1_{zj}\right]$$

$$= -\frac{\mu}{\Delta\tau}\left[H^2_{yj} - H^1_{yj}\right] \tag{30}$$

The finite difference form of (15) is

$$-\frac{1}{2\Delta z}\left[H^1_{yj+1} - H^1_{yj} + H^2_{yj} - H^2_{yj-1}\right] - \frac{\sin\theta}{c\Delta\tau}\left[H^2_{yj} - H^1_{yj}\right]$$

$$= J^{1/2}_x + \frac{\sigma^{1/2}_j}{2}\left[E^2_{xj} + E^1_{xj}\right] + \frac{\epsilon}{\Delta\tau}\left[E^2_{xj} - E^1_{xj}\right] \tag{31}$$

The finite form of Eq. (17) is

$$- \frac{\cos\theta}{c\Delta\tau}\left[H^2_{yj} - H^1_{yj}\right] = J^{1/2}_z + \frac{\sigma^{1/2}_j}{2}\left[E^2_{zj} + E^1_{zj}\right] + \frac{\epsilon}{\Delta\tau}\left[E^2_{zj} - E^1_{zj}\right] \qquad (32)$$

Rewrite (30) as

$$A_8 E^2_{xj} + A_9 E^2_{zj} + A_{10} H^2_{yj} = B_4 \qquad (33)$$

where

$$A_8 = \frac{1}{2\Delta z} + \frac{\sin\theta}{c\Delta\tau} = A_1$$

$$A_9 = \frac{\cos\theta}{c\Delta\tau} = A_3$$

$$A_{10} = \frac{\mu}{\Delta\tau} = -A_2$$

$$B_4 = \frac{1}{2\Delta z}\left[E^2_{xj-1} - E^1_{xj+1}\right] + \left[\frac{\sin\theta}{c\Delta\tau} + \frac{1}{2\Delta z}\right] E^1_{xj} + \frac{\cos\theta}{c\Delta\tau}\, E^1_{zj} + \frac{\mu}{\Delta\tau}\, H^1_{yj}$$

Rewrite (31) as

$$A_{11} E^2_{xj} + A_{12} H^2_{yj} = B5 \qquad (34)$$

where

$$A_{11} = -\frac{\epsilon}{\Delta\tau} - \frac{\sigma_j^{1/2}}{2} = A_5$$

$$A_{12} = -\frac{1}{2\Delta z} - \frac{\sin\theta}{c\Delta\tau} = -A_1$$

$$B_5 = J_x^{1/2} + \frac{\sigma_j^{1/2}}{2} - \frac{\epsilon}{\Delta\tau} E_{xj} + \frac{1}{2\Delta z}\left[H_{yj+1}^1 - H_{yj-1}^2\right] + \left[\frac{1}{2\Delta z} - \frac{\sin\theta}{c\Delta\tau}\right] H_{yj}^1$$

Finally, rewrite (32) as

$$A_{13}E_{zj}^2 + A_{14}H_{yj}^2 = B_6 \tag{35}$$

where

$$A_{13} = -\frac{\epsilon}{\Delta\tau} - \frac{\sigma_j^{1/2}}{2} = A_5$$

$$A_{14} = -\frac{\cos\theta}{c\Delta\tau} = -A_3$$

$$B_6 = J_z^{1/2} + \left[\frac{\sigma_j^{1/2}}{2} - \frac{\epsilon}{\Delta\tau}\right] E_{zj}^1 - \frac{\cos\theta}{c\Delta\tau} H_{yj}^1$$

For the TM set of equations we have the following system of linear equations:

$$\begin{bmatrix} A_1 & A_3 & -A_2 \\ A_5 & O & -A_1 \\ O & A_5 & -A_3 \end{bmatrix} \begin{bmatrix} E^2_{xj} \\ E^2_{zj} \\ H^2_{yj} \end{bmatrix} = \begin{bmatrix} B_4 \\ B_5 \\ B_6 \end{bmatrix} \tag{36}$$

Again, after more algebra the TM field components are given by

$$H^2_{yj} = \frac{\left(\frac{B_4}{A_3} - \frac{B_6}{A_5}\right)\frac{A_3}{A_1} - \frac{B_5}{A_5}}{\left(\frac{A_3}{A_5} - \frac{A_2}{A_3}\right)\frac{A_3}{A_1} + \frac{A_1}{A_5}} \tag{37}$$

$$E^2_{xj} = \frac{B_5}{A_5} + \frac{A_1}{A_5} H^2_{yj} \tag{38}$$

$$E^2_{zj} = \frac{B_6}{A_5} + \frac{A_3}{A_5} H^2_{yj} \tag{39}$$

Examination of Eqs. (20) and (30) indicate that the tangential components of $\vec{E}$ must be specified at the lower boundary. At present E_x and E_y are set to zero at the first grid point. This boundary is the earth's surface, and the boundary conditions for an infinite conductor are appropriate.

Unfortunately, an examination of Eqs. (22) and (31) indicate that the tangential component of $\vec{H}$ must also be specified. At present the following scheme is used. For H^2_{y1} the value H^1_{y1} is used for the initial pass through the grid. Then, a linear extrapolation based on H^2_{y2} and H^2_{y3} is used to give H^2_{y1}, and this value is used on the initial guess on the next pass through the grid. The same procedure is used for H_x.

3. AIR CHEMISTRY

Due to the lack of data a lumped parameteric air chemistry treatment is used. The appropriate rate equations to be solved are

$$\frac{dn_e}{dt} = Q - \beta n_e - \delta n_+ n_e + \tau n_e \tag{40}$$

$$\frac{dn_+}{dt} = Q - \delta n_+ n_e - \gamma n_+ n_- + \tau n_e \tag{41}$$

$$\frac{dn_-}{dt} = \beta n_e - \gamma n_+ n_e \tag{42}$$

with

Q	rate of ion/electron production
β	electron attachment rate to neutrals
δ	electron-positive ion recombination rate
τ	cascade rate
γ	positive ion-negative ion recombination rate

Initial charge neutrality and charge conservation gives

$$n_+ = n_e + n_- \quad , \tag{43}$$

so that only two of the above equations need to be solved. For reasons of stability as noted by Longley (Ref. 10) the rate equations for n_e and n_- will be solved.

$$\frac{dn_e}{dt} = Q + \tau n_e - \beta n_e - \delta(n_e + n_-)n_e \tag{44}$$

$$\frac{dn_-}{dt} = \beta n_e - \gamma(n_e + n_-)n_- \tag{45}$$

Note that Eqs. (44) and (45) are of the form

$$\frac{dF}{dt} + k(t)F = S(t) \tag{46}$$

which has the general solution

$$F(t) = F(o)e^{-\int_0^t k(t')dt'} + e^{-\int_0^t k(t')dt'} \int_0^t e^{\int_0^{t'} k(t'')dt''} S(t')\, dt' \tag{47}$$

An approximate solution (first order) of (47) is

$$F(t) \approx F(o)e^{-k(t/2)t} + \left(1 - e^{-k(t/2)t}\right) \frac{S(t/2)}{k(t/2)} \qquad (48)$$

The solution of (44) is

$$n_e^2 = n_e^1 e^{-k_1 \Delta\tau} - \left(1 - e^{-k_1 \Delta\tau}\right) \frac{S_1}{k_1} \qquad (49)$$

where

$$k_1 = \beta + \delta\left(n_e^1 + n_-^1\right)$$

$$S_1 = Q + \tau n_e^1$$

The solution of (45) is

$$n_-^2 = n_-^1 e^{-k_2 \Delta\tau} - \left(1 - e^{-k_2 \Delta\tau}\right) \frac{S_2}{k_2} \qquad (50)$$

where

$$k_2 = \gamma\left(n_e^1 + n_-^1\right)$$

$$S_2 = \beta n_e^1$$

The air conductivity is given by

$$\sigma = q\left(n_e\mu_e + n_-\mu_- + (n_e + n_-)\mu_+\right) \tag{51}$$

with

10

q electron charge

μ_e electron mobility

μ_- negative ion mobility

μ_+ positive ion mobility

If at a particular altitude the air density relative to sea level STP is ρ, then the values for the air chemistry parameters are given by

$$\delta = 4.5 \times 10^{-12} \text{ sec}^{-1}$$

$$\gamma = 2.3 \times 10^{-12} \text{ sec}^{-1}$$

$$\mu_e = \frac{\mu_e' \mu_w}{\left(\mu_e' + \mu_w\right)\rho} \quad \text{m}^2/(\text{volt-sec})$$

$$\mu_e' = 4.21 \times 10^{-2} * \sqrt{\frac{(E + 1.2 \times 10^6)}{(E + 8.81 \times 10^2)^2}} \quad m^2/(\text{volt-sec})$$

$$\mu_w = 9.0 \times 10^{-3}/H_2O \quad m^2/(\text{volt-sec})$$

E = total electric field magnitude

H_2O = fractional water vapor content

$$\mu_+ = 2.4 \times 10^{-4}/\rho \quad m^2/(\text{volt-sec})$$

$$\mu_- = 2.4 \times 10^{-4}/\rho \quad m^2/(\text{volt-sec})$$

The electron attachment rate to neutrals (β) is given by the following procedure. First calculate

$$BA = \frac{8.76 \times 10^7 - 1.057 \times 10^4 * E}{1.0 + 1.346 \times 10^{-4} * E}$$

if BA < 0 , set BA = 0

then calculate

$$\beta' = \frac{1.837 \times 10^{-8}}{1.0 \times 3.05 \times 10^{-5} * E} - 1.927 \times 10^7 + 54.4 * E - BA \qquad (52)$$

The attachment is given by

$$\beta = \beta' * \rho^2 \qquad \text{for} \qquad E < 2.0 \times 10^5$$

$$\beta = \beta' * \rho * \left[\frac{E - 2.0 \times 10^5}{8.0 \times 10^5} + \left(1.0 - \frac{E * 2.0 \times 10^5}{8.0 \times 10^5} \right) * \rho \right] \qquad \text{for}$$

$$2.0 \times 10^5 \leq E \leq 6.0 \times 10^6$$

$$\beta = \beta' * \rho \qquad \text{for} \qquad E \geq 6.0 \times 10^6 \qquad (53)$$

The cascading rate τ used in the code is a based-on data prescribed by Phelps (Ref. 11). A table based on this data is used with exponential interpolation between the data points. The fit for β and μ_e are the fits used in SCX, Dalich (Ref. 12).

4. SOURCES

The three components of current and conductivity from a typical HEMP run for a line of sight 30^{o} from the vertical in the south direction were fit in altitude and time. The geometry for the sources and comparison are shown in Fig. 41. The $\hat{y}$ vector is out of the page, $\hat{\varphi}$ into the page.

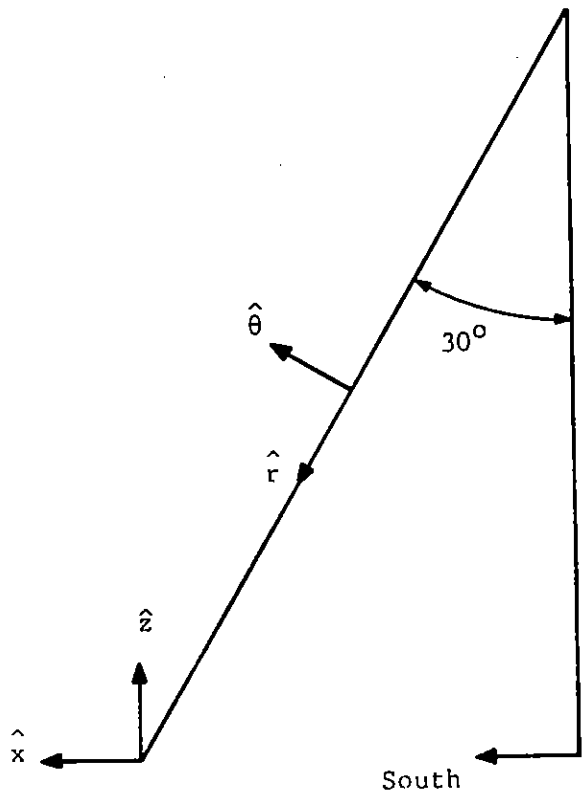

Figure 41. Comparison geometry.

The HEMP coordinates are

$$\hat{r} = \text{radial from the burst}$$

$$\hat{\varphi} = -\hat{r} \times \hat{B}_e$$

$$\theta = \hat{\varphi} \times \hat{r}$$

where $\hat{B}_e$ is a unit vector in the direction of the earth's magnetic field. The fits for all quantities are of the form

$$F(z,\tau) = Z(z)T(\tau)$$

where

$$Z(z) = \begin{cases} A_1 e^{\beta_1 (z - Z_0)} & Z < 3.0E + 4 \text{ meters} \\ A_2 e^{\beta_2 (z - Z_0)} & Z \geq 3.0E + 4 \text{ meters} \end{cases}$$

$$T(\tau) = Ce^{DT} / \left(1.0 + e^{(D+E)(\tau - \tau_0)}\right)$$

The constants for the three components of current and the conductivity are given in Table I.

TABLE I

SOURCE CURVE FIT CONSTANTS

	A_1	B_1	A_2	B_2	Z_0	C	D	E	τ_0
J_r	3.0701 (-4)	1.60 (-3)	-6.5788 (-5)	1.15196 (+2)	0	4.164 (-5)	5.0 (+8)	3.7 (+6)	2.026 (-8)
J_θ	3.0701 (-4)	1.60 (-3)	-6.5788 (-5)	1.15196 (+2)	3.0 (+3)	4.164 (-5)	5.0 (+8)	3.7 (+6)	2.026 (-8)
J_φ	3.0701 (-5)	1.60 (-3)	-6.5788 (-6)	1.15196 (+2)	0	4.164 (-5)	5.0 (+8)	3.7 (+6)	2.026 (-8)
σ	3.0701 (-4)	3.60015 (-7)	-6.5788 (-5)	2.5909 (-2)	0	1.0184	2.3 (+7)	7.4 (+5)	5.24 (-9)

No claim is made for the accuracy of these fits. The fits do, however, provide an easy-to-implement source package for use in debugging a high altitude code.

5. SAMPLE RESULTS

For the purpose of verifying the code the results from a one-dimensional high frequency approximation code are shown as the solid curve in Figs. 42-47. The results from the P code are denoted by ◇. As can be seen from the figures, agreement is quite good. A future document is planned in which late-time results from the P code will be presented.

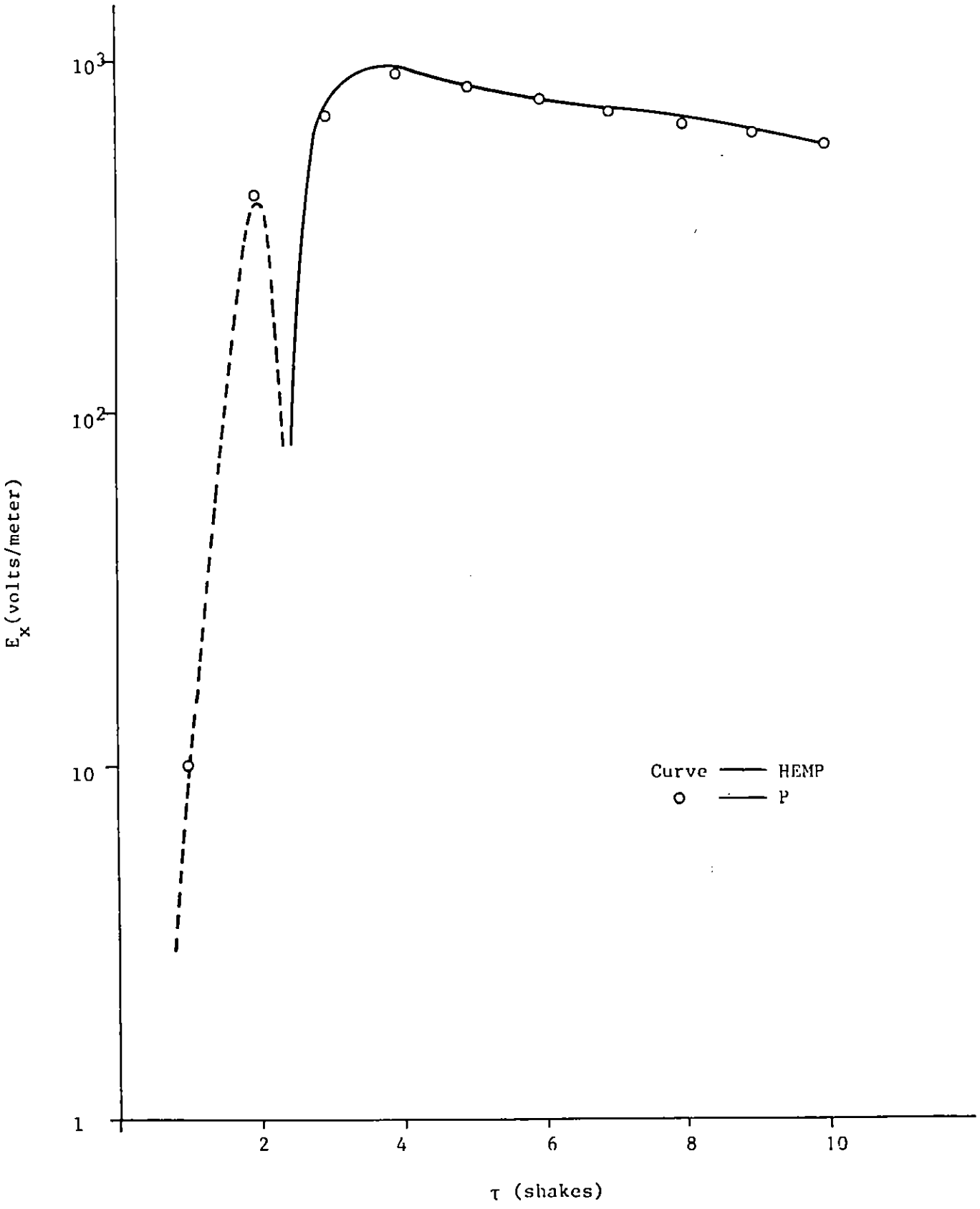

Figure 42. E_x at Altitude 50 km.

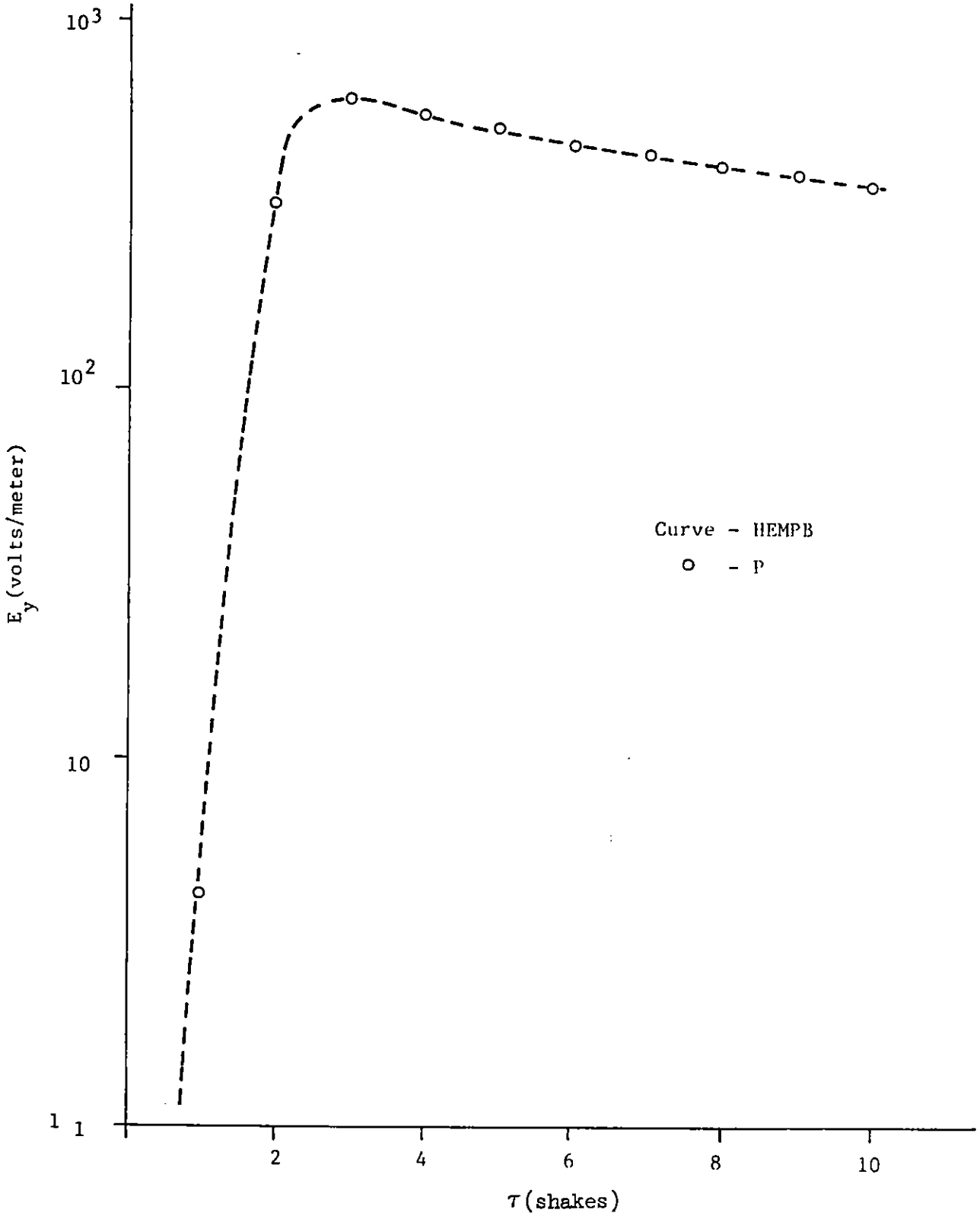

Figure 43. E_y at Altitude 50 km.

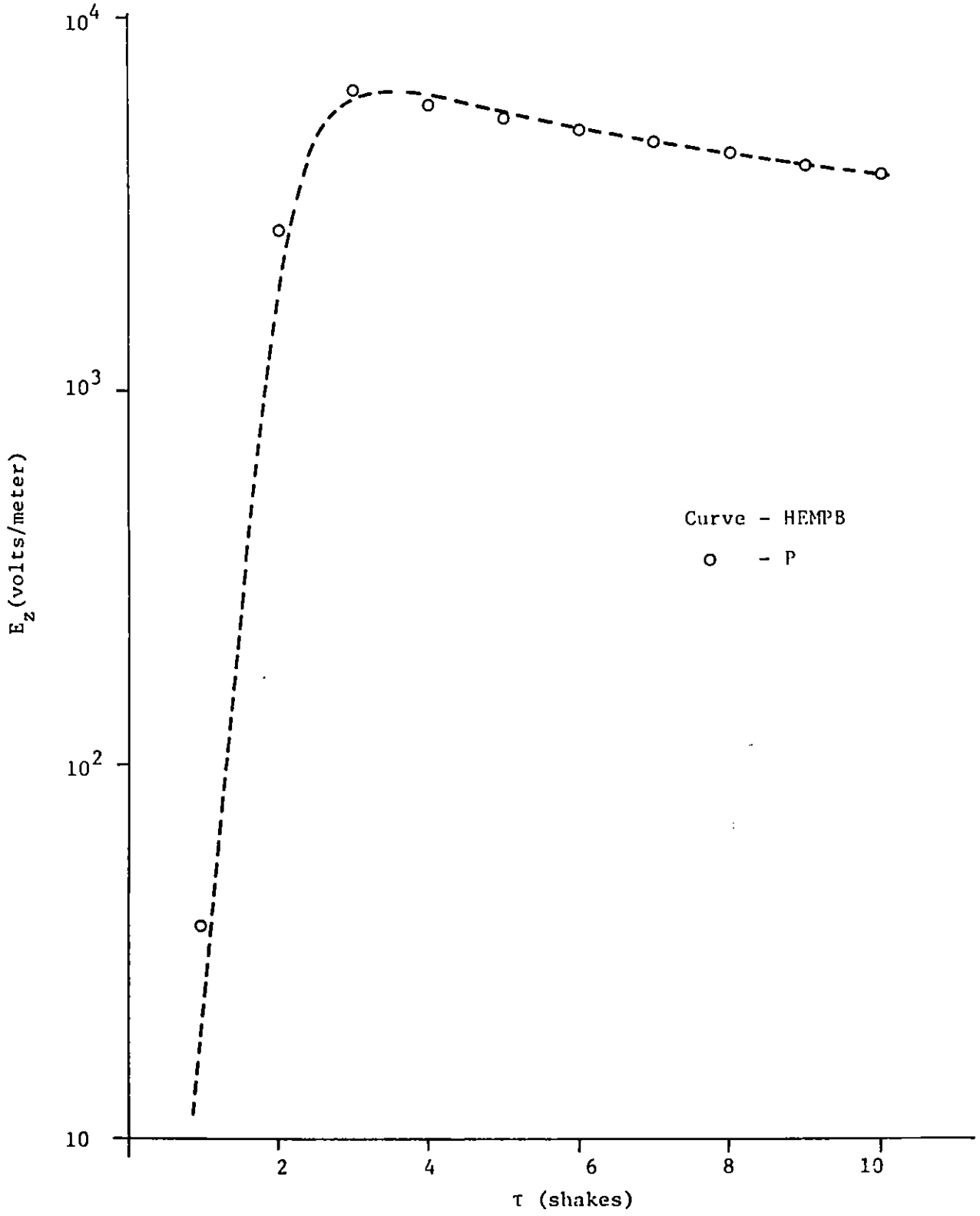

Figure 44. E_z at Altitude 50 km.

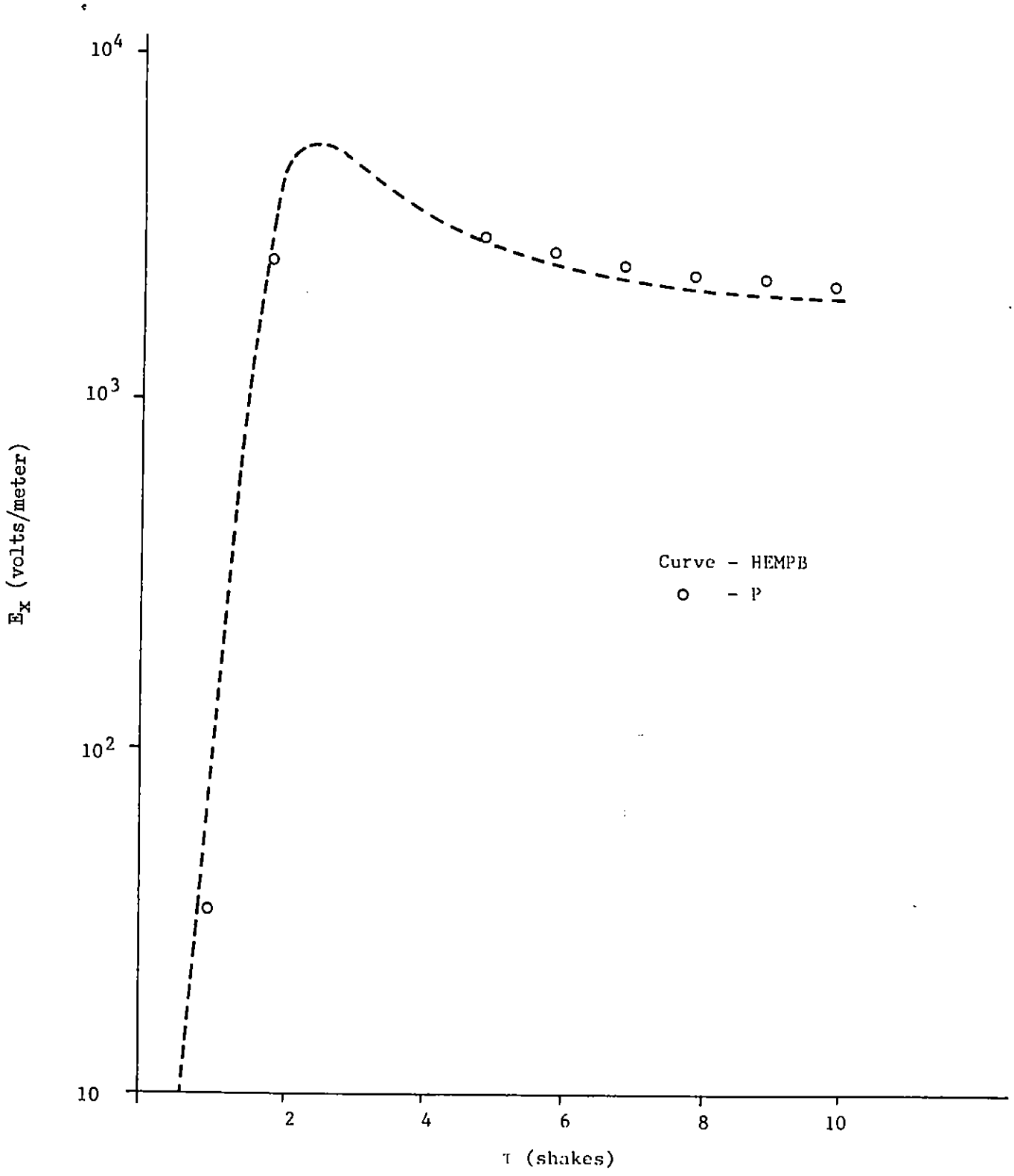

Figure 45. E_x at Altitude 30 km.

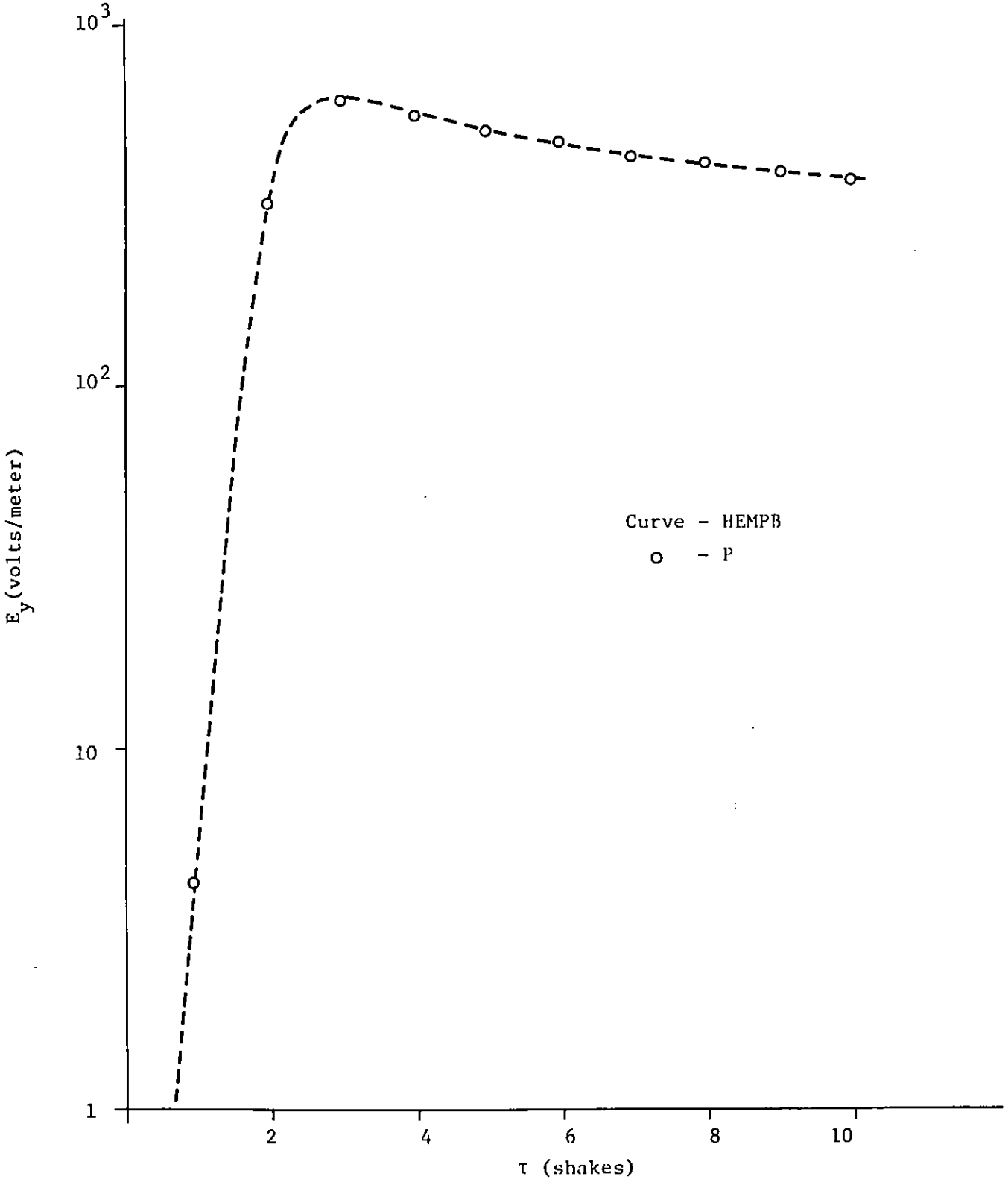

Figure 46. E_y at Altitude 30 km.

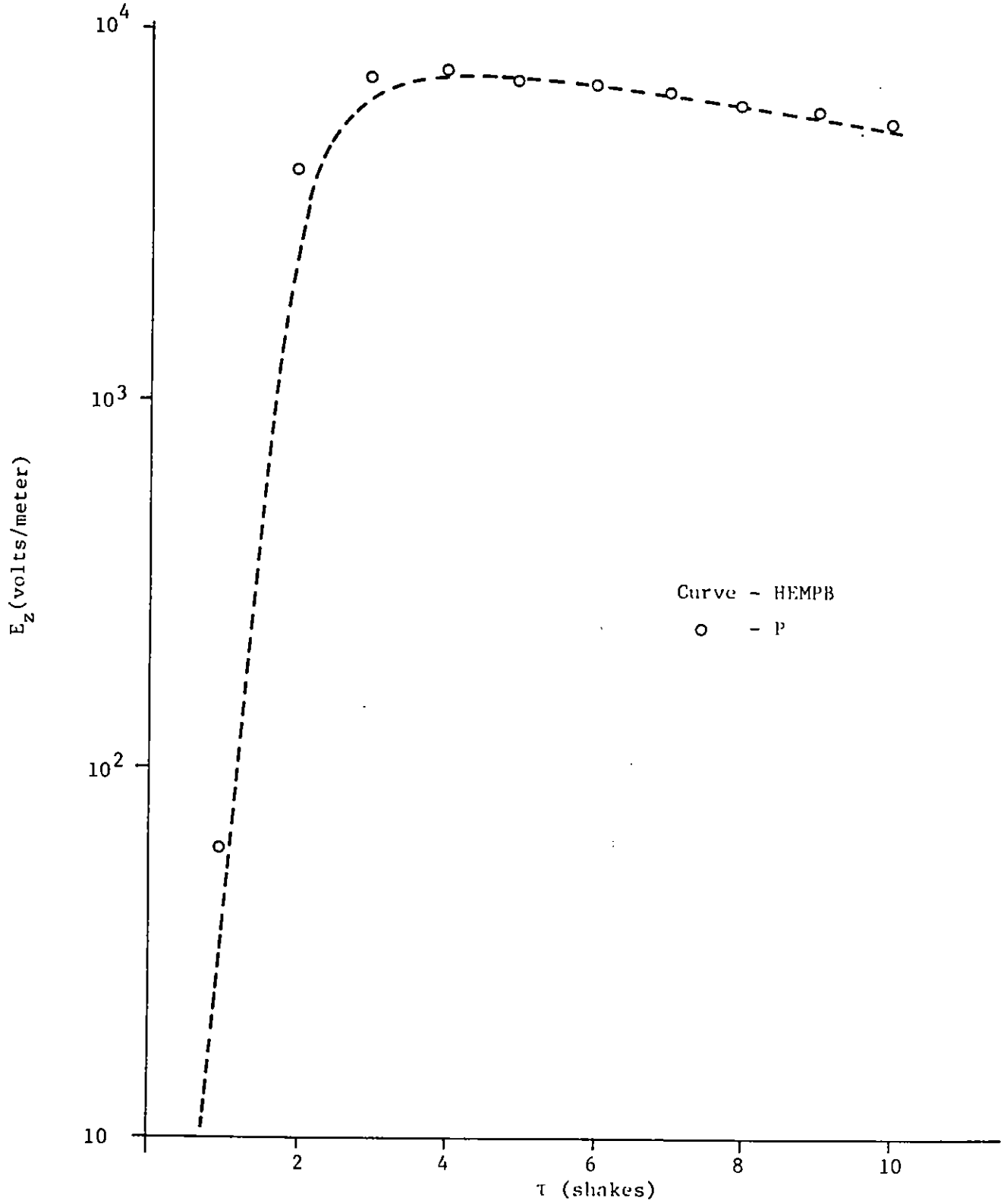

Figure 47. E_z at Altitude 30 km.

APPENDIX

CONVERSION FROM PRIMARY ELECTRON CURRENT TO TOTAL NUMBER OF SECONDARIES PRODUCED

The electron current in units of electrons/m^2sec is

$$J_e(t) = \frac{J(t)}{q} \tag{1}$$

where

$J(t)$ = current in units of amps/m^2

q = electron charge = -1.6021×10^{-19} coulombs

The total electron path length of all electrons within a cubic meter from time 0 to any time t is simply the integral of the total electron current.

$$\ell = \int_0^t J_e(t)\,dt = \frac{1}{q}\int_0^t J(t)\,dt \tag{2}$$

Now we can use a stopping power which is fairly good over the electron range to convert from electron path length to the total number of secondary electrons produced.

$$N(t) = \frac{\ell S}{c} = \frac{S}{qc}\int_0^t J(t)\,dt \tag{3}$$

where

S = stopping power in units of MeV/m

c = conversion from primary electron energy loss to number of secondary electrons produced

= 3.4×10^{-5} MeV/ion pair

Integral of the Current

$$J_r(t) = a_1 e^{b_1 t} + a_2 e^{b_2 t} \qquad \text{radial current}$$

$$J_\varphi(t) = a_3 e^{b_3 t} + a_4 e^{b_4 t} \qquad \text{phi current}$$

$$J_\theta(t) = a_5 e^{b_5 t} + a_6 e^{b_6 t} \qquad \text{theta current}$$

$$J(t) = \left[J_r^2 + J_\varphi^2 + J_\theta^2\right]^{1/2} \qquad \text{total current}$$

Assume for now that the integral of the total current is equal to the integral of the radial current.

$$\int_0^t J(t)\, dt \cong \int_0^t J_r(t)\, dt = \frac{a_1}{b_1}\left(e^{b_1 t} - 1\right) + \frac{a_2}{b_2}\left(e^{b_2 t} - 1\right) \qquad (4)$$

$$J_\theta(t) \cong .1\, J_\varphi(t)$$

$$J_\varphi(t) \cong .1\, J_r(t)$$

Average Stopping Power

The stopping power at any altitude is proportional to the air density

12

$$S(z) = S_0 \frac{\rho(z)}{\rho_0} \tag{5}$$

where

S_0 = stopping power at sea level

$\rho(z)$ = air density at the given altitude

ρ_0 = air density at sea level

The average energy of the Compton electrons produced by the source gamma rays is usually about 0.7 to 1.0 MeV. A check of stopping power tables for air indicates that a first guess of the average stopping power for electrons of this energy would be about 0.2 MeV/m.

Substitute Eqs. (4) and (5) into (3)

$$N(t) = \frac{S_0}{qc} \frac{\rho}{\rho_0} \left[\frac{a_1}{b_1} \left(e^{b_1 t} - 1 \right) + \frac{a_2}{b_2} \left(e^{b_2 t} - 1 \right) \right] \tag{6}$$

Substituting the values for S_0, q, and c

$$N(t) = -3.5 \times 10^{22} \frac{\rho}{\rho_0}\left[\frac{a_1}{b_1}\left(e^{b_1 t} - 1\right) + \frac{a_2}{b_2}\left(e^{b_2 t} - 1\right)\right] \tag{7}$$

Production Plus Attachment

Differential Equation:

$$\frac{dN}{d\tau} + \beta N = P \tag{8}$$

where

N = secondary electron density

τ = retarded time

β = attachment rate constant

P = production rate of secondary electrons

We will assume that β is only a function of air density and not a function of the electric field.

$$\beta = 10^8\left(\frac{\rho}{\rho_0}\right)^2 \text{ sec}^{-1} \tag{9}$$

The rate of production of secondary electrons is the derivative of Eq. (7)

$$P = -3.5 \times 10^{22} \frac{\rho}{\rho_0}\left[a_1 e^{b_1 \tau} + a_2 e^{b_2 \tau}\right] \tag{10}$$

Let

$$d_1 = -3.5 \times 10^{22} \frac{\rho}{\rho_0} a_1 \tag{11}$$

$$d_2 = -3.5 \times 10^{22} \frac{\rho}{\rho_0} a_2 \tag{12}$$

The differential equation is

$$\frac{dN}{d\tau} + \beta N = d_1 e^{b_1 \tau} + d_2 e^{b_2 \tau} \tag{13}$$

Taking the Laplace transform

$$sn - N(0) + \beta n = \frac{d_1}{s - b_1} + \frac{d_2}{s - b_2} \tag{14}$$

Assuming $N(0) = 0$,

$$n = \frac{1}{s + \beta}\left[\frac{d_1}{s - b_1} + \frac{d_2}{s - b_2}\right] \tag{15}$$

Using the convolution property of Laplace transforms

$$\mathcal{L}^{-1}\left\{f(s)\, g(s)\right\} = \int_0^{\tau} F(u)\, G(\tau - u)\, du \tag{16}$$

$$\mathcal{L}^{-1}\left\{\frac{d_1}{s - b_1} + \frac{d_2}{s - b_2}\right\} = d_1 e^{b_1 \tau} + d_2 e^{b_2 \tau} \tag{17}$$

$$\mathcal{L}^{-1}\left\{\frac{1}{s + \beta}\right\} = e^{-\beta \tau} \tag{18}$$

$$N = \int_0^{\tau} \left[d_1 e^{b_1 u} + d_2 e^{b_2 u}\right] e^{-\beta(\tau - u)}\, du$$

$$= e^{-\beta \tau} \int_0^{\tau} \left[d_1 e^{(b_1 + \beta)u} + d_2 e^{(b_2 + \beta)u}\right] du \tag{19}$$

$$N = e^{-\beta\tau}\left\{\frac{d_1}{b_1 + \beta}\left(e^{(b_1+\beta)\tau} - 1\right) + \frac{d_2}{b_2 + \beta}\left(e^{(b_2+\beta)\tau} - 1\right)\right\}$$

$$= \frac{d_1}{b_1 + \beta}\left(e^{b_1\tau} - e^{-\beta\tau}\right) + \frac{d_2}{b_2 + \beta}\left(e^{b_2\tau} - e^{-\beta\tau}\right) \qquad (20)$$

If the production rate of secondary electrons is zero after some time τ_x, then the density for $\tau > \tau_x$ is simply

$$N(\tau > \tau_x) = N(\tau_x)\, e^{-\beta(\tau-\tau_x)} \qquad (21)$$

REFERENCES

1. Marks, J. A., HAPS, A Two-Dimensional Computer Code to Calculate Electromagnetic Fields Resultant from High Altitude Nuclear Detonations, The Dikewood Corporation, Albuquerque, New Mexico, March 1972.

2. Longmire, C. L., Development of the LHAP EMP Code, Mission Research Corporation, Santa Barbara, California, December 1972.

3. Knight, R. L., "Numerical Solutions of Maxwell's Equations with Azimuthal Symmetry in Prolate Spheroidal Coordinates," The Dikewood Corporation, 1969, Electromagnetic Pulse Theoretical Notes, 2, Note 62, April 1971.

4. Beckwith, L. K., HEMP II, A Computer Program to Calculate EMP from High Altitude Nuclear Detonations, The Dikewood Corporation, December 1969 (SRD).

5. Ekkila, J. H., "Calculations of the EMP from High Altitude Nuclear Detonations," AFWL, 1967, Electromagnetic Pulse Theoretical Notes, 2, Note 26, April 1971.

6. Knight, R. L., et al., "HEMP B" (to be published as AFWL-TR).

7. Schlegel, G. K., et al., Electromagnetic Pulse Environment Handbook (U), Air Force Weapons Laboratory, Kirtland Air Force Base, New Mexico, January 1972 (SRD/CNWDI).

8. Marks, J. A., RORDER, A Code to Reorder Time by Range Data into Range by Time Data, Undocumented, 1973.

9. Parkinson, E. R., et al., Late Time EMP from Exoatmospheric Bursts (U), pp. 24-32, Science Applications, Inc., La Jolla, California, May 1973 (SRD).

10. Longley, H. J., "Development and Testing of LEMP1," EMP-TN-75.

11. Phelps, A. V., and W. H. Korman, "Studies and Experimental Work on Atomic Collision Processes Occurring in Atmospheric Gases," AFWL-TR-66-34.

12. Dalich, S. J., "SCX: A Two-Dimensional Ground Burst EMP Code," SAI-73-501-ABQ.